University of L'Aquila

Department of Physical and Chemical Sciences

PhD in Physical and Chemical Sciences

XXXVI cycle

Biocatalysis: A Multifaceted Examination of Free and Immobilized Enzymes

SSD CHIM/06

PhD Candidate

Alice Vetrano

PhD Course coordinator

Prof. Massimiliano Aschi

Supervisor

Prof. Nicoletta Spreti

Abstract

In the current landscape of chemical processes, a predominant focus gravitates toward the integration of green chemistry principles, emphasizing the imperative of maximizing reaction yields while minimizing by-products in adherence to the concept of atom economy. This paradigm shift has underscored the significance of employing biocatalysts, particularly enzymes renowned for their remarkable selectivity and specificity, as pivotal components of sustainable solutions. In essence, enzymes stand as indispensable allies in the pursuit of sustainable chemical processes, offering a multifaceted solution that aligns with the ethos of green chemistry. Their unique catalytic properties and biocompatibility render them not just catalysts but catalysts with an environmentally conscious edge, promising advancements that resonate across various industrial landscapes while fostering a more sustainable and eco-friendly approach from the production of pharmaceutically active compounds to energy production, from fine chemistry to polymer science, and so forth.

In this thesis work, we focused specifically on two classes of enzymes: lipases and dehydrogenases. Lipases exhibit remarkable chemoselectivity, regioselectivity, and stereoselectivity during catalysis. These enzymes, abundant and accessible, can be efficiently produced in significant quantities by microbial organisms, notably fungi and bacteria. Moreover, lipases typically function independently of cofactors and minimize catalyzing side reactions. These combined attributes establish lipases as the primary and widely adopted group of biocatalysts within the realm of organic chemistry. In particular, the first study concerns the immobilization of *Candida rugosa* lipase in alginate beads, while the second study focuses on investigating the effect of organic solvents on *Candida antarctica* lipase

B. Firstly lipase from *Candida rugosa* (CRL) has been immobilized in different formulations of calcium alginate beads, prepared by ionotropic gelation, which differ from each other in $CaCl_2$ concentration and hardening time, to investigate the effects of immobilization conditions on enzyme properties. Morphological studies on all hydrated beads, performed by SEM equipped with a Peltier plate, revealed a different internal compactness. Despite this, all types of beads had an immobilization yield of 100% measured with the Bradford method and about 94% evaluated from the residual activity of the preparation solutions; moreover, all entrapped biocatalysts catalyzed the complete hydrolysis of *p*-nitrophenyl acetate, even after one month of storage in distilled water at 4 °C. When the internal microstructure of the beads was more compact, the rate of hydrolysis of the most hydrophobic *p*-nitrophenyl dodecanoate was halved, probably due to mass transfer limiting effects. The immobilized lipase had better resistance to temperature inactivation than the free form: enzyme residual activity at 50 °C after a week were approximately 70% and 20% for the immobilized and free forms respectively. An excellent recyclability in water at 25 °C of entrapped enzyme was also found, having residual activity greater than 80% at the tenth reaction cycle. The best bead formulation was then used for the resolution of (R)-1-phenylethanol in aqueous solution starting from racemic (R,S)-1-phenylethyl acetate.

The second project focuses on the effect that the addition of percentages of organic solvent to aqueous solutions has on the enzymatic activity of *Candida antarctica* lipase B (CalB). The addition of organic solvents to an aqueous medium for enzymatic reactions it is often necessary and can offers several advantages, as they can increase the solubility of substrates but can also lead to enzyme inactivation and/or aggregation. The effect of

adding 30% of several water-soluble organic solvents on the catalytic activity of lipase B from *Candida antarctica* (CalB) was studied, and the results showed that the highest activity was obtained with the addition of *t*-butanol. *t*-Butanol and acetonitrile were selected and the kinetic parameters, determined to deepen their effect on CalB activity, showed that the addition of acetonitrile improved the enzyme–substrate affinity, while water–*t*-butanol mixtures led to a more than ninefold increase in k_{cat}. To rationalize at a molecular level the kinetic results, molecular dynamic simulations were performed. Analysis of the accessibility of the active-site cavity, solvent occupancy in the site and in the oxyanion hole, and the stability of the catalytic triad in the two solvent mixtures, provided insight into their effects on the catalytic properties of CalB. The lower occupancy in the oxyanion hole of water molecules and a shorter residence time in the active site of acetonitrile molecules in the acetonitrile–water mixture contributes to the higher enzyme–substrate affinity found experimentally. Conversely, the higher k_{cat} in the *t*-butanol mixture is explained by the higher stability of the catalytic triad and by an increase in the nucleophilicity of the catalytic serine due to the persistent presence of *t*-butanol molecules in the active site.

The second group of enzymes under study comprises alcohol dehydrogenases, specifically focusing on horse liver alcohol dehydrogenase (HLADH). Alcohol dehydrogenases (ADHs) have garnered considerable interest owing to their crucial involvement in alcohol metabolism, detoxification of xenobiotics, and broader implications within enzymology and biochemistry research. HLADH, an extensively researched enzyme extracted from equine liver tissue, plays a pivotal role in various enzymatic processes, thus warranting detailed investigation. The first part of the study

delves into the kinetic intricacies and structural dynamics of Horse Liver Alcohol Dehydrogenase (HLADH) through a comprehensive investigation employing steady-state kinetics and molecular dynamics simulations. The research elucidates the enzyme's behavior concerning various substrates, unveiling distinct kinetic profiles and cofactor dependencies. Kinetic analyses revealed anomalous behaviors in enzyme-substrate interactions, notably deviating from classical Michaelis-Menten kinetics at varying NADH concentrations. This exploration led to the identification of a potential allosteric site, shedding light on how high cofactor concentrations influence protein dynamics and catalytic properties. Molecular dynamics simulations provided structural insights into the impact of inhibitory NADH concentrations, unveiling altered protein flexibility and cavity sizes. In the second part of the work HLADH has been immobilized on calcium-alginate beads and used for both oxidation and reduction reactions. To avoid swelling of the beads and their subsequent breakage, calcium ions were added to both reaction and storage solutions, allowing the beads to maintain the initial structural features. The techniques used for this purpose revealed that 2 mM Ca^{2+} is the optimal concentration, which does not significantly change the weight of the beads, the amount of water in them, and their external and internal structure. The optimized experimental procedure has been used to verify the properties of the enzyme in terms of reusability, storage, and thermal stability. The addition of calcium ions allows the enzyme to retain more than 80 % of its initial activity for fourteen cycles and approximately 50 % at the twentieth cycle. Moreover, when the biocatalyst was stored in a buffer solution containing 2 mM Ca^{2+}, the retention of enzyme activity after 30 days was 100 %, compared to that measured before incubation. The encapsulated enzyme exhibits greater

thermal stability than free HLADH up to at least 60 °C, preventing dimer dissociation into the two subunits.

Table of Contents

Chapter 3: Experimental and Computational Techniques

Chapter 4: What makes lipases so attractive?

Chapter 5: Horse liver alcohol dehydrogenase

Addendum

Chapter 1

Introduction

1.1 Green Chemistry and Biocatalysis: A Sustainable Symbiosis

In 1987, the World Commission on Environment and Development introduced the idea of sustainable development through the publication of "Our Common Future". This report recognized the significance of promoting both industrial and societal progress to address the growing global population's needs. It underscored the critical necessity for this advancement to maintain long-term environmental and social sustainability[1]. During the mid-1980s, a heightened awareness emerged regarding the substantial waste produced by the chemical industry. It became evident that a fundamental shift in perspective was needed, away from conventional notions that emphasize chemical yield through reaction efficiency and selectivity. Instead, a new approach was needed that would prioritize the optimization of raw material utilization, the reduction of waste production and the avoidance of toxic or hazardous substances[2]. Initially, this concept was denoted as "clean chemistry". However, the widespread term "green chemistry" came into use in the mid-1990s, introduced by Anastas and fellow researchers from the US Environmental Protection Agency (EPA). The fundamental principle guiding this approach is "benign by design", as articulated in Anastas and Warner's 12 principles of green chemistry[3] reported in Figure 1.

Figure 1: Principles of green chemistry.

Green chemistry focuses on preventing waste at source, embodying the fundamental principle that avoiding environmental damage is more effective than trying to remedy it after the fact. Since the mid-1990s, the concept of green chemistry has gained widespread acceptance in both industrial and academic circles. A significant contributor to waste generation, especially in the production of fine chemicals and pharmaceuticals, stems from the employment of stoichiometric reagents, predominantly inorganic, in organic synthesis[4]. For instance, the use of metals like sodium, magnesium, zinc, iron, metal hydride reagents such as lithium aluminum hydride and sodium borohydride, as well as oxidizing agents like permanganate, manganese dioxide, and chromium (VI) compounds, all contribute to this waste[5]. Furthermore, mineral acids like sulfuric acid, hydrofluoric acid, phosphoric acid, and Lewis's acids like aluminum chloride, zinc chloride, and boron trifluoride, whether used directly in reactions or during subsequent processing, also play a substantial role in waste generation[6]. Additionally, the intricate molecular structures of most pharmaceuticals require multi-step

syntheses, which tend to produce more waste than simpler chemicals. The solution to these environmental challenges is clear: replace these inefficient stoichiometric methodologies with more efficient catalytic alternatives that are atom-efficient and involve fewer reaction steps[7]. In essence, the key to achieving green and sustainable chemistry lies in the adoption of various catalytic methods in organic synthesis, including heterogeneous catalysis, homogeneous catalysis, organocatalysis, and biocatalysis[8].

1.1.1 Biocatalysis

Biocatalysis has many interesting features in the context of green chemistry and sustainable development. First, enzyme catalysts come from renewable materials and possess characteristics such as biocompatibility and, in some cases, edibility. They are also biodegradable and virtually risk-free, making them an exceptionally sustainable choice and perfectly in line with sustainability criteria[2]. Biocatalysis circumvents the use of scarce and precious metals like palladium, platinum, and rhodium, eliminating the risk of contaminating products with these valuable elements. The long-term commercial viability of many of these "endangered" metals remains uncertain. Furthermore, the cost associated with removing even trace amounts of noble metals from end products can be substantial[9]. Biocatalytic reactions take place in environmentally friendly solvents, primarily water, and operate under mild conditions, including physiological pH, ambient temperature, and pressure. These reactions exhibit exceptional activity and display high levels of chemoselectivity, regioselectivity, and stereoselectivity[10]. Often, they do not require the typical activation, protection, and deprotection steps of functional groups seen in traditional organic syntheses. Consequently, biocatalysis leads to more efficient

processes that are economically and environmentally attractive due to reduced energy consumption, minimized usage of raw materials, reduced waste generation, and improved step economy[11]. Thanks to their higher selectivity and gentler reaction conditions, biocatalytic processes frequently yield products of greater purity compared to traditional chemical or chemo-catalytic processes. Enzymatic reactions, excluding fermentations, can be conducted in standard multipurpose batch reactors without the need for additional investment in specialized equipment, such as high-pressure apparatus[12]. Furthermore, biocatalytic reactions generally occur under similar temperature and pressure conditions, facilitating the integration of multiple reactions into environmentally efficient cascade catalytic processes[13]. As shown in Table 1[2], biocatalysis conforms with 10 of the 12 principles of green chemistry and is not relevant for the other two (principles 4 and 10), which concern the design of safer, biodegradable products.

Table 1: Green Chemistry and Biocatalysis.

	green chemistry principle	biocatalysis
1	waste prevention	significantly reduced waste
2	atom economy	more atom- and step-economical
3	less hazardous syntheses	generally low toxicity
4	design for safer products	not relevant
5	safer solvents and auxiliaries	usually performed in water
6	energy efficiency	mild conditions/energy-efficient
7	renewable feedstocks	enzymes are renewable
8	reduced derivatization	avoids protection/deprotection steps
9	catalysis	enzymes are catalysts
10	design for degradation	not relevant
11	real-time analysis	applicability to biocatalytic processes
12	inherently safer processes	mild and safe conditions

However, the widespread adoption of biocatalysis has faced significant limitations due to the scarcity of commercially available enzymes, which were primarily hydrolases like lipases and proteases used in applications such as food and beverage processing and laundry detergents[14]. Thanks to significant advancements in biotechnology over the past two decades, this landscape has undergone a remarkable transformation. Just thirty years ago, it was necessary to adapt processes to accommodate the available enzymes[15]. Recognizing the need for a new approach, directed (in vitro) evolution techniques were employed to engineer enzymes with precise process-related parameters, such as activity, specificity, and stability[16]. Today, it is entirely feasible to fine-tune enzymes to suit specific optimal processes, thereby embracing the concept of designing genuinely benign processes[17]. Moreover, their storage and operational stability can be improved through efficient immobilization, allowing for cost-effective recovery and multiple recycling in the form of free-flowing solids[18]. As a result of these advancements, biocatalysis has evolved into a highly appealing industrial technology[19–21] and has perfectly integrated into mainstream organic synthesis, particularly for the enantioselective synthesis of active pharmaceutical intermediates (APIs)[22].

1.1.2 Enzyme Immobilization

As previously mentioned, the demand for sustainable processes has significantly increased the use of enzymes as catalysts in various industrial sectors[23]. This rise in demand is accompanied by advancements in protein extraction and purification technology, as well as innovations in protein engineering. Over the past two decades, the utilization of enzymes has steadily expanded across a wide range of industrial sectors. These sectors

encompass the dairy production, the transformation of starch[24], baking[25], and beverage production[26] (such as wine, beer, and fruit concentrates). Enzymes also play a crucial role in the textile industry, being employed in various manufacturing processes and purification procedures[27]. Furthermore, enzymes have become an integral part of industries such as papermaking[28], cosmetics[29], healthcare[30], chemical and detergent production[31]. In addition to their established applications, enzymes are finding new roles in emerging industrial sectors, such as biosensor manufacturing, due to their remarkable specificity for target biomarkers. Enzymes are also increasingly utilized in biofuel production and in the treatment and recycling of wastewater[32]. However, enzymes face challenges related to their short shelf life, limited stability, and sensitivity to various process conditions. Many of these drawbacks can be mitigated or eliminated through immobilization techniques. The immobilization of enzymes has been a fascinating area of study since the 1960s[33]. This concept was first introduced by Nelson and Griffin in 1916 when they observed that invertase could hydrolyze sucrose after being absorbed onto charcoal[34]. Since then, numerous reversible and irreversible methods of enzyme immobilization have been developed, enhancing the physicochemical properties of enzymes, and making them suitable for practical applications[35]. Various immobilization methods including encapsulation, cross-linking, covalent binding, adsorption, and entrapment have been applied so far, as displayed in Figure 2[36].

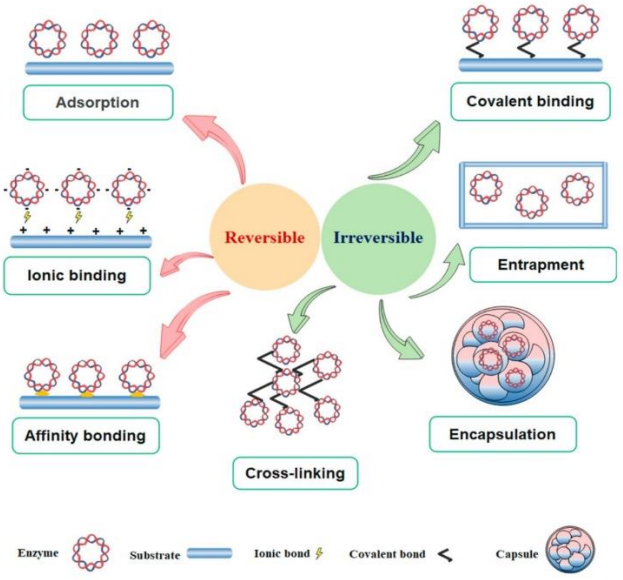

Figure 2: Diagram illustrating major enzyme immobilization methods.

Covalent binding

Covalent binding is a widely recognized method for immobilizing enzymes, achieved by linking enzymes to support materials (e.g., porous silica, polyacrylamide, agarose, porous glass, etc.) through a highly stable linkage. This approach offers several advantages, including the creation of robust enzymes and the ability to recover and reuse them effectively[37]. The covalent binding process primarily involves the activation of the support material by introducing reactive molecules and modifying the polymer's structure to activate the entire matrix[38]. Hydrophilic polysaccharide polymers are commonly used as supports in this technique. Electrophilic groups are also employed and generated on the support material at the start of the reaction, forming strong interactions with the nucleophiles in proteins[39]. Unfortunately, covalent binding has some limitations. It requires relatively complex procedures and prolonged incubation periods to achieve proper

immobilization. In some cases, further modifications to the enzyme's structure are required to expose functional groups suitable for covalent binding, and these alterations in the reaction environment may lead to enzyme denaturation[40]. Moreover, the quantity of immobilized enzymes bound to carriers is typically low, making them less suitable for large-scale industrial applications. Additionally, limitations in the mobility of enzymes attached to carriers may restrict the necessary conformational changes during catalysis, resulting in decreased enzyme activity[41].

Cross-linking

Cross-linking immobilization is a method in which enzymes are linked together through covalent bonds, and this occurs without the need for carriers[42]. This intermolecular cross-linking is achieved by employing linker agents that act as bridges connecting two neighboring enzyme molecules. Cross-linking immobilization establishes a strong bond between the enzymes, resulting in enhanced stability. Various approaches to cross-linking have been documented, including cross-linked spray-dried enzymes, cross-linked aggregates, and cross-linked dissolved enzymes, among others[43].

Adsorption

Adsorption is a straightforward method of immobilizing enzyme onto a carrier, where reversible immobilization is achieved. This technique primarily relies on physical adsorption. Various materials, including ion-exchange resins, alumina, activated carbon, and others, can be used to facilitate adsorption[44]. Although this method is cost-effective and easy to execute, it is characterized by relatively weak binding forces, such as hydrogen bonds, salt linkages, ionic bonds, and hydrophobic interactions, between the carrier and the enzyme. The advantages of enzyme immobilization by adsorption are its

minimal requirement for activation steps, the need for only a few reagents, cost-effectiveness and simplicity of implementation [45].

Ionic Binding

Ionic binding is a simple, cheap, and reversible method for immobilizing enzymes, which involves ionic interactions between enzymes and support materials. This noncovalent immobilization process can be easily reversed by adjusting temperature or ionic strength. Typically, the support materials used in this technique carry charges, and the enzymes must have opposite charges for binding to occur. The reversibility of ionic bonding can be achieved by altering the pH or by salting out the enzymes. However, the presence of charged support materials presents potential challenges, including possible distortion of the enzyme's structure and alterations in enzyme kinetics. Additionally, excessive charges can negatively impact enzyme catalysis, potentially reducing the overall product yield [46].

Affinity binding

Affinity binding is a process in which enzymes are immobilized onto a support matrix through precise and specific interactions. This immobilization method takes advantage of the enzyme's inherent specificity to effectively bind to the support under different physiological conditions. This can be accomplished through two main approaches. The first method involves pre-attachment of an affinity ligand for the target enzyme to the support matrix. In the second method, the enzyme is either modified or combined with another molecule, which imparts an affinity for the matrix, enabling efficient binding[47].

Entrapment

The entrapment method is based on caging the enzyme within a polymeric network by covalent or noncovalent bonds. By controlling the pore size of the polymeric network, which allows free diffusion of reaction components like substrates and products, enzyme leakage can be effectively prevented[48]. Entrapment offers various advantages, such as high enzyme loading capacity, cost-effectiveness in production, improved mechanical stability of the entrapped enzymes, and enhanced control over mass transfer[49]. One of the most employed methods for enzyme entrapment involves the gelation of polycationic or polyanionic polymers after the addition of multivalent counterions[50,51]. It provides the large surface area between the polymeric material and the enzyme. The drawback is the inactivation of the enzyme during entrapment.

Encapsulation

The encapsulation technique entails the trapping of various biomolecules within polymeric matrices. Encapsulation is a subset of entrapment, as both enzymes and cells exist freely in solutions, albeit within a regulated environment [52]. This method involves enclosing enzymes within a protective shell or membrane. The encapsulation process creates a defined barrier or coating around the enzyme, often forming a microcapsule or a vesicle. This protective shell can be permeable, allowing the substrate and product molecules to interact with the encapsulated enzyme while shielding it from external factors. Encapsulation generally provides a more controlled and selective environment for the enzyme. Large enzymes are confined within the capsules, preventing their movement in or out, while small substrates and products can pass through a semi-permeable membrane without hindrance.

However, some limitations are associated with this technique. For instance, the diffusion issue is severe and may cause rupturing of the membranes if the reaction products accumulate quickly[53].

1.1.3 Alginate Composites

As previously discussed, entrapment is a method for physically immobilizing substances, often achieved through a gelation process. Alginate stands out as one of the most commonly employed polymers for this purpose due to its biocompatibility, biodegradability, and its capacity to easily form desired three-dimensional structures in an aqueous medium (hydrogel) by binding divalent cations. Alginate is a linear copolymer comprised of β-D-mannuronate and α-L-guluronate monomeric units connected by 1-4 glycosidic bonds. This polymer is structured into oligopolymer blocks containing either mannuronate units (M), guluronate units (G), or alternating combinations of both monomers (MG)[54]. The crosslinking occurs through ionic interactions that specifically take place between the guluronate blocks and the crosslinking agents (generally Ca^{2+}), forming a structure commonly referred to as the "egg-box" (Figure 3)[55].

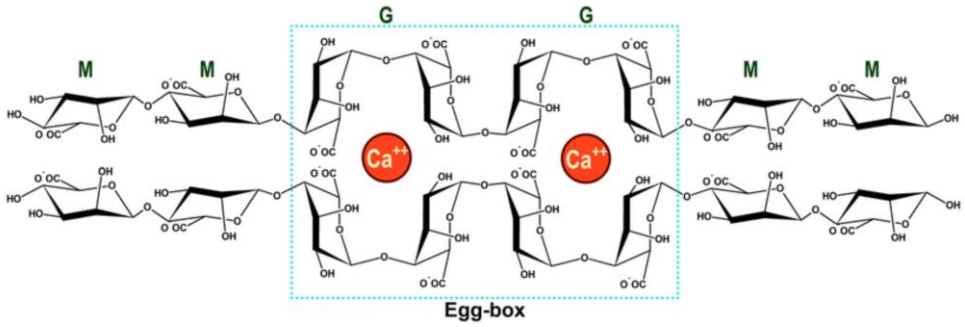

Figure 3: Structure known as "egg-box" for its particular spatial geometry, due to inter-chain interactions of the G blocks when they chelate the metal cation.

Alginate and its gels have a wide range of diverse applications. Historically, alginate has been predominantly used in the food industry, serving as an effective emulsifier, stabilizer, and gelling agent for food products. This versatile polymer has also found numerous applications in the pharmaceutical field[56]. For instance, it is utilized as an excipient in medications, especially for the treatment of heartburn and acid reflux (e.g., Gaviscon®, Bisodol®, Asilone™). Additionally, it is employed as a material for dental impressions and wound dressing (Algicell®, AlgiSite M™, Comfeel Plus®, Kaltostat®, Sorbsan®, and Tegagen™)[57]. These different applications are made possible by the advantageous characteristics of alginate, such as biocompatibility and non-immunogenicity, which are closely tied to the polymer's hydrophilicity[58]. Over the past decade, alginate has been extensively studied as an encapsulation material, with the number of publications on the topic still increasing, as can be seen in the Figure 4[59].

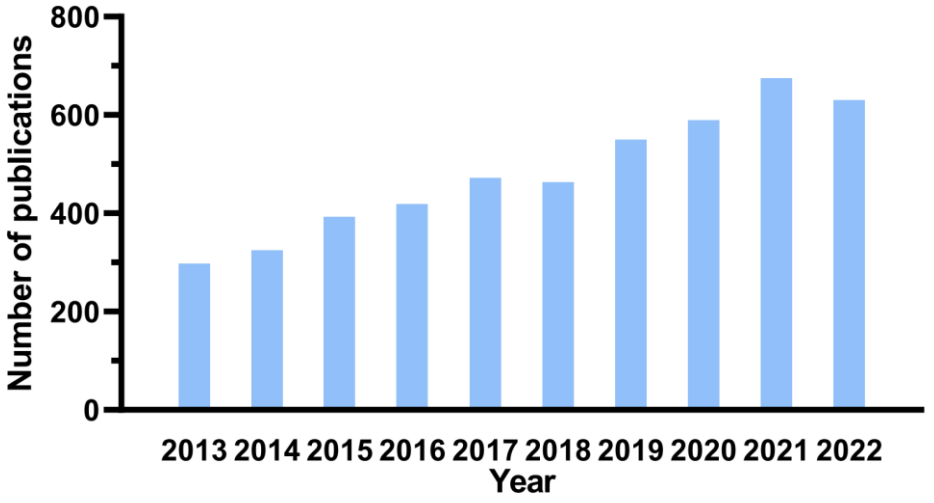

Figure 4: Number of publications of encapsulation studies using alginate in the last decade, obtained from Web of Science database.

The utilization of alginate-based materials for encapsulation holds significant potential in enhancing the stability of bioactive components, including enzymes and pharmaceuticals. By encapsulating bioactive substances within these hydrogels, it is possible to protect them from degradation, enhance their overall stability, and potentially direct their delivery to specific locations within the body. Alginate composites exhibit diverse morphologies, encompassing spheres (gel beads and emulsions), films, and fibers, as depicted in Figure 5 [60].

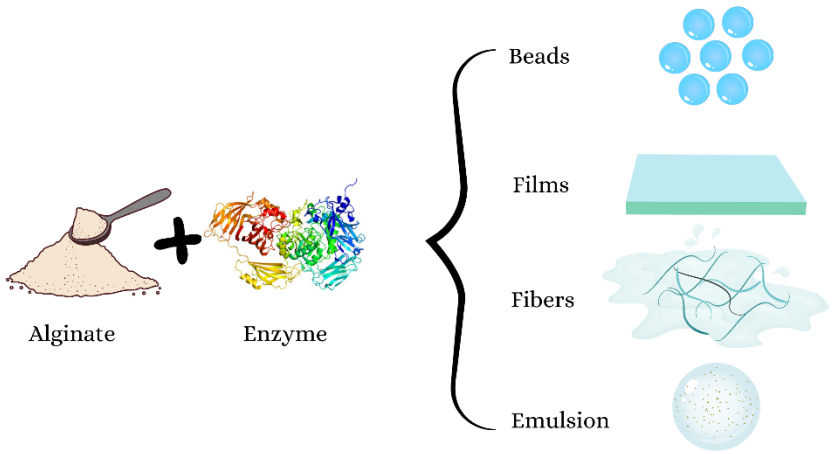

Figure 5: Alginate-based encapsulation systems.

The primary contrast among these variations of alginate composites resides in their level of gelation, a characteristic determined by the concentration of distinct precursors (e.g., sodium alginate and calcium ions) employed in the synthesis[61]. Alginate beads, distinguished by their outstanding stability and simple manufacturing, find extensive use in enzyme encapsulation. On the other hand, alginate films find primary utility in the field of food packaging and preservation. In this context, they demonstrate their value by serving as effective carriers of antibacterial enzymes, such as lysozyme, thereby

enhancing their enzymatic activity [62]. Although alginate fibers have also been employed for enzyme encapsulation, contemporary research focuses primarily on their application in the development of biomedical materials for tissue engineering and wound dressing.

Alginate Beads

Gel beads, among the various forms of alginate composites, occupy the predominant position as the preferred choice for encapsulation and enzyme delivery. This preference is attributed to the simplicity of the preparation procedures and the gentle conditions they require. Typically, the formation of gel beads through ionic gelation involves the process of dripping alginate droplets into solutions containing divalent ions, and this method ranks among the most widely employed techniques for encapsulating enzymes and other bioactive substances (Figure 6)[63].

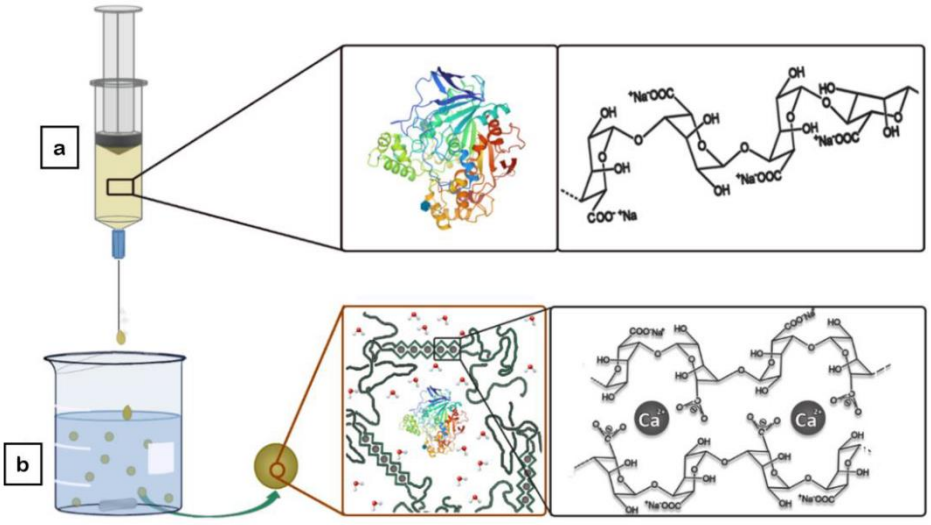

Figure 6: Preparation of alginate beads by ionotropic gelation.

One of the distinctive features of alginate gel beads is the possibility to control various properties, including microsphere size, porosity and release

profiles. These attributes can be fine-tuned by manipulating factors such as pH and alginate concentrations, allowing for a tailored approach in designing and optimizing the encapsulation and release characteristics of gel beads[64].

References

1 Y. K. Choy, *Sustainable Development*, 2015, **2**, 1197–1211.

2 R. A. Sheldon and J. M. Woodley, *Chem Rev*, 2018, **118**, 801–838.

3 P. T. Anastas and J. C. Warner., *Green chemistry: Theory and practice*, 1998, **29**, 14821–14842.

4 I. T. Horváth and P. T. Anastas, *Chem Rev*, 2007, **107**, 2169–2173.

5 P. T. Anastas, L. B. Bartlett, M. M. Kirchhoff and T. C. Williamson, *Catal Today*, 2000, **55**, 11–22.

6 G. Centi and S. Perathoner, *Catal Today*, 2003, **77**, 287–297.

7 J. H. Clark, *Pure and Applied Chemistry*, 2001, **73**, 103–111.

8 P. Anastas and N. Eghbali, *Chem Soc Rev*, 2010, **39**, 301–312.

9 M. Alcalde, M. Ferrer, F. J. Plou and A. Ballesteros, *Trends Biotechnol*, 2006, **24**, 281–287.

10 M. T. Reetz, *J Am Chem Soc*, 2013, **135**, 12480–12496.

11 P. Lozano and E. García-Verdugo, *Green Chemistry*, 2023, **25**, 7041–7057.

12 S. Wenda, S. Illner, A. Mell and U. Kragl, *Green Chemistry*, 2011, **13**, 3007–3047.

13 R. A. Sheldon, *Green Biocatalysis*, 2016, 1–15.

14 A. R. Alcántara, P. Domínguez de María, J. A. Littlechild, M. Schürmann, R. A. Sheldon and R. Wohlgemuth, *ChemSusChem*, 2022, **15**, e202102709.

15 J. M. Woodley, *Curr Opin Chem Biol*, 2013, **17**, 310–316.

16 A. S. Bommarius, J. K. Blum and M. J. Abrahamson, *Curr Opin Chem Biol*, 2011, **15**, 194–200.

17 S. Luetz, L. Giver and J. Lalonde, *Biotechnol Bioeng*, 2008, **101**, 647–653.

18 C. Garcia-Galan, Á. Berenguer-Murcia, R. Fernandez-Lafuente and R. C. Rodrigues, *Adv Synth Catal*, 2011, **353**, 2885–2904.

19 M. D. Truppo, *ACS Med Chem Lett*, 2017, **8**, 476–480.

20 L. Leemans Martin, T. Peschke, F. Venturoni and S. Mostarda, *Curr Opin Green Sustain Chem*, 2020, **25**, 100350.

21 J. P. Adams, M. J. B. Brown, A. Diaz-Rodriguez, R. C. Lloyd and G. D. Roiban, *Adv Synth Catal*, 2019, **361**, 2421–2432.

22 G. Cruz, J. Acosta, J. Del Arco, V. J. Clemente-Suarez, V. Deroncele and J. Fernández-Lucas, *ChemCatChem*, 2022, **14**, e202200140.

23 J. M. Woodley, *Appl Microbiol Biotechnol*, 2019, **103**, 4733–4739.

24 Y. Bai, H. Huang, K. Meng, P. Shi, P. Yang, H. Luo, C. Luo, Y. Feng, W. Zhang and B. Yao, *Food Chem*, 2012, **131**, 1473–1478.

25 C. R. Gomes-Ruffi, R. H. da Cunha, E. L. Almeida, Y. K. Chang and C. J. Steel, *LWT - Food Science and Technology*, 2012, **49**, 96–101.

26 O. Kirk, T. V. Borchert and C. C. Fuglsang, 2002, **13**, 345–351.

27 J. Schückel, A. Matura and K. H. van Pée, *Enzyme Microb Technol*, 2011, **48**, 278–284.

28 T. K. Hakala, T. Liitiä and A. Suurnäkki, *Carbohydr Polym*, 2013, **93**, 102–108.

29 S. Nisha, A. K. S and N. Gobi, *Chemical Science Review and Letters*, 2012, **1**, 148–155.

30 I. M. Apetrei, M. L. Rodriguez-mendez, C. Apetrei and J. A. De Saja, *Sens Actuators B Chem*, 2013, **177**, 138–144.

31 A. Basso and S. Serban, *Molecular Catalysis*, 2019, **479**, 110607.

32 S. Feng, H. Hao Ngo, W. Guo, S. Woong Chang, D. Duc Nguyen, D. Cheng, S. Varjani, Z. Lei and Y. Liu, *Bioresour Technol*, 2021, **335**, 125278.

33 M. Razzaghi, A. Homaei, F. Vianello, T. Azad, T. Sharma, A. K. Nadda, R. Stevanato, M. Bilal and H. M. N. Iqbal, *Bioprocess Biosyst Eng*, 2022, **45**, 237–256.

34 J. M. Nelson and E. G. Griffin, *J Am Chem Soc*, 1916, **38**, 1109–1115.

35 S. Bahri, A. Homaei and E. Mosaddegh, *Colloids Surf B Biointerfaces*, 2022, **218**, 112754.

36 Y. R. Maghraby, R. M. El-Shabasy, A. H. Ibrahim and H. M. E. S. Azzazy, *ACS Omega*, 2023, **8**, 5184–5196.

37 G. Ferna, M. Terreni, C. Mateo, A. Bastida and R. Ferna, *Enzyme Microb Technol*, 2001, **28**, 389–396.

38 M. Besharati, A. A. Saboury, A. A. Poostchi and A. M. Rashidi, *Int J Biol Macromol*, 2018, **106**, 1314–1322.

39 D. Liu and C. Dong, *Process Biochemistry*, 2020, **92**, 464–475.

40 G. Marrazza, *Biosensors (Basel)*, 2014, **4**, 301–317.

41 Q. Shen, R. Yang, X. Hua, F. Ye, W. Zhang and W. Zhao, *Process Biochemistry*, 2011, **46**, 1565–1571.

42 S. Gao, Y. Wang, X. Diao, G. Luo and Y. Dai, *Bioresour Technol*, 2010, **101**, 3830–3837.

43 L. S. Wong, J. Thirlway and J. Micklefield, *J Am Chem Soc*, 2008, **130**, 12456–12464.

44 T. Jesionowski, Z. Jakub and B. Krajewska, *Adsorption*, 2014, **20**, 801–821.

45 D. Brady and Æ. J. Jordaan, *Biotechnol Lett*, 2009, **31**, 1639–1650.

46 B. Brena, P. González-Pombo and F. Batista-Viera, in *Springer Media: New York*, 2013, vol. 78, pp. 15–31.

47 N. R. Mohamad, N. H. C. Marzuki, N. A. Buang, F. Huyop and R. A. Wahab, *Biotechnology and Biotechnological Equipment*, 2015, **29**, 205–220.

48 L. Chitradon, P. Mahakhan and C. Bucke, *J Mol Catal B Enzym*, 2000, **10**, 273–280.

49 D. A. M. Urrea, A. V. F. Gimenez, Y. E. Rodriguez and E. M. Contreras, *Process Safety and Environmental Protection*, 2021, **156**, 134–143.

50 A. Vetrano, F. Gabriele and N. Spreti, *ChemBioChem*, 2023, **24**, e202300456.

51 A. Vetrano, F. Gabriele, R. Germani and N. Spreti, *New Journal of Chemistry*, 2022, **46**, 10037–10047.

52 Y. Weng, G. Yang, Y. Li, L. Xu, X. Chen, H. Song and C. X. Zhao, *Adv Colloid Interface Sci*, 2023, **318**, 102957.

53 E. Kurzbaum, Y. Raizner, M. E. Kuc, A. Kulikov, B. Hakimi, L. I. Kruh and O. Menashe, *Environmental Technology (United Kingdom)*, 2020, **41**, 2875–2883.

54 H. Ertesvåg and S. Valla, *Polym Degrad Stab*, 1998, **59**, 85–91.

55 L. Cao, W. Lu, A. Mata, K. Nishinari and Y. Fang, *Carbohydr Polym*, 2020, **242**, 116389.

56 A. D. Augst, H. J. Kong and D. J. Mooney, *Macromol Biosci*, 2006, **6**, 623–633.

57 K. Y. Lee and D. J. Mooney, *Prog Polym Sci*, 2012, **37**, 106–126.

58 L. Shapiro and S. Cohen, *Biomaterials*, 1997, **18**, 583–590.

59 Y. Weng, G. Yang, Y. Li, L. Xu, X. Chen, H. Song and C. X. Zhao, *Adv Colloid Interface Sci*, 2023, **318**, 102957.

60 R. Ahmad Raus, W. M. F. Wan Nawawi and R. R. Nasaruddin, *Asian J Pharm Sci*, 2021, **16**, 280–306.

61 D. Li, Z. Wei and C. Xue, *Compr Rev Food Sci Food Saf*, 2021, **20**, 5345–5369.

62 D. Wang, R. Lv, X. Ma, M. Zou, W. Wang, L. Yan, T. Ding, X. Ye and D. Liu, *Food Hydrocoll*, 2018, **83**, 1–8.

63 B. B. Lee, P. Ravindra and E. S. Chan, *Chem Eng Technol*, 2013, **36**, 1627–1642.

64 B. Zeeb, A. H. Saberi, J. Weiss and D. J. McClements, *Food Hydrocoll*, 2015, **50**, 27–36.

Chapter 2

Exploring Enzymes

2.1 Lipases

Lipases, classified as serine hydrolases, fall into the category of triacylglycerol acyl hydrolases (E.C. 3.1.1.3) and can be distinguished from esterases based on their substrate specificity. A fundamental criterion to distinguish between these two types of enzymes is the phenomenon of interfacial activation: in the absence of an interface between an organic and an aqueous phase, the active site of lipases remains concealed by a secondary structure, rendering it inaccessible to the substrate. However, in the presence of a hydrophobic interface, lipases undergo a significant conformational rearrangement, passing into an active state. This characteristic is exhibited by a substantial number of lipases but not by esterases. Remarkably, lipases have evolved exceptionally stable structures that enable them to endure the denaturing effects of interfaces and can even withstand exposure to organic solvents[1]. Lipases play several roles in food and fat degradation, are investigated for their potential use in the treatment of digestive disorders and pancreatic disease and are very promising in the field of biotransformation. This subject is well-documented and offers a plethora of examples, spanning from hydrolysis in aqueous environments to synthetic applications in organic solvents[2]. Lipases exhibit catalytic capabilities across a range of reactions, including esterification, transesterification, and interesterification, as illustrated in Figure 1[3].

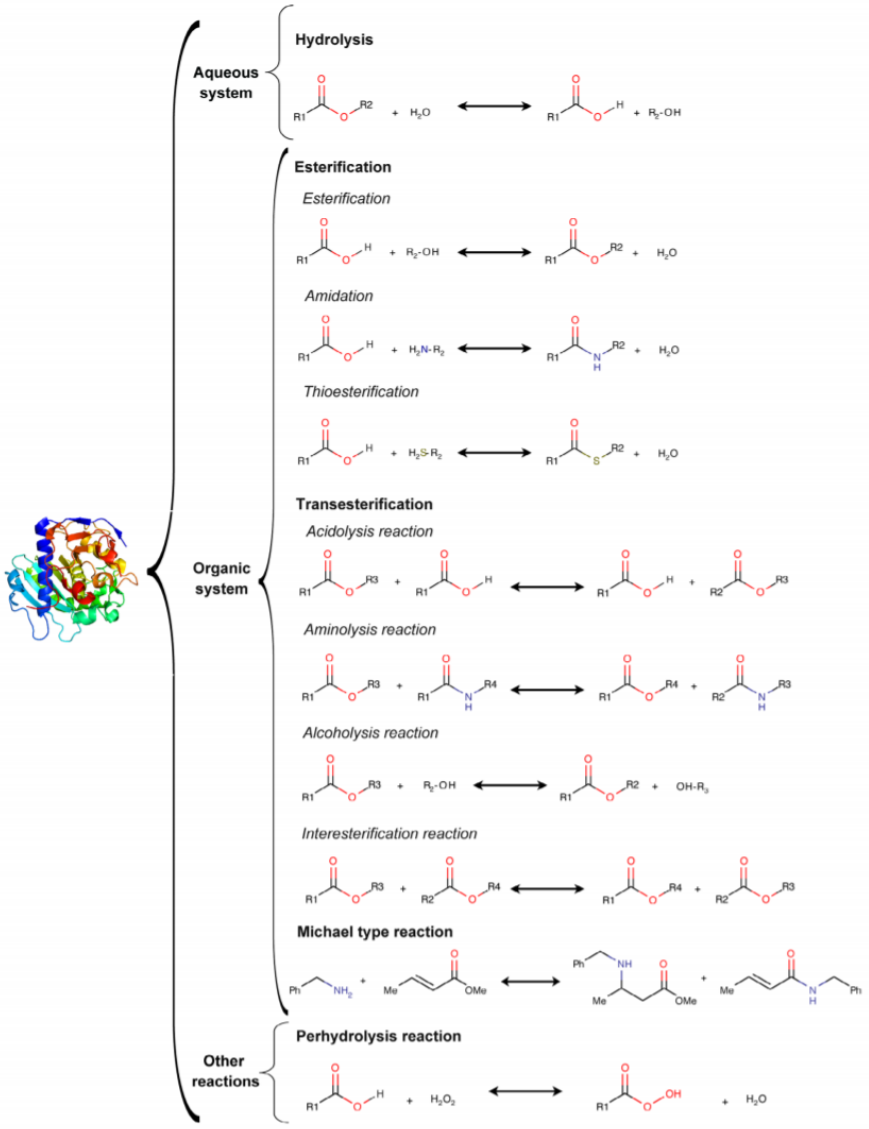

Figure 1: Reactions catalyzed by lipases.

Moreover, they can operate under extreme conditions of temperature (if sourced from thermophiles)[4], pH (if derived from acidophilic or alkaliphilic organisms), and in environments with high salt concentrations (if extracted from halophiles)[5]. These remarkable attributes underline the vast potential and versatility of lipases in various biotechnological applications. Lipases

belong to the enzyme superfamily known as α/β-hydrolases. They consist of a central core featuring secondary β-strands structures intertwined with α-helices. With the exception of lipase B from *Candida antarctica*, all lipases exhibit a conserved pentapeptide sequence Gly-X-Ser-X-Gly surrounding the active nucleophilic serine residue. This arrangement forms a distinct β-turn-α motif termed the "nucleophilic elbow"[6]. The active site of lipases comprises a catalytic triad composed of serine, histidine, and aspartic or glutamic acid. From a chemical perspective, lipases resemble proteases, differing mainly in the structure of their active sites. This distinction lies in the orientation of the hydroxyl group of the catalytic serine, resulting in an inverse stereochemistry of the respective catalytic triads[7]. Although the lid domain is a universal feature found in almost all lipases, its structure can vary considerably [8]. Figure 2 shows the common structural properties of lipases.

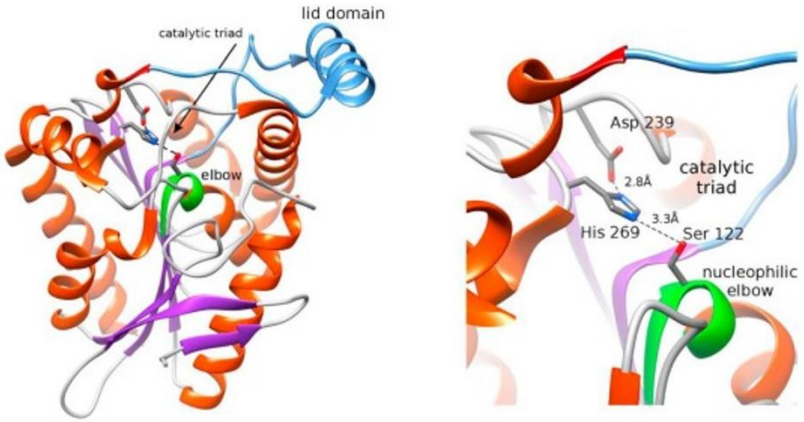

Figure 2: Lipase structure (catalytic triad, nucleophilic elbow and lid domain).

Furthermore, there are four distinct binding pockets tailored for triglycerides. The first pocket is an oxyanion hole, due to the interaction of two backbone

amides from a residue in the lipase's N-terminal region and the adjacent C-terminal region of the catalytic serine. The remaining three pockets facilitate the entry of fatty acids, accommodating them at Sn-1, Sn-2, and Sn-3 positions[9]. In the literature, lipases are classified based on the geometry of their binding sites. They are commonly divided into three categories: lipases with a hydrophobic slit-like binding site (lipases from *Rhizomucor* and *Rhizopus*), lipases with a funnel-like binding site (lipases from *Candida antarctica*), and lipases with a tunnel-like binding site (lipase from *Candida rugosa*)[10].

2.1.1 *Candida Rugosa* Lipase

Candida rugosa lipase (CRL) is one of the most widely employed enzymes in its class for executing biotransformations. This type of enzyme was initially characterized in the 1960s through the isolation of yeast from natural soil sources. Initially, two isoenzymes, designated LipA and LipB, were identified, purified, and subjected to genetic characterization. Subsequently, this nomenclature gave way to a numerical system, starting with Lip1 and extending to Lip7. At least seven genes contribute to the production of CRL, with comprehensive characterization available for five of them (Lip1 - Lip5)[11,12]. All the identified isoenzymes share a uniform composition, consisting of 534 amino acids, and exhibit a structural homology greater than 70%. Similar to other lipases, these isoenzymes belong to the α/β-hydrolase family, characterized by a catalytic triad comprising Ser-209, Glu-341, and His-449, alongside a protective lid structure that shields the active site when the enzyme is in its inactive state[13]. However, the lid structure is mainly characterized by a disulfide bond, established between Cys-60 and Cys-97, and an ionic interaction formed between Glu-96 and Arg-37. Figure 3

provides a visual representation of the conformational changes induced by the lid's opening.

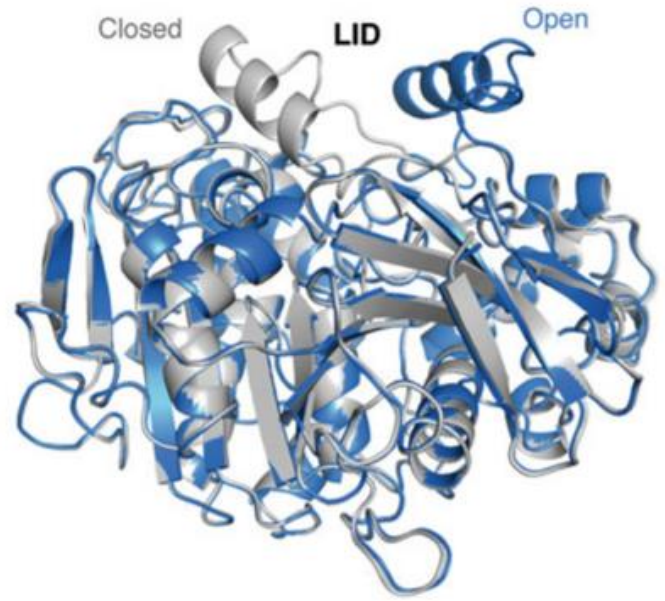

Figure 3: Overlap of the CRL in its active form (lid opened-blue) and its inactive form (lid closed-grey).

A noteworthy structural feature concerns the rotation of the amino acids Glu-66 and Pro-92, which is facilitated by a *cis-trans* isomerization of the peptide bond at Pro-92[14]. When the lid is in its open configuration, it achieves greater thermodynamic stability, thanks to the hydrophobic interactions established between the amino acids of the lid and the external lipophilic environment. Structural variations in the lid exist among different isoforms, contributing to varying catalytic activities[15]. Notable disparities are evident when comparing the lid structures of Lip1 and Lip3. For instance, π-stacking interactions between Phe-344 and Phe-87, as well as between Phe-344 and Tyr-69, are present exclusively in the Lip1 isoenzyme. Furthermore, the hydrogen bond between Ser-84 and Ser-450, observed in Lip1, cannot form in Lip3 due to

the replacement of Ser-450 with Ala-450 in this isoform[16]. Consequently, the lid of Lip1 exhibits greater stability than that of Lip3, although the latter shows greater mobility. This structural divergence results in Lip3 being more effective in esterifying bulkier substrates due to its greater degree of flexibility[17]. As previously described, CRL features a tunnel responsible for recognition of substrate hydrophobic chain, which begins near Ser-209 and extends inward under the lid. This L-shaped cavity boasts a total length of approximately 25 Å and possesses the ability to accommodate different types of substrates. Figure 4 provides a visual representation of the 3D structure of *C. rugosa* Lip3 isoenzyme (CRL3)[18,19].

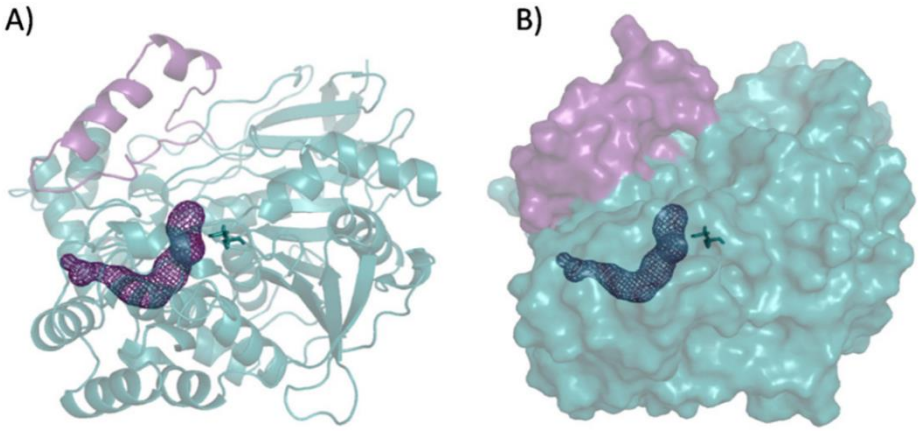

Figure 4 : 3D Structure of CRL3, the α-helices forming the lid are colored in magenta and the intramolecular tunnel is represented by a mesh.

Due to its wide-ranging substrate specificity, *Candida rugosa* lipase has gained prominence within the industrial sector. It finds successful application in a variety of reactions, including hydrolysis, esterification, and even enantioselective processes. Owing to these exceptional characteristics, it acts as a valuable biocatalyst in drug synthesis, aroma production, as well as in the perfumery and cosmetic industries[20].

2.1.2 *Candida antarctica* lipase B

Candida antarctica lipase B (CALB) is composed of 317 amino acid residues and has a molecular weight of 33.273 KDa. Its amino acid sequence and crystallographic structure were first described in 1994. The protein has approximate dimensions of about 30x40x50 Å and belongs to the α-β globular protein type. The structure comprises 10 α-helices and 9 β-strands[21]. Notably, a prominent feature of the secondary structure is the prevalence of β-α-β motifs in most connections. Helices α5 and α10 are particularly significant as they predominantly constitute the active site pocket and play a crucial role in substrate recognition. The catalytic triad consists of Ser-105, Asp-187, and His-224, as depicted in Figure 5. This discovery was pivotal because it allowed to draw analogies with other known lipases, all of which shared the same residues as essential components of the active site.

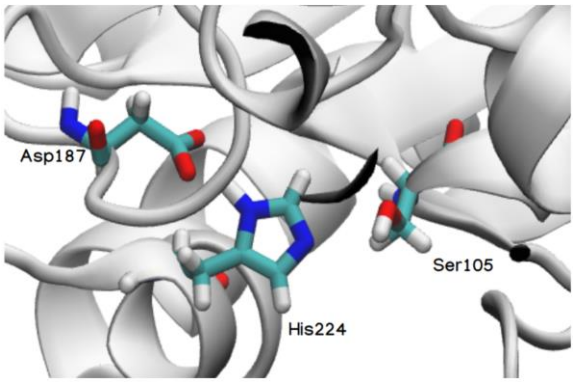

Figure 5: CALB catalytic triad.

The catalytic serine (Ser-105) is positioned just before α4, immediately following β4. However, this region exhibits a rather unique characteristic: the absence of the Gly-X-Ser-X-Gly sequence. This feature distinguishes CALB from other lipases of the same family. Another distinguishing feature is the absence of a real lid, in the case of CALB its presence is debated, and it has

been concluded that it possesses a small one. Specifically, CALB has a threonine residue in place of the first glycine. It remains uncertain whether the glycine-threonine substitution results from a different helical orientation, providing more space at that point, or if the presence of the bulkier residue leads to a change in helical orientation. The catalytic histidine (His-224) is located at the beginning of α9, while the third residue, aspartate (Asp-187), is found just after β6, as commonly observed in other lipases. Figure 6 illustrates the residues of primary interest described above[22].

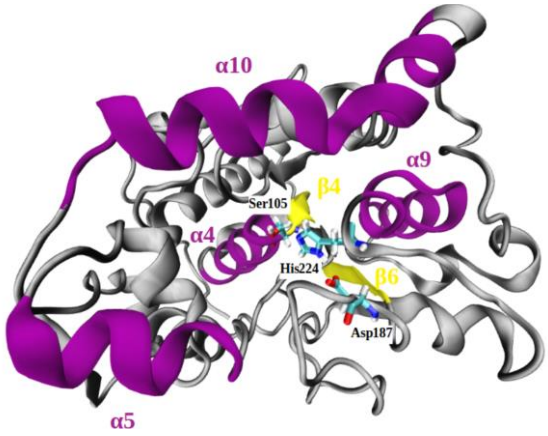

Figure 6: Crystallographic structure of CALB - PDB: 1TCA.

Another crucial region is the oxyanion hole, which serves as a pocket capable of stabilizing the negative charge of the tetrahedral intermediate. Typically, this feature consists of residues with nitrogen atoms strategically positioned to form hydrogen bonds with the substrate. In the case of CALB, as depicted in Figure 7, two residues, namely Gln-106 and Thr-40, fulfill this role[23].

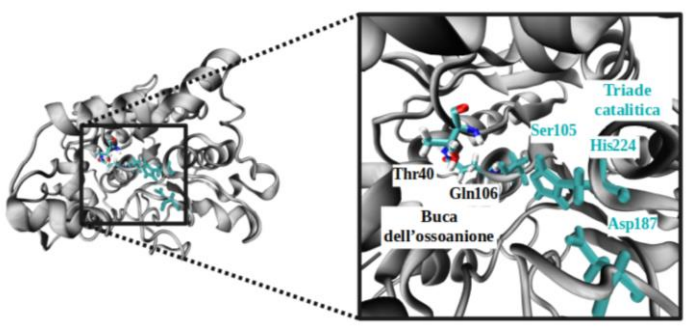

Figure 7: Crystallographic structure of CALB with magnification of the catalytic triad and the oxyanion hole.

The active site is surrounded by two α-helixes, namely α5 and α10, which have been shown to be very flexible regions. Despite the size of the lid, CalB is still considered an interfacial enzyme that exhibits the phenomenon of interfacial activation by conformational change of the α5 helix: a highly open conformation of this helix is required to bind bulky substrates, and this is favored in a hydrophobic environment[24–26].

2.2 Alcohol Dehydrogenases

The alcohol dehydrogenase (ADH) family includes multiple enzymes capable of catalyzing the reversible oxidation of a wide range of primary and secondary alcohols, leading to the formation of corresponding aldehydes and ketones[27]. The precise functional roles of ADHs are not yet fully understood. However, based on their catalytic activities, it is suggested that ADHs play a role in various metabolic processes, including the metabolism of steroids, retinoids, lipid peroxidation products, hydroxy fatty acids, as well as xenobiotic alcohols and aldehydes. Among the members of the ADH family, ADH3, also known as formaldehyde dehydrogenase (FDH), is a noteworthy enzyme. It is the only member within the family that has a known

physiological substrate, specifically S-hydroxymethylglutathione, and it functions as an effective formaldehyde scavenger. Its widespread presence and conserved structure suggest its crucial role in living organisms[28]. In the context of alcohol metabolism, ADH1 is the main enzyme responsible for metabolizing ingested ethanol, while ADH4 is primarily involved in the initial metabolism of ethanol in the stomach. The ADH system can be considered a significant detoxification mechanism for alcohols and aldehydes. When ethanol is converted into acetaldehyde, the process is coupled with the reduction of NAD^+ to NADH, resulting in an altered NAD^+/NADH ratio. This alteration is responsible for many of the metabolic effects associated with ethanol consumption[29]. Liver alcohol dehydrogenase is a member of the large superfamily known as medium-chain dehydrogenases/reductases (MDRs), which boasts an impressive list of nearly 11000 members [30,31]. These MDR proteins are delineated by their dual-domain structure, characterized by a C-terminal domain housing the coenzyme-binding Rossmann fold and an N-terminal domain responsible for substrate binding. These domains are divided by a cleft with a deep pocket, facilitating the interaction between the cofactor and the active site[32]. Before 1999, vertebrate ADHs (EC 1.1.1.1) were classified into seven distinct classes based on sequence alignment, catalytic properties, and other distinguishing features. However, the primary forms of mammalian enzymes are dimeric, with each subunit having a molecular mass of 40 kDa and two tightly bound zinc ions. Each subunit within the dimeric enzyme comprises two domains: the catalytic domain and the coenzyme-binding domain. The catalytic domain is larger and hosts the substrate-binding zinc ion, along with all the amino acid residues crucial for participating in the catalyzed reaction[33].

2.2.1 Horse liver alcohol dehydrogenase

Horse liver alcohol dehydrogenase (HLADH) is a well-documented enzyme that has played a prominent and influential role in the fields of enzymology and biochemistry[34]. This enzyme, isolated from the horse liver tissue, has been the subject of extensive research due to its central involvement in alcohol metabolism and its broader relevance in enzymatic processes. HLADH has been used as a paradigmatic system for gaining insights into the structure and function of alcohol dehydrogenases as a whole. Numerous investigations have delved into its catalytic mechanism, substrate specificity, and kinetic properties[35,36]. Furthermore, the elucidation of the three-dimensional structure of HLADH, achieved through X-ray crystallography, has provided valuable information on its active site and catalytic mechanism. As depicted in Figure 8, the crystallographic structure portrays the configuration of the two chains, denoted as A and B.

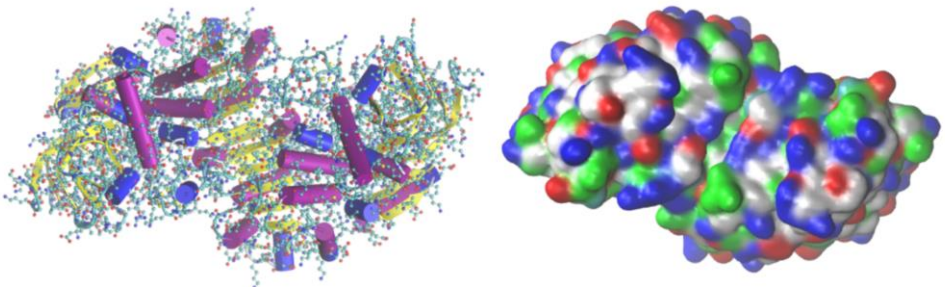

Figure 8: The crystallographic structure of horse liver alcohol dehydrogenase (HLADH - PDB: 7K35) with the protein's secondary structure highlighted on the left and the residue types displayed on the right. On the left side, alpha helices are depicted in violet, 3.10 helices in blue, coils in white, turns in light blue, and extended beta sheets in yellow. On the right side, non-polar residues are denoted in white, polar ones in green, acidic residues in red, and basic ones in blue.

HLADH, classified as a metalloenzyme, is structured as a homodimer, where each monomer consists of 374 amino acid residues, contributing to a

substantial molecular weight of 163.32 kDa. Within the active site, there are two zinc atoms, each of which plays distinct roles. One of these zinc atoms performs a catalytic function, and it is coordinated with Cys-46, Cys-174, His-67, and water in the apoenzyme state. In the holoenzyme state, it binds to the substrate. The other zinc atom, known as structural zinc, is bonded to four cysteine residues[37]. Notably, the electron densities surrounding both the catalytic and structural zinc ions adopt a nearly spherical shape, with the catalytic zinc exhibiting a tetrahedral coordination arrangement. The zinc structural site of ADH has been assigned a role in the maintenance of a proper tertiary/quaternary structure. Related enzymes not containing this zinc ion, like sorbitol dehydrogenase, display a different quaternary structure[38,39], and recombinant variants of ADH where one Cys ligand at the time has been changed to Ala, are structurally labile[40]. Approximately sixty years ago, Theorell and Chance laid the groundwork by proposing a mandatory sequence for binding, starting with the coenzyme and followed by the substrate[41]. In their initial publication on the crystal structure of HLADH in 1973, Brånden and colleagues[42] detailed a substructure responsible for coenzyme binding, comprising roughly 120 amino acids within each subunit. The structural motif of this protein, characterized by beta/alpha/beta folds, is now recognized as the Rossmann fold[43]. In each HLADH coenzyme-binding subunit, there are two of these folds, one for each nucleotide in NAD. This arrangement relies on a combined system of hydrophobic interactions and hydrogen bonds involving more than 20 amino acid residues[44]. The positioning of NAD together with HLADH is depicted in Figure 9.

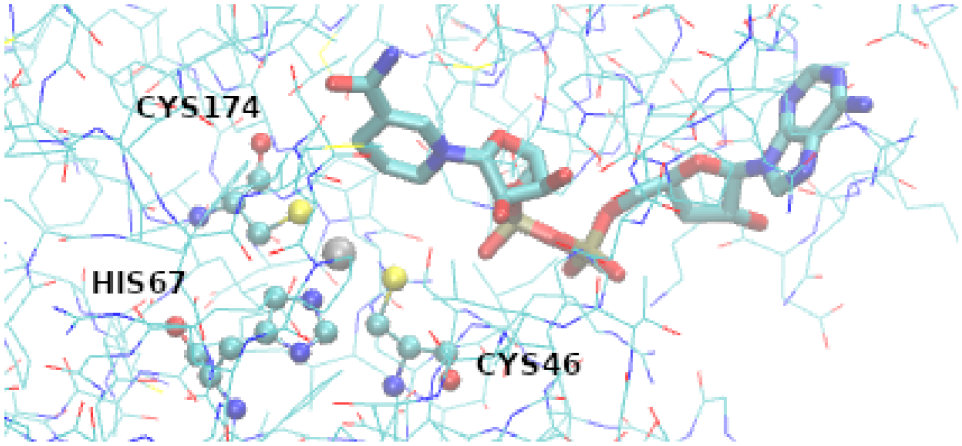

Figure 9: Catalytic site of horse liver alcohol dehydrogenase with NADH molecule.

Within this complex, the adenine base is nestled in a hydrophobic cleft, with the amino group at position 6 extending outward the protein surface. Consequently, it is the only part of the coenzyme exposed to the surrounding solvent. Both the adenosine and nicotinamide riboses form hydrogen bonds within the cavity with the Asp-223 and Lys-228 side chains and with the main carbonyl chain via Ser-48 and His-5144, respectively. The NAD pyrophosphate connects via hydrogen bonds to the main peptide chain via two arginine residues, namely Arg-47 and Arg-369. The nicotinamide component interacts with the main chain via hydrogen bonds formed by its amine group. Moreover, it is positioned precisely close to the active site due to hydrophobic interactions with the side chains of Val-203, Val-292 and Thr-178, all of which remain in contact with the non-reactive side of the ring. The other side of the ring is oriented toward the active site near the catalytic zinc ion[45]. The binding of the coenzyme triggers a substantial conformational change in the protein. Alcohol dehydrogenase was the first enzyme in which domain rotations were experimentally demonstrated. In the apoenzyme state, the central cleft is open to solvent and ligands. However, in the

holoenzyme state, the cleft is sealed by the relative movement of the domains. To move from the apoenzyme to the holoenzyme structure, the catalytic domain of HLADH undergoes a rotation of about 10 degrees[46]. This motion leads to the expulsion of residual water from the catalytic site and the establishment of a hydrophobic environment necessary for the hydride transfer. The conformational shift induced by coenzyme binding specifically requires the presence of the nicotinamide moiety of NAD, whereas the binding of ADP-ribose does not induce such a change[47]. For a long time, the binuclear zinc ion center of HLADH remained the primary focus of attention in studying the catalytic mechanism of this enzyme. However, this focus has shifted to the structural changes that accompany coenzyme binding and domain rotations. Understanding these structural dynamics is crucial to elucidate the enzyme's catalytic function and the complexity of its interactions with the substrate.

References

1 R. D. Schmid and R. Verger, *Angewandte Chemie*, 1998, **37**, 1608–1633.

2 S. Hari Krishna and N. G. Karanth, *Catal Rev Sci Eng*, 2002, **44**, 499–591.

3 E. Castillo, L. Casas-Godoy and G. Sandoval, *Biocatalysis*, 2016, **1**, 178–188.

4 N. A. Soliman, M. Knoll, Y. R. Abdel-Fattah, R. D. Schmid and S. Lange, *Process Biochemistry*, 2007, **42**, 1090–1100.

5 E. Leuisse, K. Schanck and C. Colson, *Eur J Biochem*, 1993, **216**, 155–160.

6 J. D. Schrag and M. Cygler, *Methods Enzymol*, 1997, **284**, 85–107.

7 Dodson, Guy G. and D. M. Lawson, *Faraday Discuss*, 1992, **93**, 95–105.

8 A. Hjorth, F. Carrière, C. Cudrey, H. Wöldike, E. Boel, D. M. Lawson, F. Ferrato, C. Cambillau, G. G. Dodson and R. Verger, *Biochemistry*, 1993, **32**, 4702–4707.

9 D. A. Lang and B. W. Dijkstra, *Chem Phys Lipids*, 1998, **93**, 115–122.

10 J. Pleiss, M. Fischer and R. D. Schmid, *Chem Phys Lipids*, 1998, **93**, 67–80.

11 S. Brocca, R. Grandori, D. Breviario and M. Lotti, *Curr Genet*, 1995, **28**, 454–457.

12 C. López, N. P. Guerra and M. L. Rúa, *Biotechnol Lett*, 2000, **22**, 1291–1294.

13 M. Holmquist, *Curr Protein Pept Sci*, 2000, **1**, 209–235.

14 M. Cygler and J. D. Schrag, *Biochim Biophys Acta Mol Cell Biol Lipids*, 1999, **1441**, 205–214.

15 N. A. Turner, E. C. Needs, J. A. Khan and E. N. Vulfson, *Biotechnol Bioeng*, 2001, **72**, 108–118.

16 M. A. Pernas, C. López, L. Pastrana and M. L. Rúa, *J Biotechnol*, 2000, **84**, 163–174.

17 M. Pernas, C. López, A. Prada, J. Hermoso and M. L. Rúa, *Colloids Surf B Biointerfaces*, 2002, **26**, 67–74.

18 P. Domínguez De María, J. M. Sánchez-Montero, J. V. Sinisterra and A. R. Alcántara, *Biotechnol Adv*, 2006, **24**, 180–196.

19 J. Barriuso, M. E. Vaquero, A. Prieto and M. J. Martínez, *Biotechnol Adv*, 2016, **34**, 874–885.

20 S. H. Huang, M. H. Liao and D. H. Chen, *Biotechnol Prog*, 2003, **19**, 1095–1100.

21 J. Uppenberg, M. T. Hansen, S. Patkar and T. A. Jones, *Structure*, 1994, **2**, 293–308.

22 J. Uppenberg, N. Ohmer, M. Norin, K. Hult, G. J. Kleywegt, S. Patkar, V. Waagen, T. Anthonsen and T. A. Jones, *Biochemistry*, 1995, **34**, 16838–16851.

23 M. Galmés, E. García-Junceda, K. Świderek and V. Moliner, *ACS Catal*, 2020, **10**, 1938–1946.

24 B. Luan and R. Zhou, *Physical Chemistry Chemical Physics*, 2017, **19**, 15709–15714.

25 T. Zisis, P. L. Freddolino, P. Turunen, M. C. F. Van Teeseling, A. E. Rowan and K. G. Blank, *Biochemistry*, 2015, **54**, 5969–5979.

26 C. C. Gruber and J. Pleiss, *J Mol Catal B Enzym*, 2012, **84**, 48–54.

27 G. Duester, J. Farrés, M. R. Felder, R. S. Holmes, J. O. Höög, X. Parés, B. V. Plapp, S. J. Yin and H. Jörnvally, *Biochem Pharmacol*, 1999, **58**, 389–395.

28 J. O. Höög, J. J. Hedberg, P. Strömberg and S. Svensson, *J Biomed Sci*, 2001, **8**, 71–76.

29 C. S. Lieber, *Alcohol Clin Exp Res*, 1999, **23**, 991–1007.

30 B. Persson, J. Hedlund and H. Jörnvall, *Cellular and Molecular Life Sciences*, 2008, **65**, 3879–3894.

31 B. Persson, J. S. Zigler and H. Jörnvall, *Eur J Biochem*, 1994, **226**, 15–22.

32 C. A. Staab, M. Hellgren and J. O. Höög, *Cellular and Molecular Life Sciences*, 2008, **65**, 3950–3960.

33 G. Pettersson, *CRC Crit Rev Biochem*, 1987, **21**, 349–389.

34 H. Jørnvall, *Eur J Biochem*, 1970, **16**, 25–40.

35 H. Eklund, B. V. Plapp, J. P. Samama and C. I. Brändén, *Journal of Biological Chemistry*, 1982, **257**, 14349–14358.

36 D. Giacomini, P. Galletti, A. Quintavalla, G. Gucciardo and F. Paradisi, *Chemical Communications*, 2007, 4038–4040.

37 G. Schneider, H. Eklund, E. Cedergren-Zeppezauer and M. Zeppezauer, *EMBO J*, 1983, **2**, 685–689.

38 J. Jeffery, J. Chesters, C. Mills, P. J. Sadler and H. Jörnvall, *EMBO J*, 1984, **3**, 357–360.

39 H. Jornvall, H. von Bahr-Lindstrom and J. Jeffrey, *Eur J Biochem*, 1984, **140**, 17–23.

40 J. Jeloková, C. Karlsson, M. Estonius, H. Jörnvall and J. -O Höög, *Eur J Biochem*, 1994, **225**, 1015–1019.

41 K. Dalziel, *Biochem J*, 1962, **84**, 244–254.

42 C. I. Branden, H. Eklund, B. Nordstrom, T. Boiwe, G. Söderlund, E. Zeppezauer, I. Ohlsson and A. Akeson, *Proc Natl Acad Sci U S A*, 1973, **70**, 2439–2442.

43 S. T. Rao and M. G. Rossmann, *J Mol Biol*, 1973, **76**, 241–256.

44 S. Ramaswamy, H. Eklund and B. V. Plapp, *Biochemistry*, 1994, **33**, 5230–5237.

45 J. K. Rubach and B. V. Plapp, *Biochemistry*, 2003, **42**, 2907–2915.

46 A. Dołega, *Coord Chem Rev*, 2010, **254**, 916–937.

47 B. V. Plapp, *Arch Biochem Biophys*, 2010, **493**, 3–12.

Chapter 3

Experimental and Computational Techniques

3.1 Microscopy

Microscopy is a fundamental tool in the field of scientific research, enabling us to explore the intricate world of the very small. It is a technique that allows scientists and researchers to visualize and study objects, structures, and phenomena at the micro- and nanoscale, which are often beyond the reach of the naked eye. Microscopy provides valuable insights into the composition, structure, and behavior of various materials and biological samples. It can be broadly categorized into two main divisions: optical microscopy and electron microscopy. These two branches differ in their operating principles and the resolution scale they offer. Optical microscopy, also known as light microscopy, relies on visible light and a series of lenses to magnify and visualize specimens. It is a versatile and widely used tool for examining biological samples, materials, and surfaces at relatively low magnifications. Optical microscopes come in various forms, including bright-field, phase-contrast, and fluorescence microscopy, each tailored to specific applications. On the other hand, electron microscopy uses a focused beam of electrons to achieve much higher resolution and greater magnification than optical microscopy. This division includes transmission electron microscopy (TEM) and scanning electron microscopy (SEM), which are indispensable in the study of ultrafine structures and materials, as well as in the life sciences. These two divisions of microscopy, optical and electronic, serve as powerful tools that complement each other in scientific

investigations, offering a wide range of applications in various disciplines, from biology and materials science to chemistry and physics[1].

3.1.1 Stereomicroscopy

The stereomicroscope, often referred to as a stereoscopic microscope, is a specialized optical instrument meticulously engineered to provide binocular vision, thus offering a three-dimensional perception of the specimen under examination. Unlike traditional microscopes, which rely on transmitted light, stereomicroscopes predominantly utilize reflected light, making them particularly advantageous for scrutinizing thicker and bulkier samples that might pose challenges for transmission microscopes. Two prominent magnification systems are commonly employed in stereoscopic microscopy. The first is known as “fixed magnification”. In this configuration, magnification is achieved by pairing two objective lenses, each with a predetermined and unchangeable magnification factor. This design offers a set magnification level that remains constant throughout the observation. Conversely, the second system is termed “variable magnification”. This innovative approach enables users to seamlessly adjust the magnification level within a predefined range, providing greater flexibility in the examination process.

3.1.2 Scanning Electron Microscopy (SEM)

Electron microscopy operates in a quite analogous manner to the principles governing optical microscopy, which relies on photons for imaging. The fundamental determinant of the resolution of an imaging instrument is the wavelength of the particles it employs as probes. In this context, electron microscopy enjoys a significant advantage, as the wavelength of electrons is markedly smaller than that of photons. Consequently, electron

microscopes provide approximately 1000 times higher resolution than optical microscopes[2]. The electron beam utilized in electron microscopy is generated by an electron source, typically a tungsten filament. This source emits a concentrated stream of primary electrons, which are subsequently shaped, focused, and guided by a series of electromagnetic lenses. An objective lens serves a dual role: it further refocuses the electron beam and exerts precise control over its deflection, enabling the systematic scanning of specific regions on the sample. When the primary electron beam interacts with the sample, a series of intricate processes takes place, depicted in Figure 1.

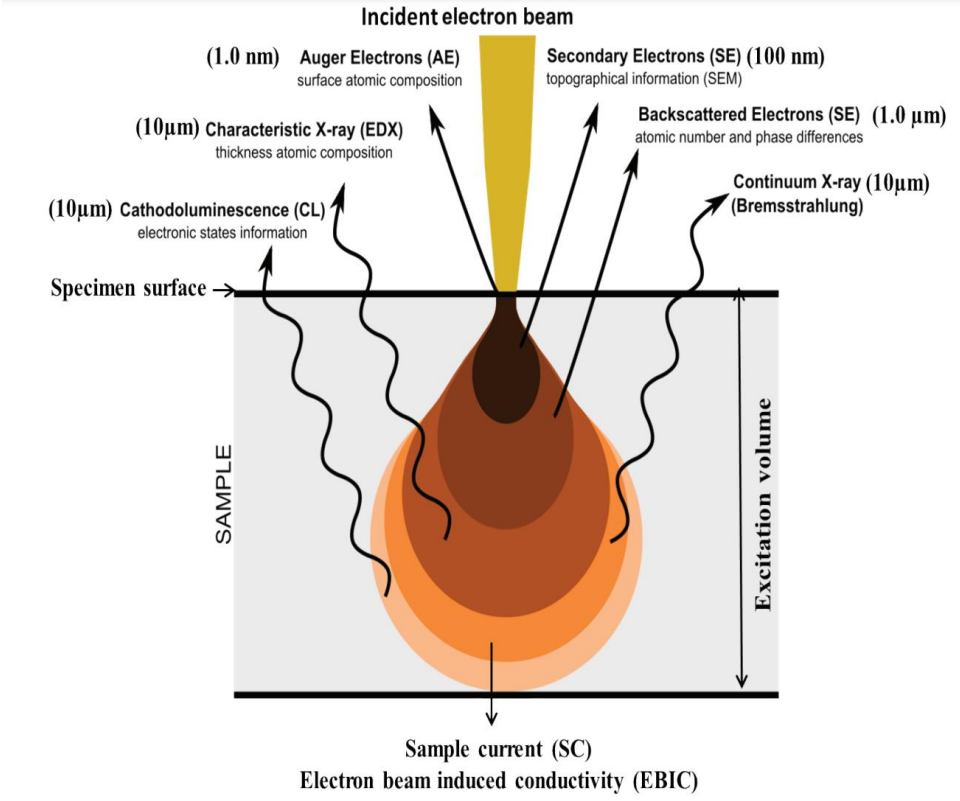

Figure 1: Phenomena induced by the interaction between the electron beam and the sample.

Initially, the electrons lose energy through multiple instances of random scattering and absorption. This occurs within a defined, teardrop-shaped region within the specimen, aptly named the “interaction volume”. The size of this interaction volume ranges from less than 100 nanometers to approximately 10 micrometers below the sample surface. The specific size of the interaction volume depends on several factors, including the landing energy of the electrons, the atomic number of the specimen, and the material density of the specimen itself. The energy exchange between the electron beam and the sample causes several discernible outcomes. Firstly, high-energy backscattered electrons are emitted as a result of elastic scattering. Secondly, low-energy secondary electrons and auger electrons are generated through inelastic scattering. Lastly, the interaction leads to the emission of electromagnetic radiation, encompassing X-rays and cathodoluminescence. Each of these emitted particles or forms of radiation can be detected by specialized detectors tailored to their respective properties. Furthermore, the beam current absorbed by the specimen also becomes a quantifiable parameter that can be detected. This absorbed current is pivotal in generating images that portray the current distribution of the specimen[3]. To facilitate this process, electronic amplifiers of diverse types are employed to enhance the signals collected from the detectors. These amplified signals are subsequently converted into digital images by electronic detectors. Finally, the resulting digital images are displayed on a computer monitor, allowing to visualize and analyze the data with precision and clarity[4].

SEM-EDS

Scanning electron microscopy with energy dispersive X-ray spectrometry (SEM/EDS) is an elemental microanalysis technique widely applied in the field of physical and biological sciences, engineering, technology, and forensic investigations. Electron-excited characteristic X-ray peaks provide identification and quantification of all elements of the periodic table, except H, He, and Li[5]. The underlying principle of this technique revolves around the production of characteristic X-rays through the process of inelastic scattering. This phenomenon occurs when energetic electrons from a focused incident beam, typically confined to a diameter ranging from micrometers to nanometers, interact with the specimen. The energy level of the incident beam is usually chosen within the range between 5 keV to 30 keV. In the early stages of elemental mapping, the instruments relied on wavelength-dispersive X-ray spectrometers (WDS), which are based on Bragg diffraction of X-rays. These diffraction processes take place with both natural crystals and synthetic multi-layer materials. WDS offers several advantages, notably high spectral resolution, and a robust ability to handle a significant volume of data. This is attributed to the brief time required for the flow proportional gas detector to respond, enabling count rates of 10^5 per second and even higher[6].

SEM-Peltier

The presence of a vacuum environment inside a scanning electron microscope (SEM) causes water to evaporate, leading to the dehydration of the sample under investigation. Consequently, the examination of wet samples via scanning electron microscopy requires a specialized methodological approach. To address this challenge, the utilization of

variable-pressure equipment (VP-SEM) and Peltier cooling devices (as depicted in Figure 2) presents a highly practical and efficient technique for the study of wet samples and hydrated systems within the SEM. This methodology allows to overcome the issues of sample dehydration, making it a valuable tool for analyzing specimens in their native, hydrated state[7].

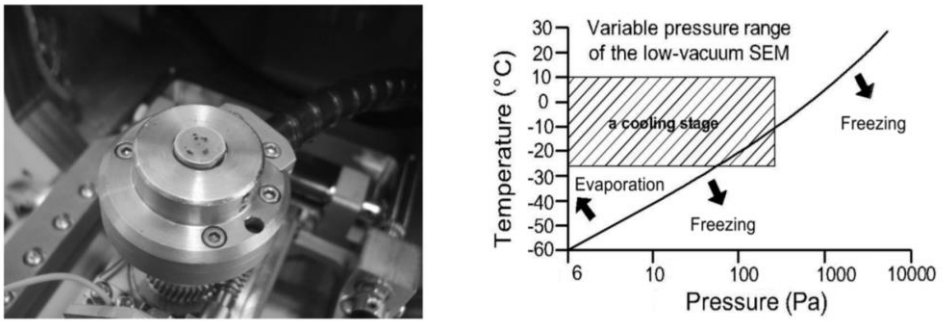

Figure 2: On the left there is an imagine of a Peltier device and on the right its range of cooling.

3.2 Calorimetry

When discussing the thermal analysis of a material, conventionally, it refers to a set of techniques in which a chemical-physical property of the substance under examination is measured as a function of temperature (or time) while the sample is subjected to a controlled and programmed thermal treatment. Differential Scanning Calorimetry (DSC) stands as one of the most commonly used techniques in thermal analysis[8]. Conducted at a constant pressure, the heat change aligns with the enthalpy of the transition, expressed as:

$$\mathrm{C_p} = \left(\frac{\partial \mathrm{H}}{\partial \mathrm{T}}\right)_{\mathrm{p}} \Leftrightarrow \Delta H = \int_{T_i}^{T_f} C_p \cdot \delta T$$

The specific heat (C) is determined as the ratio of the change in heat at constant pressure (Cp) to the mass (m) of the sample under investigation:

$$C = \frac{C_p}{m}$$

By analyzing the thermogram obtained from differential scanning calorimetry, it is possible to quantify the grams of water contained within the samples. The instrument consists of an oven that accommodates two crucibles: one containing the sample to be analyzed and the other left empty for reference. Two thermocouples associated with the crucibles allow the difference in heat between them to be measured over time:

$$\Delta Q = Q_{sample} - Q_{reference}$$

The increase or decrease in temperature must be carefully controlled to always maintain an ideal, constant state of thermal equilibrium between the two crucibles. This ensures that all heat, whether absorbed or released, is attributed solely to the transition under examination[9].

3.3 Chromatographic techniques

Chromatography operates on the principle of separating molecules within a mixture by applying them to a solid or liquid surface, with a stationary phase that remains stable and a mobile phase aiding their movement. The separation process depends on various factors related to the molecules, such as their adsorption (liquid-solid), partition (liquid-solid), and differences in molecular weights[10,11]. These differences lead to some mixture components remaining in the stationary phase moving slowly through the chromatography system, while others rapidly transition to the mobile

phase, exiting the system more quickly. This chromatographic approach revolves around three key components:

- Stationary phase, consisting of a solid material or a liquid layer adhered to a solid support.
- Mobile phase, comprising a liquid or a gaseous element.
- Separate molecules.

The nature of the interactions among the stationary phase, mobile phase, and the substances within the mixture plays a fundamental role in the effective separation of molecules from each other. In chromatography when the mobile phase is a liquid, it is known as liquid chromatography (LC), and when it is a gas, it's called gas chromatography (GC). Gas chromatography is typically employed for analyzing gases, volatile liquid mixtures, and solid materials, while liquid chromatography is particularly useful for thermally unstable and non-volatile samples. Chromatography serves the dual purpose of quantitative analysis and separation. It aims to achieve a satisfactory separation within an appropriate time frame. Various chromatographic methods have been developed for this purpose, including column chromatography, thin-layer chromatography (TLC), paper chromatography, gas chromatography, ion exchange chromatography, gel permeation chromatography, high-pressure liquid chromatography, and affinity chromatography[12].

3.3.1. High-pressure liquid chromatography (HPLC)

HPLC is a chromatographic method that enables rapid structural and functional analysis as well as the purification of various molecules. This technique excels in achieving precise separation and identification of

compounds such as amino acids, carbohydrates, lipids, nucleic acids, proteins, steroids, and other biologically active substances. In HPLC, the mobile phase is forced through columns at pressures ranging from 10 to 400 atmospheres and exhibits a high flow rate typically ranging from 0.1 to 5 cm per second. The use of fine particles and the application of high pressure to control solvent flow significantly enhances the separation capabilities of HPLC, resulting in swift and efficient analysis[13].

3.3.2. Gas Chromatography (GC)

Gas chromatography involves a stationary phase in the form of a column within the device, which houses a liquid stationary phase that adheres to the surface of an inert solid material. This method is referred to as "gas-liquid" chromatography because it relies on gases like helium or nitrogen as the carrier phase. An inert gas acts as the mobile phase, and it is forced through the column at high pressure. The sample to be analyzed is vaporized and introduced into the gaseous mobile phase. The components present in the sample become dispersed between the mobile phase and the stationary phase on the solid support. Gas chromatography is known for its simplicity, versatility, high sensitivity, and rapid application, making it an excellent choice for the precise separation of extremely small molecules. The FID detector is the most widely used in gas chromatography and is highly versatile. In this detector, the column effluent passes through a small flame powered by air and hydrogen. The detection involves monitoring the current generated by the collection of ions and electrons produced during the combustion of analytes. The FID is characterized by high sensitivity, wide linear response range, and low background noise[14].

3.4 UV-VIS Spectroscopy

Spectroscopy measurements, in general, concern the quantitative and qualitative analysis of the interaction between matter (molecules, atoms, ions) and electromagnetic radiation in a wide range of wavelengths, from ultraviolet (UV) to visible (VIS) to infrared (IR) and beyond. Specifically, UV-VIS spectroscopy is a fundamental analytical method for investigating how matter interacts with electromagnetic radiation in the ultraviolet (UV) and visible (VIS) portions of the electromagnetic spectrum. In UV-VIS spectroscopy, it is possible to examine how substances absorb or emit light in the UV and VIS regions, helping to understand electronic transitions in molecules and atoms. This technique is widely employed for identifying compounds and quantifying their concentrations in samples, as each compound exhibits a unique spectral pattern. The instrumentation used is typically UV-VIS spectrophotometers, which measure the light intensity before and after it passes through a sample to obtain absorption or emission spectra. The Lambert-Beer Law is a foundational principle, that allows precise determination of concentration based on absorbance measurements. UV-VIS spectroscopy covers the wavelength range from 190 to 800 nanometers, the UV and VIS ranges are somewhat arbitrarily divided and overlap each other. It seems practical to take the actual or near UV range from 200–400 nm or and the VIS range from 400–800 nm[15]. Overall, UV-VIS spectroscopy is appreciated for its simplicity, versatility, accuracy, and cost-effectiveness, provides rapid results, and plays a crucial role in scientific and industrial laboratories.

3.5 Molecular Mechanics

Molecular Dynamics (MD) encompasses a set of computational techniques that employ the integration of Newton's equations to explore the temporal evolution of atomistic models. The progression of a system over time is visualized as a trajectory, which describes the change in atomic coordinates during the simulation. Molecular dynamics techniques can be broadly categorized into two primary branches: Classical-Mechanics MD, which employs classical physics to describe atomic interactions, and Quantum-Mechanics MD, which utilizes quantum physics for atom-to-atom interactions through ab-initio calculations. In Classical Mechanics or Molecular Mechanics (MM), the focus is solely on atomic nuclei, using simple equations to represent atomic interactions. MM necessitates an initial molecular connectivity, involving a predefined set of bonds between atoms that remains constant throughout the simulation. This approach proves to be extremely advantageous for analyzing structural characteristics of large systems, often comprising thousands of atoms, thanks to its computational efficiency. However, it is not suitable for capturing complex chemical reactions involving the breaking or forming of molecular bonds. In the classical approach, the potential experienced by each atom is a composite of two types of interactions known as bonding (intramolecular) and non-bonding (intermolecular).

$$V(r_N) = V(r_N)_{intra-molecolar} + V(r_N)_{inter-molecolar}$$

The composition of several potential terms with their peculiar constants associated with a chosen set of atomic kinds is called Force field (FF). Using different force fields for various types of molecular systems is recommended because different systems may exhibit distinct effects

governing their chemical interactions. In protein simulations, for example, it is mandatory to include a term for hydrogen bond interactions in the FF. Furthermore, in very large systems it can be advantageous to describe a given amount of atoms as a single entity and reduce the computational cost.

3.5.1 Simulation Analyses

Root Mean Square Deviation

The Root Mean Square Deviation (RMSD) represents a fundamental and extensively utilized metric within the realms of structural biology and computational chemistry. It plays a pivotal role in evaluating the likeness or variance in structure between two sets of atomic coordinates, such as those derived from protein structures obtained through molecular simulations, NMR experiments, or X-ray crystallography. RMSD quantifies the average spatial shift of atoms between these two structures, thereby offering valuable insights into the dynamic nature, conformational changes, and stability of biomolecules. The calculation of RMSD entails the alignment of two structures, often using a reference frame like the backbone atoms of a protein, followed by the computation of the root mean square of the squared distances between corresponding atoms in the aligned structures. Lower RMSD values indicate closer structural resemblance, indicating minimal structural deviations. Conversely, higher RMSD values point to more substantial structural disparities or flexibility. Furthermore, RMSD contributes significantly to the characterization of the dynamics of biological macromolecules, providing valuable insights on their functioning. Researchers use RMSD to identify crucial conformational changes in proteins or nucleic acids, especially during processes such as ligand binding

or enzyme catalysis. In addition, it plays a fundamental role in model validation by assessing the trustworthiness of computational simulations and the precision of structural models. Given its adaptability and importance, RMSD remains an essential tool in the exploration of biomolecular structures and their dynamic behavior, facilitating scientists in achieving a deeper comprehension of intricate biological systems. In this thesis work, the Root Mean Square Deviation (RMSD) was computed in relation to the minimized structure of the system under study. This analysis was carried out utilizing the GROMACS package.

Root Mean Square Fluctuation

Root Mean Square Fluctuation (RMSF) is a dynamic property that characterizes the vibrational and thermal movements of atoms or residues within a biomolecule. It serves as a foundational tool in molecular dynamics simulations and structural biology. When RMSF values are computed for distinct sections of a biomolecule, they allow researchers to identify areas exhibiting differing degrees of rigidity or flexibility. Higher RMSF values signify increased flexibility, indicating a greater likelihood of undergoing conformational changes in those specific regions. This information holds fundamental importance for comprehending the dynamic behavior of proteins, nucleic acids, or other macromolecules within biological systems. It is possible to exploit RMSF data to identify functionally critical areas, including binding sites, active sites, or allosteric sites, where structural flexibility plays a pivotal role in biological function. Furthermore, RMSF analysis can prove instrumental in designing experiments or facilitating drug discovery initiatives that target specific areas of interest within biomolecules[16].

Calculation of the Enzyme Active Site Pocket Volume

In the investigation of enzyme-ligand interactions, the determination of the volume of the enzyme's active site pocket plays a critical role in evaluating the accessibility of substrates. For this purpose, the Epock software is a valuable tool, capable of quantifying the volumes of cavities within proteins. To utilize Epock, a molecular dynamics trajectory and a configuration file, which can be generated using the VMD program, are required[17]. This configuration file serves to define specific parameters relating to the cavities for which volume calculations are desired[18]. Notably, these parameters encompass the selection of residues that delineate the cavity, the creation of inclusion spheres that establish their boundaries, and the instructions to the program to calculate the volume within these defined limits.

References

1 F. J. Timmermans and C. Otto, *Review of Scientific Instruments*, 2015, **86**, 011501.

2 W. Zhou, R. Apkarian, Z. L. Wang and D. Joy, in *Scanning Microscopy for Nanotechnology: Techniques and Applications*, 2007, pp. 1–40.

3 K. S. Subramanian, G. J. Janavi, S. Marimuthu, M. Kannan, K. Raja, S. Haripriya, D. Jeya Sundara Sharmila and P. S. Moorthy, in *Textbook on Fundamentals and Applications of Nanotechnology*, 2018, pp. 91–90.

4 D. McMullan, in *Biological Low-Voltage Scanning Electron Microscopy*, 2008, pp. 1–25.

5 D. E. Newbury and N. W. M. Ritchie, *J Anal At Spectrom*, 2013, **28**, 973–988.

6 D. E. Newbury and N. W. M. Ritchie, *Scanning*, 2013, **35**, 141–168.

7 A. Wassilkowska and T. Woźniakiewicz, *Solid State Phenomena*, 2015, **231**, 139–144.

8 C. Schick, *Anal Bioanal Chem*, 2009, **395**, 1589–1611.

9 H. Gharanjig, K. Gharanjig, M. Hosseinnezhad and S. M. Jafari, in *Characterization of Nanoencapsulated Food Ingredients*, Elsevier Inc., 2020, pp. 295–346.

10 S. J. Gerberding and C. H. Byers, *J Chromatogr A*, 1998, **808**, 141–151.

11 M. Das and D. Dasgupta, *Prep Biochem Biotechnol*, 1998, **28**, 339–348.

12 J. Porath, *J Protein Chem*, 1997, **16**, 463–468.

13 F. E. Re, *Science (1979)*, 1983, **222**, 245–252.

14 Z. Wang and J. R. Jocelyn Paré, *Techniques and Instrumentation in Analytical Chemistry*, 1997, **18**, 61–91.

15 M. Picollo, M. Aceto and T. Vitorino, *Physical Sciences Reviews*, 2019, **4**, 1–14.

16 A. Cooper, *Proc Natl Acad Sci U S A*, 1976, **73**, 2740–2741.

17 W. Humphrey, A. Dalke and K. Schulten, *J Mol Graph*, 1996, **14**, 33–38.

18 B. Laurent, M. Chavent, T. Cragnolini, A. C. E. Dahl, S. Pasquali, P. Derreumaux, M. S. P. Sansom and M. Baaden, *Bioinformatics*, 2015, **31**, 1478–1480.

Chapter 4

What makes lipases so attractive?

Lipases typically demonstrate exceptional chemoselectivity, regioselectivity, and stereoselectivity in their catalytic actions. These enzymes are easily accessible in substantial quantities, as numerous varieties can be efficiently produced in high yields by microbial organisms, particularly fungi and bacteria. In addition, the availability of crystal structures for many lipases significantly aids in the development of rational engineering approaches. Lastly, lipases generally operate without the need for cofactors and tend to avoid catalyzing side reactions. These collective characteristics make lipases the predominant and extensively utilized group of biocatalysts in organic chemistry.

4.1 Candida rugosa lipase entrapped in alginate beads

Candida rugosa lipase (CRL) is one of the most used enzymes for biotransformations, but the use of the free form is not convenient, since it is deactivated when exposed to temperatures higher than 50 °C for a long time[1] and, above all, the enzyme is not recyclable and its separation from the final products requires many time-consuming steps. For these reasons, several methods have been reported to improve enzyme stability and recyclability: physical adsorption on solid supports[2–6], cross-linking[7–9], covalent binding[10–12] and encapsulation on a solid matrix[13–16].

In this research, *Candida rugosa* lipase was immobilized in six distinct formulations of calcium-alginate beads. We carefully considered several operating parameters, including the $CaCl_2$ concentration in gelation solution

and the duration of residence of the beads in the hardening solution, to assess their influence on several critical aspects:

- The loading efficiency of CRL within the beads.
- The performance of biocatalytic hydrolysis towards two substrates with different hydrophobicity, namely, *p*-nitrophenyl acetate (*p*-NPA) and *p*-nitrophenyl dodecanoate (*p*-NPD).
- The recyclability and thermostability of the immobilized biocatalyst, qualities of paramount importance for industrial applications.
- The internal structure of the resulting beads.

Ultimately, after rigorous evaluation, we selected the most optimal formulation for the kinetic resolution of the racemic (*R,S*)-1-phenylethyl acetate ester.

4.1.1 Materials

Alginic acid sodium salt from brown algae (low viscosity), lipase from *Candida rugosa* (CRL, type VII, > 1000 U/mg solid), *p*-nitrophenyl acetate (*p*-NPA), *p*-nitrophenyl dodecanoate (*p*-NPD), racemic (*R,S*)-1-phenylethanol and (*R*)-(+)-1-phenylethanol were purchased from Sigma Aldrich. Racemic (*R,S*)-1-phenylethyl acetate was obtained from Merck. Coomassie Brilliant Blue G-250 dye was supplied by Bio-Rad. Enzyme and substrate were used without further purification. All other chemicals used were of analytical grade.

4.1.2 Preparation of enzymatic calcium alginate beads

Enzyme, either in powdered form or dissolved in a buffer solution, was introduced into a 5% (w/v) alginate solution, which could be aqueous or in a buffer. The resulting mixture was thoroughly stirred to ensure complete

homogenization. Subsequently, a 2 mL portion of this mixture was withdrawn using a syringe equipped with a 23G needle (with an inner diameter of 600 μm). This 2 mL aliquot was then gently dropped from a height of approximately 10 cm into a calcium chloride solution, which was either 2% or 5%, and was constantly magnetically stirred at 50 rpm. This process produced approximately 120 beads, with a total weight between 1.4 and 1.8 grams. After the beads were formed, they were left immersed in the calcium chloride solution for a period ranging from 10 minutes to 1 hour. This extended contact duration served to improve their mechanical strength. Finally, the beads underwent a filtration step and were subsequently rinsed with distilled water to eliminate any excess calcium chloride solution.

4.1.3 Beads characterization

The shape and size of the beads were analyzed using ZeissAxio Imager M2 microscope with AXIOCAM 503 MONO1 camera connected to a computer. The distribution of bead diameters was evaluated by using the variance coefficient (CV), which indicates the deviation of each diameter (D_n) from the average value (D_m) and was determined as described in the following equation (eq. 1).

$$CV = \frac{1}{D_m}\sqrt{\frac{\sum_{n=1}^{n}(D_n - D_m)^2}{n-1}} \times 100 \qquad (1)$$

If the CV value is less than 5%, 20-30 microspheres are usually sufficient to determine the indicators of sphericity because the dimensions are uniform[17]. Sphericity factor (SF) and aspect ratio (AR) are indicators that describe the roundness of a particle. SF varies from zero, for a perfect sphere, to unity for an elongated particle. AR, on the other hand, varies from unity, for a sphere,

to infinity for an elongated particle[18]. These factors were calculated using the equations below (eqs. 2 and 3).

$$SF = \frac{d_{max} - d_{min}}{d_{max} + d_{min}} \quad (2)$$

$$AR = \frac{d_{max}}{d_{min}} \quad (3)$$

where d_{max} and d_{min} are the maximum and the minimum diameter of Feret, respectively. Subsequently, the volume of the beads was calculated using the formula for the volume of an ellipsoid according to the following equation (eq. 4).

$$V = {}^{4}/_{3}\,\pi \frac{d_{max}}{2} \times \left(\frac{d_{min}}{2}\right)^{2} \quad (4)$$

To calculate the volume of an ellipsoid having only two diameters, it is assumed that the third one is equal to the minimum diameter.

The surface morphology, the internal structure and the elemental composition of the beads were investigated by means of Zeiss GeminiSEM 500 equipped with a Peltier cooling-device MK3 Cool stage Carl Zeiss SUPRA and with an EDS OXFORD Aztec Energy with INCA X-ACT detector with a working distance of about 8 mm and high voltage of 10 KeV. Sample morphology analyses were performed on hydrate systems at about 0 °C in variable pressure mode, using a BSE detector (Signal A BSD4). The energy dispersive X-ray spectrometry technique was used to semi-quantitatively determine the elemental composition of an area of interest and was carried out on dried beads.

4.1.4 CRL-alginate beads

Encapsulation of *Candida rugosa* lipase within calcium alginate beads involved an optimization process to ensure the beads' shape and resistance to magnetic stirring. The six most successful bead formulations, which varied in terms of the concentration of the calcium chloride and the duration of the residence in the solution, are detailed in Table 1. Notably, in each of these formulations, the CRL concentration remained constant at 2 mg/ml.

Table 1: Composition of alginate bead formulations. Sodium alginate 5% wt, CRL 2 mg/ml.

Beads N°	1	2	3	4	5	6
$CaCl_2$ %, v/w	2	5	2	5	2	5
Residence time min.	10	10	30	30	60	60

4.1.5 Immobilized CRL activity assay

The hydrolytic activity of lipase was determined by spectrophotometric measurements, by using Shimadzu UV-160A instrument, following the hydrolysis reaction of *p*-nitrophenyl acetate (*p*-NPA); the procedure was adapted from the literature to this case of study[19]. Beads (1.4-1.8 g - 4 mg CRL) were placed in a reaction vessel containing 9 ml of distilled water; then, 1 ml of substrate stock solution in CH_3CN (100 mM) was added to the vessel to start the reaction. The reaction was carried out at room temperature under mild stirring and monitored at different times. Spectrophotometric measurements were performed at λ = 348 nm, which corresponds to the isosbestic point of the equilibrium between *p*-nitrophenol/*p*-nitrophenoxide (*p*-NP), with a molar extinction coefficient as 5400 $M^{-1}cm^{-1}$. Once the reaction

was completed, the beads were filtered under vacuum, washed, placed in a container with distilled water and stored at 4 °C.

4.1.6 Immobilization efficiency

Loading efficiency was determined by quantifying the CRL content in both bead preparation and washing solutions using the Bradford method[20]. A calibration curve was obtained by measuring the absorbance of solutions containing from 0 to 0.3 mg/ml, prepared from a stock solution with a CRL concentration of 2 mg/ml, at λ = 595 nm. The resulting calibration curve had a R^2 correlation coefficient of 0.99. A similar approach was used to assess the loss of enzyme from the beads over time. Furthermore, the activity of the solution employed for bead preparation was measured, and this value was subtracted from that of the free enzyme to determine the immobilized activity and, consequently, the immobilization yield (%)[21]:

$$Yield(\%) = \frac{immobilized\ activity}{starting\ activity} \times 100 \qquad (6)$$

We have taken as starting activity that of the free enzyme since the entrapment process is very fast. Moreover, the immobilization efficiency, that is the percentage of the immobilized activity that remains after the entrapment (observed activity), was calculated as[22]:

$$Efficiency(\%) = \frac{observed\ activity}{immobilized\ activity} \times 100 \qquad (7)$$

In the analysis of the preparation and washing solutions, it was determined that the CRL concentration was below the detection limit of the method (22 μg/ml). Additionally, to assess the effective amount of immobilized enzyme, the catalytic activity of the prepared solution was measured, resulting in an immobilization yield of approximately 94.4%, as calculated using equation 1.

The immobilization efficiency, determined using equation 2, was found to be 76%. These findings suggest that 18% of the immobilized enzyme activity was lost due to the entrapment procedure, possibly because the enzyme became inactivated or was inaccessible to the substrate.

Regarding the enzyme's stability over time, samples of the storage water were collected at various times over a one-month period and subjected to the Bradford assay. Notably, after 48 hours of storage in the aqueous solution, only the preparations involving Beads 1 and Beads 2 showed detectable enzyme losses, with concentrations at or above the sensitivity of the detection method. Importantly, the enzyme concentration in these preparations remained relatively constant over time, and this phenomenon was observed in Beads 1 and Beads 2, which had a shorter residence time in the calcium chloride solution (10 minutes).

4.1.7 Hydrolytic activity of CRL-alginate beads on *p*-NPA

Before assessing the hydrolytic activity of *Candida rugosa* lipase encapsulated in alginate beads, control experiments were conducted to ensure that the beads without the enzyme did not catalyze the hydrolysis of *p*-nitrophenyl acetate (*p*-NPA). Once this control was established, the activity tests were carried out using the CRL-containing beads in pure water rather than a buffer solution. This choice was made because the pH of the medium plays a crucial role in enzymatic reactions by influencing the ionization state of the enzyme and causing changes in the active site[23], it was important to avoid the presence of salts in the reaction vessel to prevent bead from swelling. Initial catalytic experiments involved all six types of bead formulations with *p*-NPA at a concentration of 10 mM. The resulting data,

presented in Figure 1, illustrates the conversion percentage of the substrate over time for these different bead formulations.

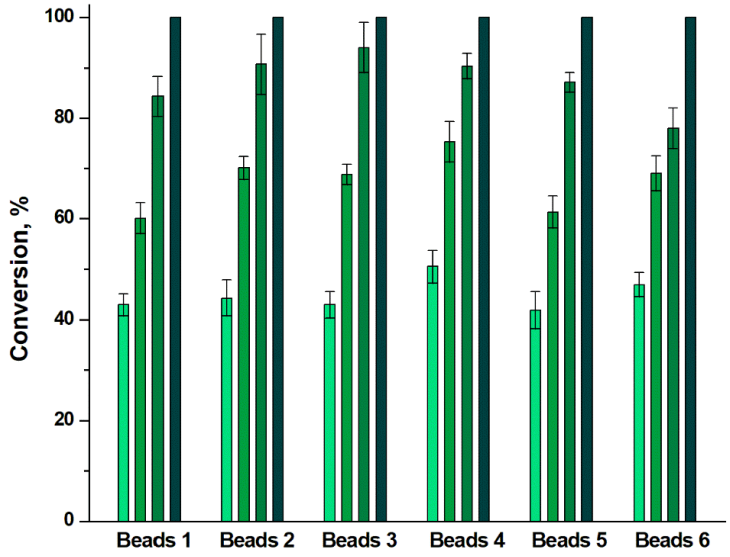

Figure 1: Substrate conversion percentages for all types of beads at 30 min (■), 1 h (■), 2 h (■) and 3 h (■); [p-NPA] = 10 mM, T = 25 °C.

The figure clearly illustrates that, regardless of the specific bead formulation used, all reactions reached completion within a three-hour time frame, exhibiting an initial reaction rate of approximately 130±10 μM/min. Minor variations were noted among the different types of beads during the reaction. As a result, it proved challenging to distinguish between them in terms of conversion efficiency, particularly when used immediately after their preparation. In the previous section, we established that no enzyme leakage occurred from the beads during extended storage, except in the case of Beads 1 and Beads 2, where enzyme loss remained at or below 1%. However, we lacked information on the enzyme activity after a prolonged period of storage in water. To address this issue, a reaction cycle was conducted one month after bead preparation to evaluate whether the

encapsulated enzyme remained active. Notably, for all types of beads, complete substrate conversion was achieved within four hours, indicating that there were no substantial alterations in the CRL activity even after one month of storage.

4.1.8 CRL-beads Reusability

One of the most valuable advantages of enzyme immobilization is its ability to be reused, a key factor in the production of biocatalysts. Consequently, a substantial body of literature addresses the stability and reusability of CRL when immobilized on solid supports through various methods, including adsorption[2,4,6], cross-linking[7], covalent binding[10–12], and entrapment[13,15,24,25]. While many of these studies have demonstrated significant improvements in enzyme stability and recyclability, it is important to note that protein deactivation can still occur. This deactivation often results from enzyme leakage from the support or limitations in its conformational flexibility. Additionally, limited substrate diffusion may also contribute to the loss of catalytic activity.

In this work we evaluated the stability of the encapsulated CRL and its potential for reuse employing the identical conditions as described in the preceding section. After each cycle, the biocatalyst was subjected to a filtration step, followed by multiple washes with water to eliminate any product adsorbed on the beads. Subsequently, the biocatalyst was reintroduced into a fresh reaction medium. The progress of the substrate hydrolysis reaction was monitored at specific time intervals until its complete conversion into the desired product. To examine the potential of our immobilization system, we selected the two extreme formulations, Beads 1 and Beads 6, and subjected them to ten consecutive catalytic cycles. This

investigation aimed to assess the impact of both the $CaCl_2$concentration and the residence time in the hardening solution. These tests were conducted using a 10 mM substrate concentration, and the reactions were monitored until completion. The results of these repeated uses, observed after 3 hours of reaction, which corresponds to the time required for the biocatalyst to complete its initial cycle, are presented in Figure 2.

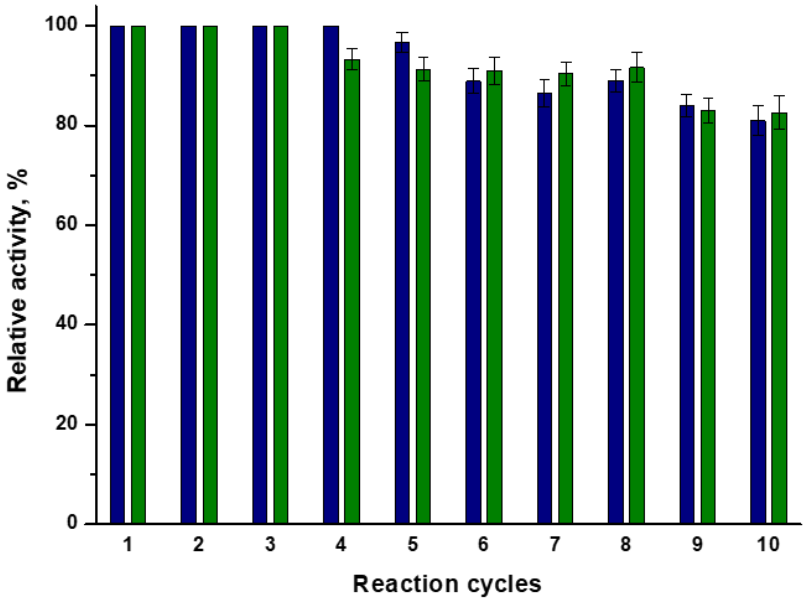

Figure 2: Residual activity of immobilized CRL in Ca-alginate beads in water after 3 h of reaction: Beads 1 (■) and Beads 6 (■); [pNPA] = 10 mM, T = 25 °C.

The data collected provides clear evidence that Beads 1 and Beads 6 effectively converted all substrate to product during the first four and three cycles, respectively. At the tenth cycle, both formulations exhibited a loss of activity of less than 20%. Despite this slight reduction in relative activity, the reaction time increased from 3 hours in the first cycle to 7 hours in the tenth cycle to achieve complete substrate hydrolysis. This prolonged reaction time can be attributed to a halving of the initial reaction rate for both formulations, decreasing from approximately 120 µM/min to 60 µM/min. The results

obtained so far suggest that there are no discernible differences in terms of catalytic efficiency and recyclability among the various formulations. When considering the use of alginate beads to immobilize CRL using our method, numerous advantages become apparent, as illustrated in Table 2. The preparation of the support is a simple process involving only two steps, resulting in high immobilization efficiency, recyclability, and storage stability. Furthermore, our biocatalyst remains active in distilled water, eliminating the need for a buffer solution, which may be responsible for the observed enzyme leakage and bead swelling[24,26].

Table 2: Comparison of our immobilization system with those of the literature in terms of preparation, yield of immobilization, recycling, and storage.

Immobilization Method	Preparation step	biocatalyst	Immobilization yield	substrate	Recycle times	Residual activity	Operational condition	Storage stability (days)	Residual activity	Ref.
Covalent immobilization onto a solid carrier (MOF)	2	*Candida rugosa* lipase (CRL) type VII	CRL-ZIF-8 8.18% mCRL-ZIF-8 9.45%	*p*-nitrophenyl palmitate	7	CRL-ZIF-8 45.8% mCRL-ZIF-8 52.3%	Isopropanol-PBS pH 7,5 (1:9) 35 °C	7	CRL-ZIF-8 34.42% mCRL-ZIF-8 42.18%	[9]
Covalent immobilization onto a ternary support (CRL-ALG/NC/MMT)	5	*Candida rugosa* lipase (CRL) Type VII	2.9%	Levulinic acid	9	47.5%	Ethanol 50 °C	-	-	[11]
Covalent immobilization on magnetic beads	5	*Candida rugosa* lipase (CRL)	-	racemic ibuprofen	5	100%	Cyclohexane 37 °C	-	-	[12]
Sol-gel encapsulation in presence of magnetic sporopollenin/Fe_3O_4 nanoparticles	4	*Candida rugosa* lipase (CRL)	Fe-A-Spo-E 36% Fe-EP-Spo-E 89%	*p*-nitrophenyl palmitate	7	Fe-A-Spo-E 21% Fe-EP-Spo-E 63%	Isopropanol – PBS pH 7 37 °C	50	Fe-A-Spo-E 45% Fe-EP-Spo-E 40%	[13]
Sol-gel encapsulation e with Fe_3O_4 or Fe_3O_4-Spo	5	*Candida rugosa* lipase (CRL) type VII	Fe_3O_4 78,6% Fe_3O_4-Spo 76,2%	racemic naproxen methyl ester	5	Fe_3O_4-E 36% Fe3O4-Spo 64%	aqueous phase–organic solvent (PBS pH 7 – isooctane)	42	Fe_3O_4 >70% Fe_3O_4-Spo >90%	[14]
Sol-gel encapsulation with b-cyclodextrin grafted magnetic nanoparticles (CD-APS-NP)	5	*Candida rugosa* lipase (CRL) type VII	2.2%	*p*-nitrophenyl palmitate	6	~ 50%	PBS buffer (pH 7.0) 35 °C	-	-	[15]
sol–gel Encapsulation in the presence of magnetic calix[4]arene nanoparticles	4	*Candida rugosa* lipase (CRL)	3.2%	racemic naproxen methyl ester	5	28%	aqueous phase–organic solvent (PBS – isooctane)	-	-	[16]
Covalent immobilization on magnetite coated with nanosilica	5	*Candida rugosa* lipase (CRL)	~ 80%	n-butyric acid and 1-butanol (1:2)	17	50%	n-heptane at 45 °C	-	-	[27]

Encapsulation in chitosan nanoparticles	3	*Candida rugosa* lipase (CRL)	-	Olive oil	7	53%	Water-oil (1:1) 37 °C	-	-	[28]
Entrapment in Ca-alginate beads	2	*Candida rugosa* lipase (CRL)	35%	*p*-nitrophenyl butyrate	3	72%	Tris–HCl buffer (pH 7.2); 30 °C	-	-	[24]
Covalent immobilization of lipase onto the silica nanoflowers-NH2	3	*Candida antarctica* lipase	~ 57%	levulinic acid and ethanol (1:10)	8	68%	tetra-butyl methyl ether 40 °C	-	-	[29]
Freeze dried calcium alginate beads	3	*Candida antarctica* lipase B (CALB)	-	*p*-nitrophenyl butyrate	6	~ 90%	Distilled water 35 °C	16	~ 100%	[30]
Immobilization on magnetic sol-gel hybrid organic-inorganic (Fe_3O_4 MNPs@TEOS-TSD@ CALB)	4	*Candida antarctica* lipase B (CALB)	90%	waste cooking oil	10	16.5%	Methanol; 40 °C	-	-	[31]
Covalent immobilization on polydopamine functionalized magnetic mesoporous biochar (MPCB-DA)	6	*Bacillus licheniformis* lipase	46.5%	*p*-nitrophenyl palmitate	10	56%	Tris-HCl (50 mM, pH 8.5); 40 °C	70	88% at 25 °C	[32]
Covalent immobilization on hydroxyapatite/glycyrrhizin/lithium-based metal–organic framework (HA/GL/Li-MOF) nanocomposites	5	*Thermomyces lanuginosus* lipase (TLL)	TLL@HA/GL/Li-MOF 71% TLL@Li-MOF 68%	*p*-nitrophenyl palmitate	10	TLL@HA/GL/Li-MOF ~ 55% TLL@Li-MOF ~ 45%	carbonate bufer (100 mM, pH 9.0); 60 °C	30	TLL@HA/GL/Li-MOF ~ 30% TLL@Li-MOF ~ 20%	[33]
Entrapment inside Ca-Alginate beads	2	*Candida rugosa* lipase (CRL) type VII	94.4%	*p*-nitrophenyl acetate	10	>80%	Distilled water 25 °C	30	~ 100%	Current work

4.1.9 Morphological Characterization

The morphological analysis was conducted to investigate the macro- and microstructure of beads produced with varying concentrations of calcium chloride and residence times in the hardening solution. In this study, Beads 1 and Beads 6 (enzyme-free) were specifically selected for examination. Initially, analyses were carried out using a stereomicroscope, and the corresponding results can be seen in Figure 3.

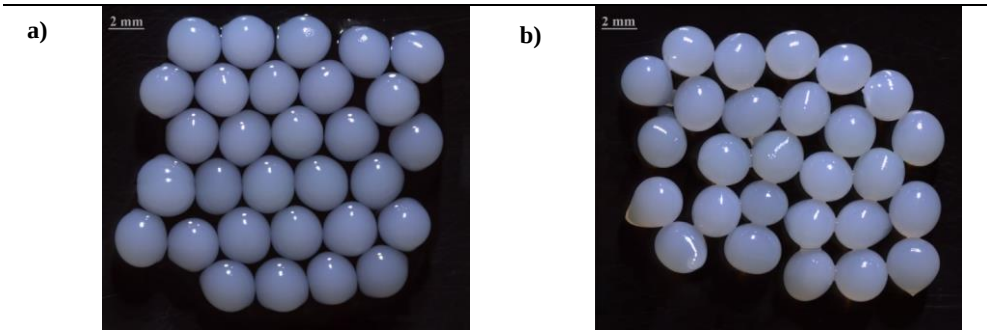

Figure 3: Stereomicroscope images at 1x magnification of Beads 1 (a) and Beads 6 (b).

Beads 1 and Beads 6 both displayed uniform dimensions, and a size distribution of 25 beads was measured. The variance coefficient (CV) values, determined using equation 1, were 0.9% and 3.7% respectively. Some dimensionless shape indicators, quantified using equations 2 and 3 in Section 4.1.2, are reported in Table 3.

Table 3: Average diameters of Beads 1 and Beads 6 and their sphericity indicators.

	BEADS 1	BEADS 6
Average diameter (D_m)	3.2 mm	3.4 mm
Sphericity factor (SF)	0.031	0.069
Aspect ratio (AR)	1.06	1.15

Both bead formulations have similar dimensions of approximately 3 mm. However, Beads 1 exhibited a better spherical shape compared to Beads 6. Beads 1 were prepared with a lower concentration of calcium chloride and a shorter hardening time, resulting in a spherical factor (SF) of less than 0.05 and a slightly higher aspect ratio (AR) than unity[18]. On the other hand, Beads 6, as observed from the stereomicroscope image, were less spherical. Their SF value was very similar to that of alginate particles reported in the literature, which were prepared using the same alginate and $CaCl_2$ concentration, and hardening time[34]. To analyze the morphology of the beads, scanning electron microscopy (SEM) was performed on both the external surface and the internal structure by cutting them with a scalpel. It is worth noting that morphological SEM studies in the literature are often conducted on dehydrated beads, which may not accurately reflect the real systems used in catalytic tests since they are usually hydrated. To overcome this limitation, variable-pressure equipment (VP-SEM) and a Peltier cooling device were utilized to investigate wet and hydrated samples in the SEM[35]. This methodology allowed us to examine the samples in their operating conditions. The SEM images were acquired at different magnifications, with Figure 4 showing the most significant images at 70x and 300x.

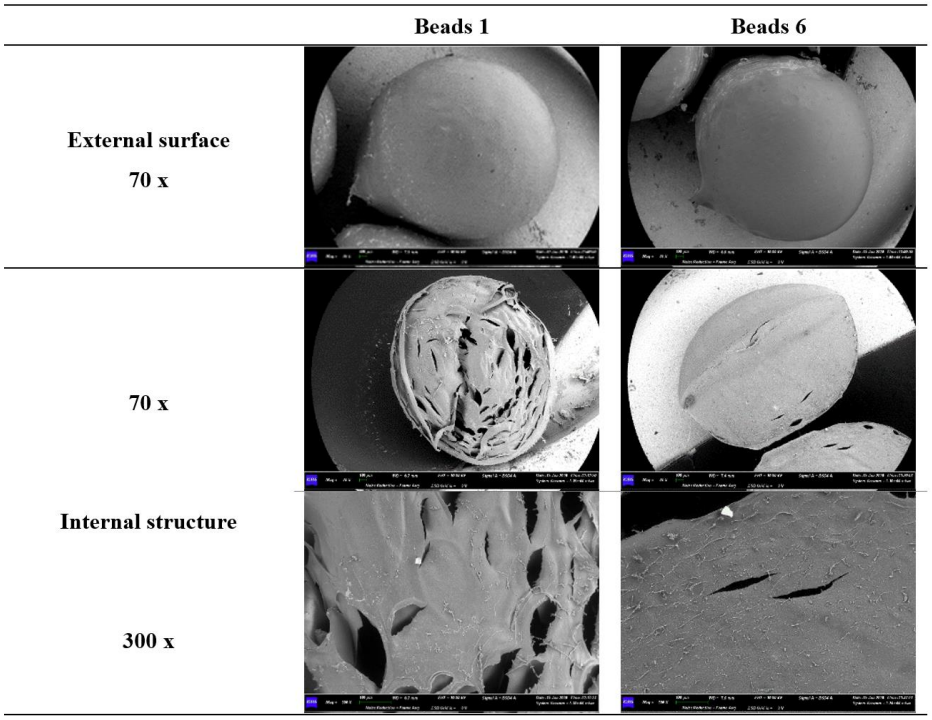

Figure 4: SEM images at 70x magnification of the external structure and at 70x and 300x magnifications of the internal structure of Beads 1 and Beads 6.

Although no significant differences were found in the external surface of both Beads 1 and Beads 6, the cross-sectional analysis revealed that Beads 1 had a lower internal compactness than Beads 6, which were denser and more homogeneous. To investigate the reasons for this difference in internal morphology, further SEM analyses were conducted, and Beads 2 ($CaCl_2$ 5%, 10 min) and Beads 5 ($CaCl_2$ 2%, 60 min) were chosen. SEM images of both the entire beads and their internal structure, shown in Figure 5, demonstrated that the internal compactness is influenced by the hardening time rather than the concentration of $CaCl_2$.

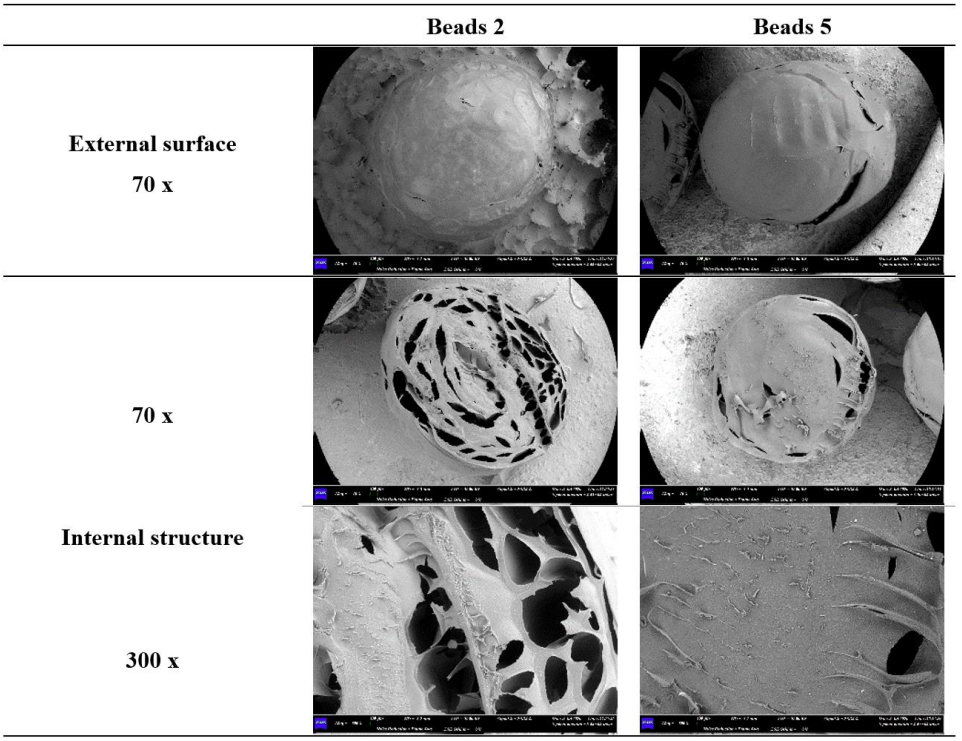

Figure 5: SEM images at 70x magnification of the external structure and at 70x and 300x magnifications of the internal structure of Beads 2 and Beads 5.

4.1.10 Reaction with a more hydrophobic substrate

p-Nitrophenyl dodecanoate (*p*-NPD) was selected to assess the effectiveness of CRL immobilized on Beads 1 and 6 with a more hydrophobic substrate. Due to its poor solubility in water, the hydrolysis reaction of *p*-NPD was conducted in tert-butyl alcohol, a sterically hindered alcohol, to minimize the competitive transesterification reaction rate. The conversion efficiency of the two formulations differed significantly. Beads 1 completely hydrolyzed the substrate within 6 hours, while Beads 6 had a very slow reaction rate, with only slightly over 40% product formed after 6 hours and a gradual increase over time. The reaction was not complete even after 24 hours, with a conversion of 80%. This outcome indicated that the internal structure of

Beads 6 limited the mass transfer of reagents and/or products in the reaction medium, particularly with larger, natural-like hydrophobic substrates. Conversely, Beads 1, with their less compactness, allowed the free diffusion of reagents within their porous structure. Additionally, the time taken for Beads 1 to completely hydrolyze *p*-NPD was double that required for the reaction with *p*-NPA. To determine if the longer reaction time was due to the substrate or the solvent, the reaction of *p*-NPA in *tert*-butyl alcohol was conducted for comparison. After 48 hours, only 58% conversion was achieved, which could be attributed to the dehydration of the beads, causing them to shrink over time. The decrease in the reaction rate was a result of water loss from the confined environment in which the enzyme was located. This hypothesis was supported by experiments varying the amount of water in the reaction medium, where the time for complete hydrolysis of *p*-NPA decreased from 24 to 4 hours with water percentages of 5% and 75%, respectively. Considering all the aforementioned factors, the Beads 1 formulation, which exhibited faster reaction rates and better mass transfer capabilities, was chosen for thermostability tests and kinetic resolution of (*R,S*)-1-phenylethyl acetate.

4.1.11 Thermostability

We investigated the thermal stability of both free and immobilized CRL. Each form of the enzyme was subjected to incubation in distilled water at temperatures of 25 °C and 50 °C for different times, ranging from 8 hours to one week. To evaluate their stability, the hydrolysis reaction of *p*-NPA was carried out at the respective incubation temperatures for a 30-minute duration in pure water. This allowed us to measure both the initial and the residual enzymatic activity. One of the advantages of enzyme immobilization

is the improvement of thermal stability. Therefore, the stability of both free and immobilized lipase in Beads 1 was determined by incubating them for different times and the residual activity was measured at 25.0±0.1 and 50.0±0.1 °C (Figure 6).

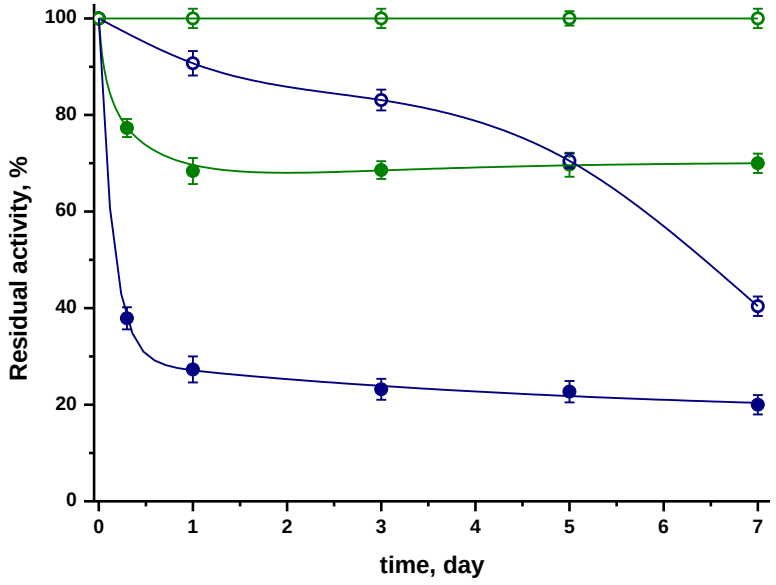

Figure 6: Thermal stability of free (●/○) and immobilized lipase (●/○) at 25 °C (empty symbols) and 50 °C (closed symbols).

The figure clearly demonstrates the effect of immobilization on the stability of Ca-alginate beads for CRL. At 25 °C, the activity of immobilized CRL did not decrease even after 7 days of incubation, while the free form suffered a 30% loss of activity after 5 days and 60% after one week. The stabilization effect was even more pronounced at 50 °C, where the residual free lipase activity dropped below 40% after only 8 hours and continued to decrease to about 20% after one week. In contrast, the immobilized CRL maintained approximately 70% of its initial activity after 1 day of heat treatment and remained constant throughout the week. To further assess the effect of

different bead formulations on enzyme thermal stability, tests were conducted with Beads 6 at 50 °C. These tests showed that the higher compactness of the beads did not affect the stability of the enzyme, as the loss of activity after 24 hours was recorded at 66%.

Although the data in Figure 6 presents the trends of residual activity over time, it does not consider the differences in reaction rate before incubation. Specifically, the hydrolysis rate with free CRL was 30% higher than that of the immobilized CRL at both 25 °C (183 vs. 132 μM/min) and 50 °C (520 vs. 370 μM/min). This could be attributed to a slower diffusion of the substrate within the support. However, after one week of incubation, the reaction rate of Beads 1 at both temperatures was twice as high as that of the free enzyme, indicating an improvement in enzyme stabilization through entrapment.

4.1.12 Kinetic resolution of racemic 1-phenylethyl acetate

Numerous studies have been dedicated to the kinetic resolution of racemic substrates with pharmacological significance, such as naproxen[7,14,36] and ibuprofen[12], using immobilized *Candida rugosa* lipase. This interest arises from the fact that the enantiomers of these non-steroidal anti-inflammatory drugs exhibit distinct therapeutic activities.

The hydrolysis reaction of (*R,S*)-1-phenylethyl acetate was conducted as previously described. At various time intervals, the beads were separated via vacuum filtration, and the aqueous phase was extracted using ethyl ether. After solvent removal, isopropanol was added to the flask. To determine the conversion and enantiomeric excess values (ee %) for both the reactants and products, we employed HPLC analysis with an Agilent - 1220 Infinity II instrument, equipped with a chiral column (Lux Cellulose-1). The eluent used was a 99:1 mixture of hexane and isopropanol, with a flow rate of 0.6 ml/min.

The retention times for key compounds were as follows: 3.6 min for (*R*)-1-phenylethyl acetate, 3.9 min for (*S*)-1-phenylethyl acetate, 14.7 min for (*R*)-1-phenylethanol, and 18.5 min for (*S*)-1-phenylethanol. We calculated the enantiomeric excess of the substrate (ee_s) and product (ee_p), as well as conversion (c) and enantioselectivity (E), with the latter determined using the actual values of c and ee. These calculations were performed using the following equations:

$$ee_s(\%) = \frac{|R-S|}{|R+S|} \times 100 \quad (8)$$

$$ee_p(\%) = \frac{|R-S|}{|R+S|} \times 100 \quad (9)$$

$$c\ (\%) = \frac{ee_s}{ee_s + ee_p} \times 100 \quad (10)$$

$$E = \frac{\ln[(1-c)(1-ee_s)]}{\ln[(1-c)(1+ee_s)]} \quad (11)$$

where R was values of peak areas for (*R*)-1-phenylethanol and its ester, whereas S was values of peak areas for (*S*)-1-phenylethanol and its ester.

Given the remarkable recyclability and thermal stability of Beads 1, which make them potential candidates for industrial applications, we carried out preliminary tests using these beads for the resolution of (*R*)-1-phenylethanol in an aqueous solution, starting from racemic 1-phenylethyl acetate as a model substrate. While the literature contains reports on the stereoselective kinetic resolution of racemic 1-phenylethyl acetate catalyzed by other lipases[37–41], which achieved very high enantiomeric excess toward the (*R*)-enantiomer, the yields were not entirely satisfactory. More recently, the marine microbial GDSL lipase MT6 displayed opposite stereoselectivity by generating (*S*)-1-phenylethanol instead of (*R*)-1-phenylethanol during the

hydrolysis of racemic 1-phenylethyl acetate[42]. In our experiments, we observed that, as the conversion increased, the enantiomeric excess of the product (ee_p) decreased. At the optimal reaction time of 12 hours, a conversion of 28.5% was achieved, with an enantiomeric excess value of the substrate (ee_s) above 97%. In contrast, CRL solubilized in phosphate buffer at pH 7.2 exhibited no enantiopreference for the (*R*)-acetate, with an enantiomeric excess value (ee_p) of only 44% and an enantioselectivity factor of 4[43]. The percentage of enantiomeric excess (ee_s and ee_p), conversion (c), as well as enantioselectivity (E), calculated using equations 3-6, are presented in Table 4.

Table 4: Enantiomeric excess of both substrate (ee_s) and product (ee_p), conversion (c) and enantioselectivity (E) of the hydrolysis reaction of (R,S)-1-phenylethyl acetate using Beads 1 at 25 °C.

Reaction time (h)	ee_s, %	ee_p, %	c, %	E
8	3.5	61.5	5.3	4.3
24	17.6	62.8	21.9	5.2
32	18.1	61.9	22.6	5.1
48	23.1	64.5	26.4	5.8
72	49.5	61.7	44.5	6.8
96	83.3	60.9	57.8	10.3

As evident from the findings, the enantiomeric excess of the product (ee_s) exhibited a steady increase with prolonged reaction time and higher conversion rates, while the enantiomeric excess of the substrate (ee_p) remained relatively constant. After 96 hours of reaction, the highest values of enantioselectivity (E = 10.3), conversion (c = 57.8%), and enantiomeric excess of the substrate (ee_s = 83.3%) were attained. These values, although slightly higher, do not significantly deviate from those documented in the

literature concerning free lipase in a phosphate buffer, which demonstrated an ee_s value of 44% and an enantioselectivity factor of 4[43]. It is noteworthy that the inherent chirality of the matrix played a role in these results. These tests were undertaken to evaluate whether immobilization enhanced the enantioselectivity of the enzyme towards the chosen substrate. In this case, no improvement in enantioselectivity was observed. However, the entrapment of CRL improved its stability under non-physiological conditions and at elevated temperatures, making it reusable for multiple cycles. This recyclability is pivotal for industrial applications.

4.1.13 Conclusion

In this study, lipase from *Candida rugosa* was efficiently trapped within Ca-alginate beads prepared under various operating conditions. Morphological studies showed that, although the internal microstructure differed, all formulations exhibited high immobilization efficiency, good recyclability, and both operational and thermal stability. The effectiveness of the immobilized CRL was dependent on the substrate's hydrophobicity. The greater compactness of Beads 6 compared to Beads 1 did not affect the hydrolysis rate of *p*-NPA but limited the mass transfer of the more hydrophobic substrate *p*-NPD, resulting in a significant decrease in its reaction rate.

4.2 CALB: experimental and computational approach

Transformation in organic solvents or in a mixture of water and co-solvent is an emerging research area for the application of biocatalysis in the industrial field[44]. Firstly, because the use of pure water in reactions leads to challenges in purification due to its high boiling point and low vapor pressure, resulting in increased costs and time consumption[45]. Additionally, water as a reaction medium can induce unwanted side reactions like racemization, ester hydrolysis, polymerization, and decomposition, particularly limiting reactions involving enzyme synthesis[46]. If water is used as the reaction medium, it must be considered that it can participate in reactions as an acid/base catalyst or influence the stability of the transition state. Furthermore, water can be the reagent or product of the desired reaction, modifying its equilibrium[47]. By removing the constraints imposed by water as a reaction medium, many potential products or reactants that are insoluble or labile in water can be used in biotransformation[48]. In non-aqueous conditions, enzymatic stability depends on the nature of the enzymes, whether they are free or immobilized[49], on the presence of additives[50], on the water content and on the type of non-aqueous solvent[51]. The presence of organic solvents can lead to irreversible inactivation of the enzymes due to unfolding[52]; furthermore, given the hydrophilic nature of many enzymes, they will tend to aggregate in non-aqueous media causing their mutual deactivation[53]. For these reasons, heterogeneous phase biocatalysts based on lyophilized enzyme powders, cross-linked crystals and enzymes immobilized on inert supports are often used. Among the latter, Novozym435 (N435) is of particular interest. It is a commercially available lipase, produced by Novozymes, based on the immobilization by interfacial activation of the lipase B from *Candida antarctica* (CalB) on the microporous resin Lewatit VP

OC 1600, composed of polymethyl methacrylate cross-linked with divinylbenzene. Although this biocatalyst presents some serious problems, such as its release from the support and the mechanical fragility of the support under stirring[54], it is one of the most widely used commercial biocatalysts in both industry and academia.

In this study, we investigated the impact of various organic solvents on the activity of *Candida antarctica* lipase type B. The hydrolysis reactions were conducted using mixtures containing 30% organic solvent. After identifying the most influential solvents (*t*-butanol and acetonitrile), we further evaluated the effect of varying solvent concentrations on CalB activity. Subsequently, molecular dynamics simulations were performed to analyze the behavior of CalB within these selected solvent mixtures. Specifically, we examined alterations in the structural and dynamic characteristics of the enzyme's active site, as well as the behavior of solvent molecules present within the enzyme's cavity. These analyses aimed to provide insights into the observed kinetic data.

4.2.1 Materials

Novozym 435 (the commercially immobilized form of *Candida antarctica* lipase B), *p*-nitrophenyl acetate (*p*-NPA) were purchased from Merck. All the organic solvents were of analytical grade (RPE) and supplied by Merck, Carlo Erba Reagents and Sigma-Aldrich.

4.2.2 Hydrolytic activity assay of *Candida antarctica* lipase type B

The catalytic activity was monitored spectrophotometrically with the Hewlett Packard HP 8452A instrument, following the hydrolysis reaction of *p*-NPA at 348 nm, which corresponds to the isosbestic point *p*-nitrophenol/*p*-nitrophenoxide. The procedure was adapted from the

literature to this case study[55]: a test tube containing the reaction solution (water/organic solvent mixture at different percentages) was thermostated at a temperature of 37° C. The enzyme at a concentration of 0.5 mg/ml is added to the reaction solution after 15 minutes so that it has reached thermal equilibrium. To start the hydrolysis reaction, the substrate solubilized in the same organic solvent present in the reaction mixture is added to reach a final concentration of 10 mM. To monitor the evolution of the reaction and determine the reaction rate, 20 µl of the reaction mixture, at specific time intervals, were placed in a 1 ml cuvette in order to carry out the spectrophotometric analyzes. Following the same procedure, the kinetic parameters of the enzyme were performed in 5% and 30% acetonitrile and 30% *t*-butanol. It is important to specify that 5% v/v acetonitrile is the minimum amount required to solubilize the substrate; therefore, under this condition the medium will be considered exclusively aqueous.

Kinetic parameters k_{cat} and K_M in water and in the presence of 30% organic solvents were obtained from the linear regression analysis of the double reciprocal Lineweaver-Burk plots with *p*-NPA concentration varied by 0.5 units from 1 to 3 mM and the initial rate was evaluated by carrying out several samplings in the early stages of the reaction. The regression coefficient was always above 0.99. All sets of experiments were reproduced at least three times, and the differences between duplicates in each experiment were always below 5%.

4.2.3 Effect of the solvent and its percentage on the CalB activity in water/organic mixture

The effect of some water-miscible organic solvents (Table 5) on the hydrolytic activity of CalB towards the substrate *p*-NPA was studied following the procedure described above.

Table 5: Solvents used for the initial screening, with selected physicochemical properties.

Organic solvents	Abbreviations	log *P* [56]	μ_r [57]
Acetone	ACE	-0.24	20.56
Acetonitrile	MeCN	-0.34	35.94
Dimethyl sulfoxide	DMSO	-1.35	46.45
Ethylen glycol	EG	-1.37[58]	37.70
Isopropanol	*i*-PrOH	0.05	19.92
N,*N*-Dimethylformamide	DMF	-1.01	36.71
n-Propanol	*n*-PrOH	0.25	20.45
t-Butanol	*t*-BuOH	0.35	12.47

Specifically, for the screening some different solvents were chosen, both miscible with water and able to solubilize the substrate, and the results are reported in Figure 7.

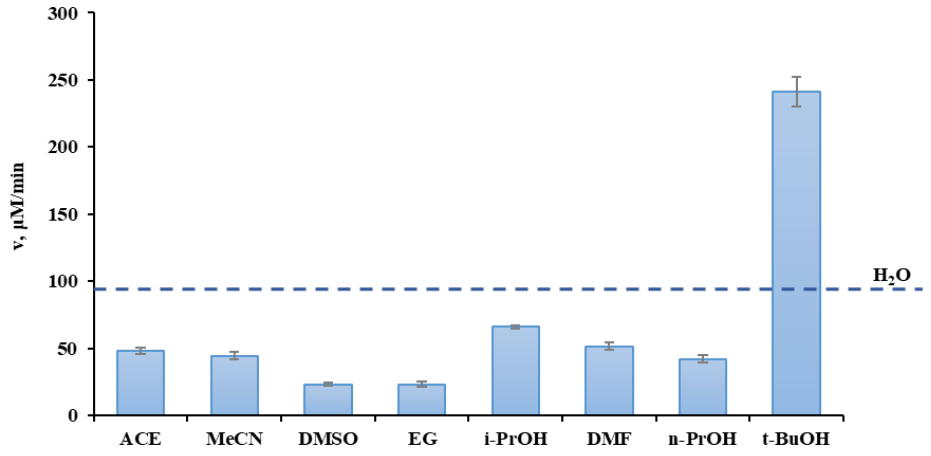

Figure 7: Hydrolysis reaction rate in 30% v/v organic solvent in water at 37°C.

As shown in the Figure, the hydrolytic activity of CalB depended on the organic solvent used in the experiment. The highest activity was obtained with 30% *t*-BuOH, whose reaction rate was approximately 240 µM/min. In all the other cases, the addition of 30% organic solvents reduced the enzyme activity, compared to pure water, and varied between 20 and 60 µM/min, regardless of their physicochemical properties. In particular, solvents with the smallest log P values, i.e., DMSO and EG, showed the lowest activity (23 µM/min), but there was no clear correlation between the solvent polarity parameters, as log *P* or dielectric constant, reported in Table 1, and reaction rate. In fact, solvent not only solubilizes the substrate, but could also establish specific interactions with the enzyme and its active site by inducing denaturation.

As for alcohols, no tests were performed with small alcohols such as methanol and ethanol. In fact, it is well known that methanol exerts a deactivation towards CalB, as it binds in the substrate access channel, with a consequent competitive inhibition[59,60]. The enzyme deactivation caused by ethanol and water-ethanol mixtures is instead due to the dissolution of the

polymethyl methacrylate, which constitutes the support of CalB, and to a change in the enzyme secondary structure, producing an increase in β-sheet structure and a decrease in the α-helix content[61]. Despite the solubility of the support was also found using other short-chain alcohols, *n*-propanol and *i*-propanol were herein used as this effect is less pronounced[62]. The hydrolysis reaction rate in the presence of 30% *i*-PrOH was 1.4-fold higher compared to *n*-PrOH (62 μM/min vs. 44 μM/min), indicating the slight difference in activity that occurs between linear and branched alcohols, already reported by Zieniuk and coworkers[63]. The higher hydrolytic activity when using nonlinear alcohols was even more evident with *t*-BuOH, as previously seen. Short-chain alcohols, including *t*-BuOH, were recently reported to induce biocatalyst inactivation[64]. This result is not consistent with the beneficial effects reported in the literature according to which the use of *t*-BuOH as solvent for biodiesel production overcame the negative effects caused by excessive methanol and the by-product glycerol[65–67].

After this preliminary screening, two solvents were selected, and their percentages were varied by increasing them to 50 and 75% v/v. The best co-solvent in the initial screening, *t*-butanol, and acetonitrile, able to easy solubilize the substrate and simple to parameterize for molecular dynamics studies, were chosen. The trends of the hydrolysis reaction rate of *p*-NPA as the percentage of solvent increases are shown in Figure 8.

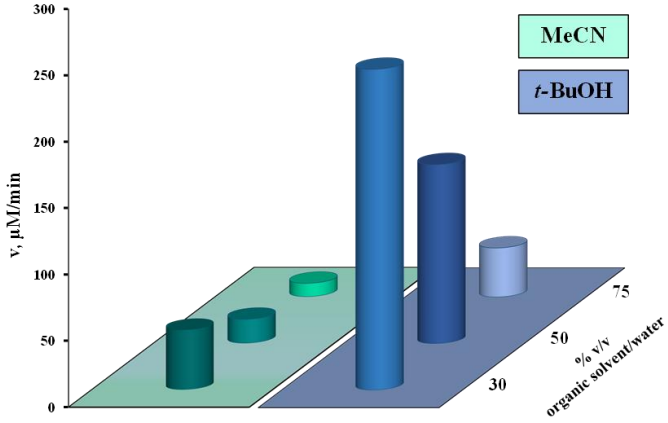

Figure 8: Hydrolysis reaction rate of p-NPA at different percentages of MeCN and t-BuOH added at 37 °C.

For both solvents, the increase in their percentage resulted in a reduction in hydrolysis rate. In both cases, the reaction rate decreased by about 50% and 80% when the percentage of organic solvents in the mixture was increased from 30 to 50% and 75% respectively. It is important to underline that, despite the significant loss of activity, the hydrolysis rate in the presence of 75% *t*-BuOH is slightly lower than that found in 30% MeCN. Then, considering these results and those of the previous screening, it can be asserted that *t*-BuOH is the best co-solvent among the investigated ones.

4.2.4 Determination of kinetic parameters

To gain more insight into how different reaction conditions may affect the enzyme reaction rate kinetic parameters of CalB were determined. All data points obeyed Michaelis-Menten kinetics and could be correlated in the Lineweaver-Burk plot for an estimation of the kinetic parameters, reported in Table 6.

Table 6: Effect of organic solvents on CalB kinetic parameters at 37 °C.

% v/v organic solvent/water	K_M, mM	$10^2 k_{cat}$, s^{-1}
-	9.7	9.3
30% MeCN	3.5	3.7
30% *t*-BuOH	32.4	85.5

The K_M value characterizes the affinity between the substrate and the enzyme. A low K_M value means high affinity between enzyme and substrate and greater difficulty in the dissociation of the ES complex. K_M value depended on the characteristics of the reaction mixture catalyzed by the enzyme and the reaction conditions. In fact, as can be seen from the data in the table, two opposite effects were found when the two solvents were added in water. In particular, the addition of MeCN resulted in an improvement of the enzyme-substrate affinity (the K_M value was 3 times lower than in pure water), but at the same time a 2.5-fold decrease in the catalytic constant was also detected. On the other hand, a lower enzyme-substrate affinity was found in the presence of *t*-BuOH, together with a high increase in the catalytic constant (more than 9-fold).

Possible explanations for the different K_M and k_{cat} values observed in the different solvents are addressed by means of computational methods which are described in the following paragraph.

4.2.5 Computational modelling

To rationalize at a molecular level the differences in the catalytic activity of the CalB enzyme in different solvents we carried out Molecular Dynamics (MD) simulations. The starting configuration of CalB was taken from the structure present in the 1TCA.pdb file. All graphical representations of the

computational part were made with VMD software. The set-up of the system was analogous to that employed in previous work[68] and is discussed in detail in the Chapter 3 paragraph 3.5. It should be noted that in our simulations the enzyme is fully solvated, while in the experiments it is anchored to an inert support. Hence, possible effects due to the presence of the resin are not taken into consideration. To analyze the behavior of the active site of the enzyme in the two solvent mixtures we firstly examined the distance between the two helices forming the protein lid, *i.e.*, helix α5 and α10. In Figure 9 the distribution of the distance between the centers of mass of the two helices in the two solvents is reported. Two representative configurations are also reported in the top panel of the figure. From the comparison it is evident that the active site is more accessible in the presence of *t*-BuOH than in the mixture with the more polar solvent MeCN. The analysis of the volume of the active-site cavity in the two solvents shows that also the cavity itself is larger in the presence of *t*-BuOH (data not shown). The presence of a wider cavity in *t*-BuOH might not be so crucial in hosting small substrates, as the *p*-NPA used in the present experiments but might be more relevant in the case of larger substrates.

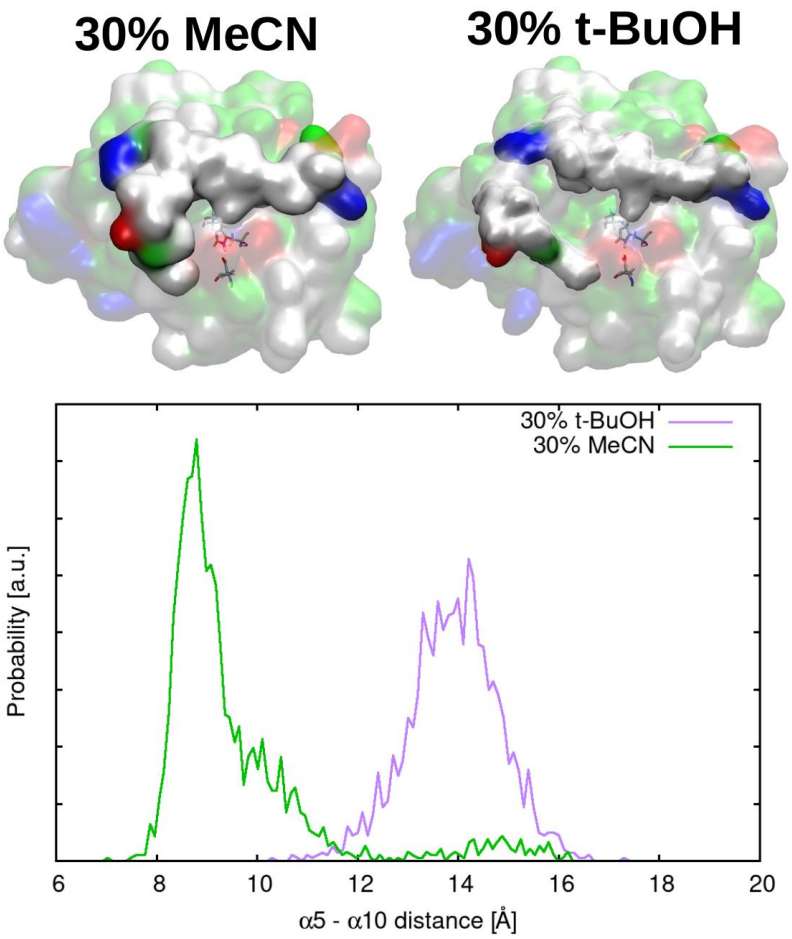

Figure 9: Analysis of the accessibility of the active-site cavity. In the top panel representative configurations of open and closed states of the protein lid are reported. The catalytic triad is highlighted in a stick representation. In the bottom panel the distribution of the distance between the centers of mass of helix α5 and helix α10 along the simulation in30%t-BuOH (purple) and 30% MeCN (green) is reported.

To gain a deeper insight into the accessibility of specific regions of the active-site cavity to the substrate, we analyzed the solvent occupancy in the oxyanion hole, which is the site that hosts the carbonyl group of the substrate and has the role of stabilizing the negative charge localization on the oxygen at the transition state. While the organic solvent molecules cannot access the oxyanion hole because of steric hindrance, water molecules are found to

occupy the site, but with different probability in the two solvents. The analysis of the distribution of the minimum distance between the amide N atoms of residues Thr-40 and Gln-106 of the oxyanion hole and the oxygen atom of the closest water molecule, reported in Figure 10, top panel, for both mixtures, shows that while in *t*-BuOH a water molecule is always tightly bound to the oxyanion hole, instead a water molecule is found in only half of the configurations in MeCN. Given that binding of the substrate implies a close interaction of the carbonyl group of the substrate with the oxyanion hole, a lower occupancy of water in the oxyanion hole, as observed for the water-MeCN mixture, should favor substrate binding. This agrees with the different experimental affinity (i.e., K_M) values.

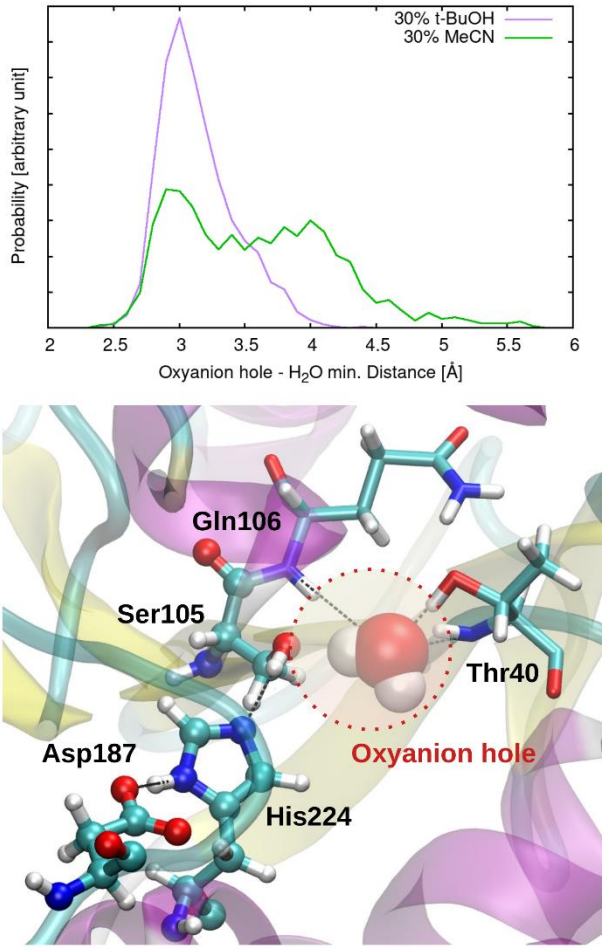

Figure 10: Water occupancy in the active-site cavity. In the top panel the distribution of the minimum distance between the amide N-atoms of the oxyanion hole and the oxygen of the closest water molecule is reported. A representative configuration of the oxyanion hole with a bound water molecule is reported.

We then analyzed the presence of organic solvent molecules in the active-site cavity. In both mixtures, two solvent molecules are found, on average, in the cavity. Nevertheless, the mean residence time of the organic solvent molecules in the pocket is different in the two mixtures, being 9.2 ± 1.2 ns in *t*-BuOH and 2.5 ± 1.1 ns in MeCN. The mean residence time was calculated as the average of all the residence times sampled along the full trajectory (see Figure 11). The lower residence time of MeCN molecules in the active

site is an additional factor contributing to the higher substrate affinity found experimentally.

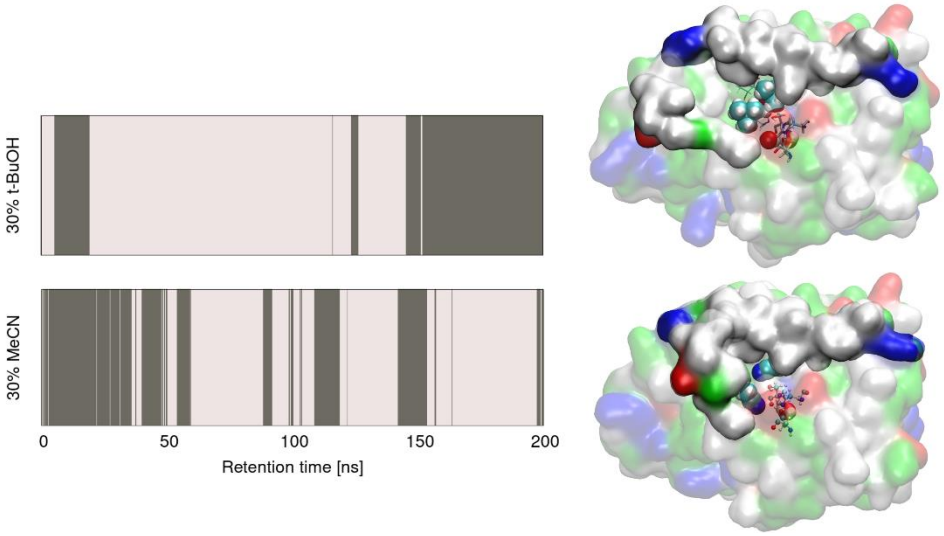

Figure 11: Organic solvent occupancy of the active-site cavity. In the left panel, the residence times of the organic solvent molecules used to calculate their mean residence time in the two water-organic solvent mixtures are reported. Each exchange between light and dark shades of grey indicates the exchange of the solvent molecule closest to the active site with another solvent molecule. The width of each band represents the residence time of the solvent molecule within the catalytic site. Note that the two colors are not associated with specific molecules but are meant to highlight the exchange between different molecules. In the right panels, representative configurations showing the occupancy of organic molecules in the active-site cavity in the two solvent mixtures are reported.

To gain insight into the difference in the catalytic rate constants k_{cat} found experimentally in the two solvent mixtures, we analyzed the stability of the catalytic triad over the two simulations. It was previously proposed based on short (few ns long) MD simulations of CalB in different solvents (water, CH_3Cl, *t*-BuOH, MeOH and others) that the polarity of the solvent affects the catalytic triad stability by inducing a change in the length of the Ser-105-His-224 hydrogen bond (HB) distance[69]. In our simulations, we provide a different explanation for the different catalytic-triad stability observed in the two

mixtures of different polarity. The HB distance of the Ser-105-His-224 couple (namely the O-N distance) was calculated along the two simulations and the corresponding distributions are reported in Figure 12, bottom panel. Three main peaks were found: a peak at 3.0 Å corresponding to a stable, "direct" HB between Ser-105 and His-224; a peak at ~4.0 Å corresponding to configurations with a "water-mediated" HB, through which a proton exchange between the two residues is possible via a Grotthus mechanism[70]; a peak at ~5.0 Å corresponding to configurations in which the HB is "broken". While in the water/*t*-BuOH solvent almost 90% of the structures possess "active" configurations of the triad (i.e., with either a "direct" or "water-mediated" HB), in the water/MeCN solvent the "water-mediated" HB is never observed and only ~60% of the structures show a "direct" HB.

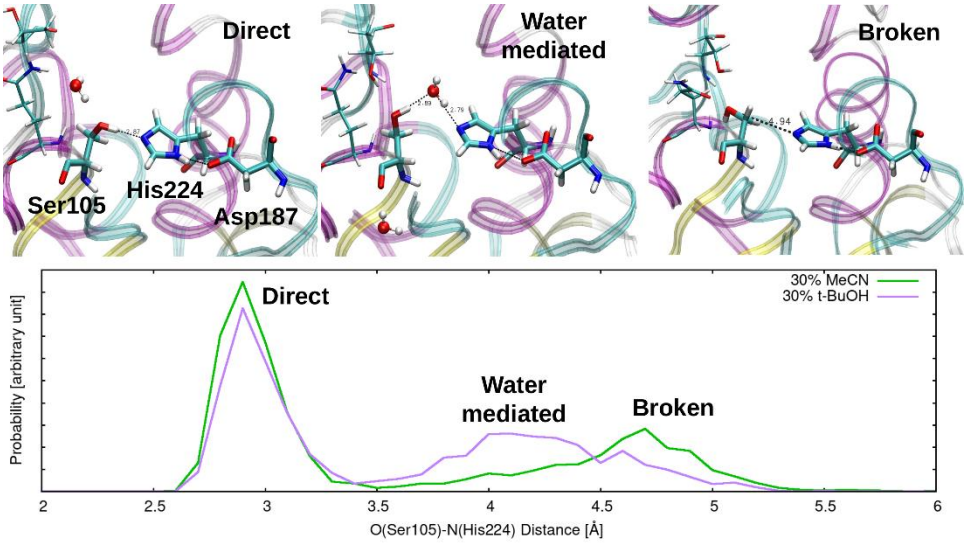

Figure 12: Stability of the catalytic triad. The top panel shows representative configurations of the most populated structures of the catalytic triad. The distribution of the O(Ser-105)–N(His-224) distance is reported in the bottom panel. The purple and green lines represent the simulations in 30%t-BuOH and 30% MeCN, respectively.

The results on the stability of the catalytic triad support the experimental evidence that the CalB catalytic activity is higher in the water/*t*-BuOH mixture than in the water/MeCN one. Additionally, the persistent presence of *t*-BuOH molecules, which are less polar than the MeCN ones, in the active-site cavity should increase the nucleophilicity of the catalytic serine, thus contributing to the higher k_{cat} observed experimentally.

4.2.6 Conclusion

In this research, we assessed the impact of water-organic solvent blends on the catalytic efficiency of *Candida antarctica* lipase B, employing both kinetic analyses and molecular dynamics simulations. Our aim was to discern how alterations in the active site structure, induced by organic solvents, influenced the enzyme's activation or inhibition. Acetonitrile and *t*-butanol, chosen for their contrasting effects on catalysis, were the focal solvents. Our investigation delved into several aspects, including the accessibility of the active site, the duration of solvent presence within the enzyme cavity, the water occupancy in the oxyanion hole, the stability of the catalytic triad, and the environmental polarity. This approach allowed us to gain detailed molecular-level information on the observed kinetic properties. Specifically, we found that notable variations in the mobility of organic solvent and the presence of water in the oxyanion hole had a significant impact on the accessibility of the active-site, thereby affecting enzyme-substrate affinity. Additionally, the stability of the catalytic triad and the existence of a less polar environment emerged as pivotal factors in determining the catalytic activity of *Candida antarctica* lipase B.

References

1 M. Matsumoto and K. Ohashi, *Biochem Eng J*, 2003, **14**, 75–77.

2 H. Aghaei, M. Ghavi, G. Hashemkhani and M. Keshavarz, *Int J Biol Macromol*, 2020, **162**, 74–83.

3 R. D. M. Ferreira, R. Brackmann, E. B. Pereira and R. D. C. da Rocha, *Appl Biochem Biotechnol*, 2020, **190**, 839–850.

4 L. Izrael-Zivkovic, L. Zivkovic, B. Jokic, A. Savic and I. Karadzic, *Journal of the Serbian Chemical Society*, 2015, **80**, 1113–1125.

5 L. T. Izrael Živković, L. S. Živković, V. P. Beškoski, K. R. Gopčević, B. M. Jokić, D. S. Radosavljević and I. M. Karadžić, *J Mol Catal B Enzym*, 2016, **133**, S533–S542.

6 L. T. Izrael Živković, L. S. Živković, B. M. Babić, M. J. Kokunešoski, B. M. Jokić and I. M. Karadžić, *Biochem Eng J*, 2015, **93**, 73–83.

7 S. Salgın, M. Çakal and U. Salgın, *Prep Biochem Biotechnol*, 2020, **50**, 148–155.

8 S. Velasco-Lozano, F. López-Gallego, J. Rocha-Martin, J. M. Guisán and E. Favela-Torres, *J Mol Catal B Enzym*, 2016, **130**, 32–39.

9 J. C. Wu, V. Selvam, H. H. Teo, Y. Chow, M. M. R. Talukder and W. J. Choi, *Biocatal Biotransformation*, 2006, **24**, 352–357.

10 B. Zou, L. Zhang, J. Xia, P. Wang, Y. Yan, X. Wang and I. O. Adesanya, *Appl Biochem Biotechnol*, 2020, **192**, 132–145.

11 F. N. N. Mohd Hussin, N. Attan and R. A. Wahab, *Enzyme Microb Technol*, 2020, **136**, 109506.

12 M. P. Marszałł and T. Siódmiak, *Catal Commun*, 2012, **24**, 80–84.

13 E. Ozyilmaz, K. Etci and M. Sezgin, *Prep Biochem Biotechnol*, 2018, **48**, 887–897.

14 E. Yilmaz, M. Sezgin and M. Yilmaz, *J Mol Catal B Enzym*, 2011, **69**, 35–41.

15 E. Ozyilmaz, S. Sayin, M. Arslan and M. Yilmaz, *Colloids Surf B Biointerfaces*, 2014, **113**, 182–189.

16 S. Sayin, E. Yilmaz and M. Yilmaz, *Org Biomol Chem*, 2011, **9**, 4021–4024.

17 B. B. Lee, P. Ravindra and E. S. Chan, *Chem Eng Technol*, 2013, **36**, 1627–1642.

18 E. S. Chan, B. B. Lee, P. Ravindra and D. Poncelet, *J Colloid Interface Sci*, 2009, **338**, 63–72.

19 Y. Ji, Z. Wu, P. Zhang, M. Qiao, Y. Hu, B. Shen, B. Li and X. Zhang, *Biochem Eng J*, 2021, **169**, 107962.

20 M. M. Bradford, *Analytica Biochemistry*, 1976, **72**, 248–254.

21 J. Boudrant, J. M. Woodley and R. Fernandez-Lafuente, *Process Biochemistry*, 2020, **90**, 66–80.

22 R. A. Sheldon and S. van Pelt, *Chem Soc Rev*, 2013, **42**, 6223–6235.

23 Y. Liu, Q. Jin, L. Shan, Y. Liu, W. Shen and X. Wang, *Ultrason Sonochem*, 2008, **15**, 402–407.

24 K. Won, S. Kim, K. J. Kim, H. W. Park and S. J. Moon, *Process Biochemistry*, 2005, **40**, 2149–2154.

25 C. H. Yang, C. C. Yen, J. J. Jheng, C. Y. Wang, S. S. Chen, P. Y. Huang, K. S. Huang and J. F. Shaw, *Molecules*, 2014, **19**, 11800–11815.

26 S. S. Betigeri and S. H. Neau, *Biomaterials*, 2002, **23**, 3627–3636.

27 E. Onoja, S. Chandren, F. I. A. Razak and R. A. Wahab, *J Biotechnol*, 2018, **283**, 81–96.

28 M. Weng, C. Xia, S. Xu, Q. Liu, Y. Liu, H. Liu, C. Huo, R. Zhang, C. Zhang and Z. Miao, *Colloid Polym Sci*, 2022, **300**, 41–50.

29 B. Jia, C. Liu and X. Qi, *Fuel Processing Technology*, 2020, **210**, 106578.

30 S. Zhang, W. Shang, X. Yang, S. Zhang, X. Zhang and J. Chen, *Bull Korean Chem Soc*, 2013, **34**, 2741–2746.

31 E. Parandi, M. Safaripour, M. H. Abdellattif, M. Saidi, A. Bozorgian, H. Rashidi Nodeh and S. Rezania, *Fuel*, 2022, **313**, 123057.

32 J. Zhao, M. Ma, X. Yan, G. Zhang, J. Xia, Z. Zeng, P. Yu, Q. Deng and D. Gong, *Food Chem*, 2022, **379**, 132–148.

33 A. Ameri, F. Asadi, M. Shakibaie, A. Ameri, H. Forootanfar and M. Ranjbar, *Appl Biochem Biotechnol*, 2022, **194**, 2108–2134.

34 A. K. Tamo, I. Doench, A. M. Helguera, D. Hoenders, A. Walther and A. O. Madrazo, *Polymers (Basel)*, 2020, **12**, 1–24.

35 A. Wassilkowska and T. Woźniakiewicz, *Solid State Phenomena*, 2015, **231**, 139–144.

36 E. Yilmaz, K. Can, M. Sezgin and M. Yilmaz, *Bioresour Technol*, 2011, **102**, 499–506.

37 I. Bustos-Jaimes, Y. García-Torres, H. C. Santillán-Uribe and C. Montiel, *J Mol Catal B Enzym*, 2013, **89**, 137–141.

38 I. Bustos-Jaimes, W. Hummel, T. Eggert, E. Bogo, M. Puls, A. Weckbecker and K. E. Jaeger, *ChemCatChem*, 2009, **1**, 445–448.

39 F. Kartal and A. Kilinc, *Biotechnol Prog*, 2012, **28**, 937–945.

40 Y. Gao, R. Zhong, J. Qin and B. Lin, *Chem Lett*, 2009, **38**, 262–263.

41 E. M. Hill, J. M. Broering, J. P. Hallett, A. S. Bommarius, C. L. Liotta and C. A. Eckert, *Green Chemistry*, 2007, **9**, 888–893.

42 D. Deng, Y. Zhang, A. Sun and Y. Hu, *Cuihua Xuebao/Chinese Journal of Catalysis*, 2016, **37**, 1966–1974.

43 F. Bellezza, A. Cipiciani, G. Cruciani and F. Fringuelli, *J Chem Soc Perkin 1*, 2000, **24**, 4439–4444.

44 M. Mangiagalli, H. Carvalho, A. Natalello, V. Ferrario, M. L. Pennati, A. Barbiroli, M. Lotti, J. Pleiss and S. Brocca, *Int J Biol Macromol*, 2020, **150**, 930–940.

45 G. R. Castro and T. Knubovets, *Crit Rev Biotechnol*, 2003, **23**, 195–231.

46 D. Holtmann and F. Hollmann, *Molecular Catalysis*, 2022, **517**, 112035.

47 A. Kumar, K. Dhar, S. S. Kanwar and P. K. Arora, *Biol Proced Online*, 2016, **18**, 1–11.

48 J. S. Deetz and J. D. Rozzell, *Trends Biotechnol*, 1988, **6**, 15–19.

49 U. T. Bornscheuer, *Angewandte Chemie - International Edition*, 2003, **42**, 3336–3337.

50 L. Fernández, L. Gómez, H. L. Ramírez, M. L. Villalonga and R. Villalonga, *J Mol Catal B Enzym*, 2005, **34**, 14–17.

51 K. M. Polizzi, A. S. Bommarius, J. M. Broering and J. F. Chaparro-Riggers, *Curr Opin Chem Biol*, 2007, **11**, 220–225.

52 C. M. Soares, V. H. Teixeira and A. M. Baptista, *Biophys J*, 2003, **84**, 1628–1641.

53 A. L. Serdakowski and J. S. Dordick, *Trends Biotechnol*, 2008, **26**, 48–54.

54 C. Ortiz, M. L. Ferreira, O. Barbosa, J. C. S. Dos Santos, R. C. Rodrigues, Á. Berenguer-Murcia, L. E. Briand and R. Fernandez-Lafuente, *Catal Sci Technol*, 2019, **9**, 2380–2420.

55 H. J. Park, K. Park and Y. J. Yoo, *Mol Simul*, 2013, **39**, 653–659.

56 J. Sangster, *J Phys Chem Ref Data*, 1989, **18**, 1111–1227.

57 C. Reichardt and T. Welton, *Appendix A. Properties, Purification, and Use of Organic Solvents*, 2010, vol. 16.

58 A. J. Leo, *Chem Rev*, 1993, **93**, 1281–1306.

59 H. F. Carvalho, V. Ferrario and J. Pleiss, *J Chem Theory Comput*, 2021, **17**, 6570–6582.

60 T. Kulschewski, F. Sasso, F. Secundo, M. Lotti and J. Pleiss, *J Biotechnol*, 2013, **168**, 462–469.

61 C. José, R. D. Bonetto, L. A. Gambaro, M. D. P. Guauque Torres, M. L. Foresti, M. L. Ferreira and L. E. Briand, *J Mol Catal B Enzym*, 2017, **71**, 95–107.

62 C. Ortiz, M. L. Ferreira, O. Barbosa, J. C. S. Dos Santos, R. C. Rodrigues, Á. Berenguer-Murcia, L. E. Briand and R. Fernandez-Lafuente, *Catal Sci Technol*, 2019, **9**, 2380–2420.

63 B. Zieniuk, A. Fabiszewska and E. Białecka-Florjańczyk, *Bioprocess Biosyst Eng*, 2020, **43**, 605–613.

64 M. Mangiagalli, H. Carvalho, A. Natalello, V. Ferrario, M. L. Pennati, A. Barbiroli, M. Lotti, J. Pleiss and S. Brocca, *Int J Biol Macromol*, 2020, **150**, 930–940.

65 L. Wang, W. Du, D. Liu, L. Li and N. Dai, *J Mol Catal B Enzym*, 2006, **43**, 29–32.

66 G. T. Jeong and D. H. Park, *Appl Biochem Biotechnol*, 2008, **148**, 131–139.

67 D. Royon, M. Daz, G. Ellenrieder and S. Locatelli, *Bioresour Technol*, 2007, **98**, 648–653.

68 D. Van Der Spoel, E. Lindahl, B. Hess, G. Groenhof, A. E. Mark and H. J. C. Berendsen, *J Comput Chem*, 2005, **26**, 1701–1718.

69 C. Li, T. Tan, H. Zhang and W. Feng, *Journal of Biological Chemistry*, 2010, **285**, 28434–28441.

70 N. Agmon, *Chem Phys Lett*, 1995, **244**, 456–462.

Chapter 5

Horse Liver Alcohol Dehydrogenase

5.1 A kinetic and computational study

Steady-state kinetics of enzymes involving coenzymes refers to the study of enzyme-catalyzed reactions in a condition in which the concentration of substrates, products, and enzyme-coenzyme complexes remains relatively constant over time. This analysis focuses on determining the rate of enzymatic reactions, understanding the enzyme's affinity for its substrate and coenzyme, elucidating the turnover rate, and exploring the mechanisms that govern the interactions between the enzyme, the substrate, and its coenzyme during the reaction process[1]. Numerous attempts employing steady-state kinetics have been undertaken to explore the intricate relationship between substrate structure and catalytic rate of horse liver alcohol dehydrogenase (HLADH). These investigations faced challenges arising from ordered reaction mechanism of the enzyme, as elucidated by Theorell and Chance in 1951[2]. Their proposed bi-bi ordered mechanism, that is visually depicted in red in Scheme 1, where the cofactor ($NADH/NAD^+$) is the first to bind to the enzyme and the last to leave the active site:

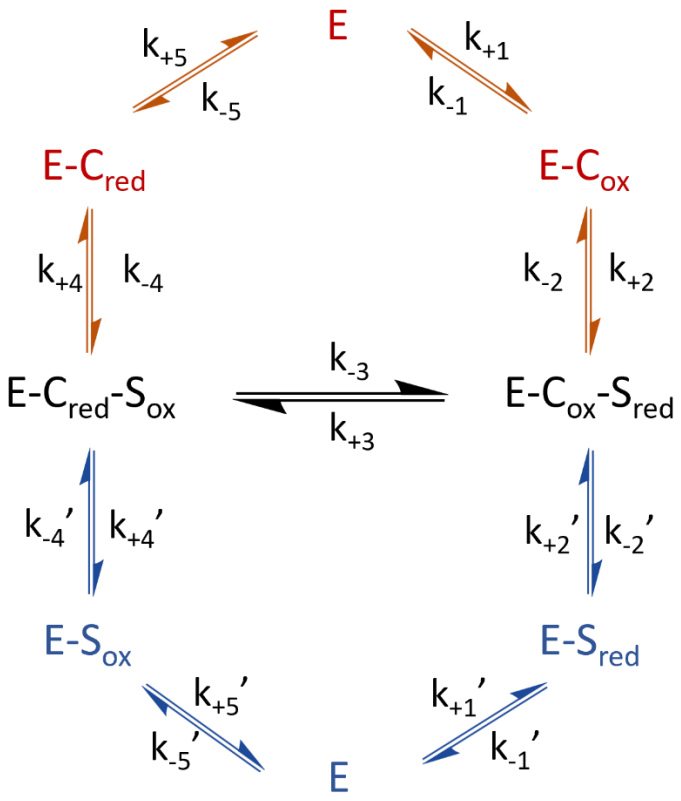

Scheme 1: Global reaction scheme, where Cred and Cox are respectively the two forms of the cofactor: NADH and NAD⁺, and Sox and Sred correspond to the carbonyl and alcoholic substrates respectively.

Among various reported reaction steps, the dissociation of the binary E-cofactor product complex was identified as the rate-determining step, as pointed out by Dalziel in 1963[3]. The kinetic constants of this process were estimated by Plapp through kinetic simulations of a family of progress curves using KIN SIM and FITSIM[4]. This approach allowed establishing the relationships between the kinetic constants and the affinity constant, determining which of the constants was the catalytic one. Specifically, the Michaelis constant serves as a crucial indicator, representing the equilibrium

constant governing both the formation and dissociation processes of E-cofactor complexes or E-cofactor-substrate complexes. On the other hand, the catalytic constant delineates the dissociation constant specifically pertaining to the E-cofactor product complex. The described relationships are reported in Table 1.

Table 1: Relationship between kinetic constants with both affinity and catalytic constants.

oxidation	*reduction*
$K_M(NAD^+) = \frac{k_{+5}}{k_{+1}}$	$K_M(NADH) = \frac{k_{-1}}{k_{-5}}$
$K_M(RCH_2OH) = \frac{k_{+4}}{k_{+2}}$	$K_M(RCHO) = \frac{k_{-2}}{k_{-4}}$
$k_{cat}(ox) = k_{+5}$	$k_{cat}(red) = k_{-1}$

Meticulous investigations involving initial velocity studies by varying substrate concentrations provided support for the Theorell–Chance mechanism, but more intricate mechanisms also emerge from steady-state kinetic studies. Indeed, at least another reaction pattern, that can occur with high relative substrate concentrations, has been proposed[5] (blue path in Scheme 1). According to this reaction mechanism, the enzyme can initially bind the substrate, forming an E-substrate complex to which the cofactor will subsequently bind at different rates depending on the substrate under examination. This process thus influences kinetic parameters. Moreover, the possibility of abortive ternary complexes (i.e. non-productive), both in reduction (E-NADH-RCH_2OH) and in oxidation (E-NAD^+-RCHO) have been proposed. Being the possible number of ternary complexes large and debated, such complexes are not reported in the Scheme 1. The formation

of abortive E–NAD^+–aldehyde and E–NADH–alcohol complexes is particularly evident under very high substrate concentrations[6,7]. Notably, when ethanol is the alcohol substrate, NADH dissociates slower from the abortive enzyme–NADH–alcohol complex, showing substrate inhibition. Conversely, with cyclohexanol as the substrate, NADH dissociation occurs more rapidly, demonstrating also substrate activation[8,9]. Additionally, benzyl alcohol forms an abortive enzyme–NADH–alcohol complex, impeding the dissociation of NADH[10]. Product inhibition investigations proved the kinetic importance of the abortive ternary E–cofactor–substrate complexes in the overall reaction scheme. These findings underline the diverse and nuanced effects of different alcohols on the enzyme's behavior, highlighting the complexity of the reaction mechanisms beyond the first proposal[5]. As just described, HLADH is an extensively studied and well-characterized enzyme from both a kinetic and structural perspective. Specifically, researchers have investigated the impact of substrate structure, inhibition or activation by substrate and product through the formation of ternary complexes, and how enzyme kinetics vary with different metals[5,9,11]. Throughout these explorations, and in practical applications, the cofactor concentration is typically kept constant, at or below than 0.2 mM for the reduction[12,13] and approximately at 1 mM for the oxidation reaction[14,15]. In this study we aimed to investigate the effect of both substrate and cofactor concentration on enzyme activity. In the present work, kinetic anomalies under variable cofactor concentration have been observed. Thus, we used the aid of molecular dynamics (MD) simulations to rationalize this behavior at molecular level.

5.1.1 Materials

Horse Liver Alcohol Dehydrogenase (HLADH recombinant, expressed in E. coli, ≥0.5 U/mg), β-nicotinamide adenine dinucleotide hydrate (NAD^+, grade ≥ 96.5%), nicotinamide adenine dinucleotide reduced (NADH, grade ≥ 94.0%), cyclohexanol (CH-OH), cyclohexanone (CH-one), 3-pentanone (DEK), 3-pentanol (3-PeOH), benzaldehyde (Bnz) and benzyl alcohol (Bn-OH) were purchased from Merck. Enzyme and substrate were used with no further purification. All other chemicals used were of analytical grade.

5.1.2 Measurements of Enzyme Kinetics

Three distinct substrate types were chosen to assess the enzyme's activity concerning cyclic, benzyl, and open-chain substrates, both in oxidation and reduction reactions. The catalytic activity of HLADH was evaluated through the oxidation of these substrates into products, coupled with the simultaneous reduction reaction of NAD^+ into NADH, and vice versa. The standard assay was performed at 25°C in a Tris-HCl buffer solution (50 mM, pH 8.0) containing a substrate concentration of 10 mM. The cofactor concentrations were varied to establish the enzyme's kinetic profile, specifically NAD^+ ranging from 0 to 1.0 mM and NADH from 0 to 0.4 mM. The enzyme concentration was maintained at 0.5 μM, except for DEK, where it was set at 1 μM. Additionally, to outline the kinetics of cyclohexanone, the pH of the Tris-HCl buffer solution was varied within the enzyme's stability range, between pH 7 and 9. Enzyme activity measurements were conducted through spectrophotometric kinetics at a wavelength of 340 nm, monitoring the changes in NADH absorbance. These measurements were performed using a Shimadzu UV-160A instrument, and each assay was repeated three

times for accuracy and reliability. Figure 1 shows the kinetic profile of the selected substrates as a function of cofactor concentration.

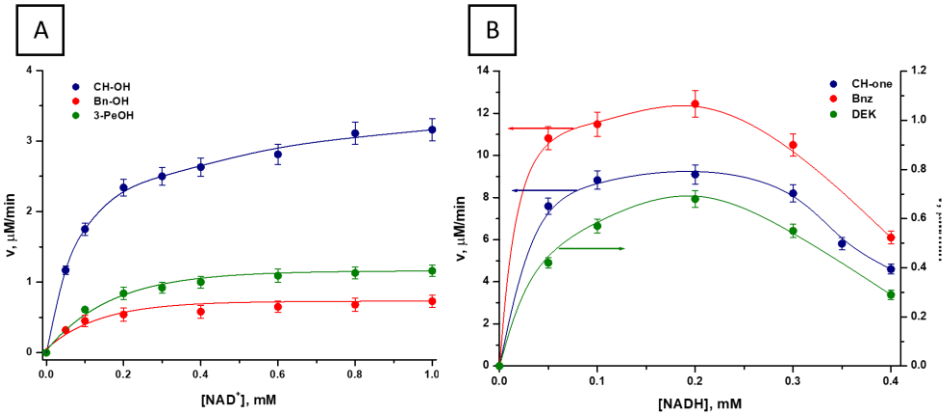

Figure 1: (A) Effect of NAD⁺ concentration on the reaction rate for the three substrates: cyclohexanol (CH-OH), benzyl alcohol (Bn-OH), and 3-pentanol (3-PeOH) on the left; (B) effect of NADH concentration on the reduction reaction rate for the three substrates: cyclohexanone (CH-one), benzaldehyde (Bnz), and 3-pentanone (DEK) on the right.

As can be seen from the profile in Figure 1A, the rate of oxidation reaction for all three substrates increases by increasing cofactor concentration until reaching a plateau at saturating concentration. Instead, as depicted in the profile on the right (Figure 1B), an unusual pattern has been noticed. Contrary to the expected Michaelis-Menten behavior, the kinetics exhibited, with varying NADH concentrations, deviates from the typical model. Rather than reaching a plateau at saturating coenzyme concentrations, the reaction rate initially rises to a maximum, after which it declines. This effect has been previously observed in the case of alcohol dehydrogenase from Saccharomyces cerevisiae for the reduction reaction of formaldehyde[16]. In this study, they observed that when the NADH concentration ranged

between 8 to 14 mM, the reaction followed Michaelis-Menten kinetics. However, at higher (25-40 mM) or lower (6-8 mM) concentrations of NADH, the enzyme exhibited unconventional behavior, strongly suggesting the presence of a cofactor inhibition phenomenon, although they do not delve into further mechanistic details. In the present work we observed similar inhibition behavior for the reduction reaction in all the three studied substrates. Therefore, this divergence from the conventional Michaelis-Menten kinetics requires a deeper exploration of the underlying factors that influence the reaction behavior with varying cofactor concentrations. Typically, initial rate equations are formulated on the basis of the Michaelis constant. However, as just described, in the case of two-substrate reactions, the Michaelis constant for each substrate (K^{S}_{M}) and cofactor (K^{C}_{M}) tends to vary with the concentration of the other. The kinetic parameters of both reactions, oxidation and reduction, at non inhibitory cofactor concentrations (0.01-0.05 mM NADH; 0.1-1.0 mM NAD^+), are reported in Table 2.

Table 2: The kinetic parameters for the oxidation and reduction reactions by varying both the substrate and cofactor concentrations.

oxidation			*reduction*		
	K_M, mM	k_{cat}, s^{-1}		K_M, mM	k_{cat}, s^{-1}
CH-OH	1.04	0.06	*CH-one*	7.6	0.3
NAD+	0.08		*NADH*	0.03	
Bn-OH	0.03	0.02	*Bnz*	0.04	0.3
NAD+	0.09		*NADH*	0.008	
3-PeOH	3.5	0.02	*DEK*	0.3	0.003
NAD+	0.2		*NADH*	0.004	

Enzyme affinity values observed for both alcoholic and carbonyl substrates closely align with those documented in literature[7,10,17–21]. The high enzyme affinity for benzyl substrates can be reasonably ascribed, at least in part, to the hydrophobic characteristics of its active site. Furthermore, within the entry cavity of the substrate close to the catalytic zinc ion, two specific residues, namely Phe-93 and Phe-319, can establish pi-stacking interactions with the benzyl substrates, contributing to their enhanced affinity for the enzyme. If we consider the mechanism reported in red in Scheme 1 as the sole mechanism, the K^{C}_{M} and the reaction k_{cat}, related to steps involving only the enzyme and coenzyme, should not be affected by the substrate. In more detail, the K^{C}_{M} represents the equilibrium constant of the cofactor dissociation (consumed)/association (new) process, and the catalytic constant has been identified as the kinetic constant for the cofactor dissociation step, which is the rate determining step[4]. Furthermore, the kinetic parameters can be strongly influenced by the formation of the abortive ternary complexes described above. For example, in the presence of an excess of cyclohexanol, which has a k_{cat} value three times higher than the other two substrates, it has been demonstrated that NADH dissociates more rapidly from the abortive ternary complex formed compared both ethanol and the product complex E-NADH[8]. In addition to the variable affinity of the cofactor depending on the substrate, it is evident from the reduction reaction data that NADH consistently exhibits in all cases a much greater affinity than its oxidized form. It is precisely in this higher affinity of NADH that we sought the reason for the anomalous behavior observed in the kinetic profile (Figure 1B). To better understand this behavior, we chose a synergistic computational-kinetic approach. Since the anomalous kinetic trend with increasing NADH concentration appears to be independent of the

substrate under examination, cyclohexanone was chosen as substrate for further experiments. This choice was motivated by its convenience from a kinetic perspective. Although it has a high K^{S}_{M}, it exhibits a good k_{cat}, and the balance between the two parameters result in a suitable reaction velocity for the experimental set-up. This does not hold true for the reduction reaction of benzaldehyde, which is very fast. Conversely the reaction for pentanone is rather slow due to its very low k_{cat}. So, to better understand the anomalous behavior from a kinetic point of view, we conducted kinetic analyses of cyclohexanone at different NADH concentrations, ranging from non-inhibitory to inhibitory levels, from 0.05 to 0.5 mM. All lines at different cofactor concentrations are depicted together in a Lineweaver-Burk plot in Figure 2.

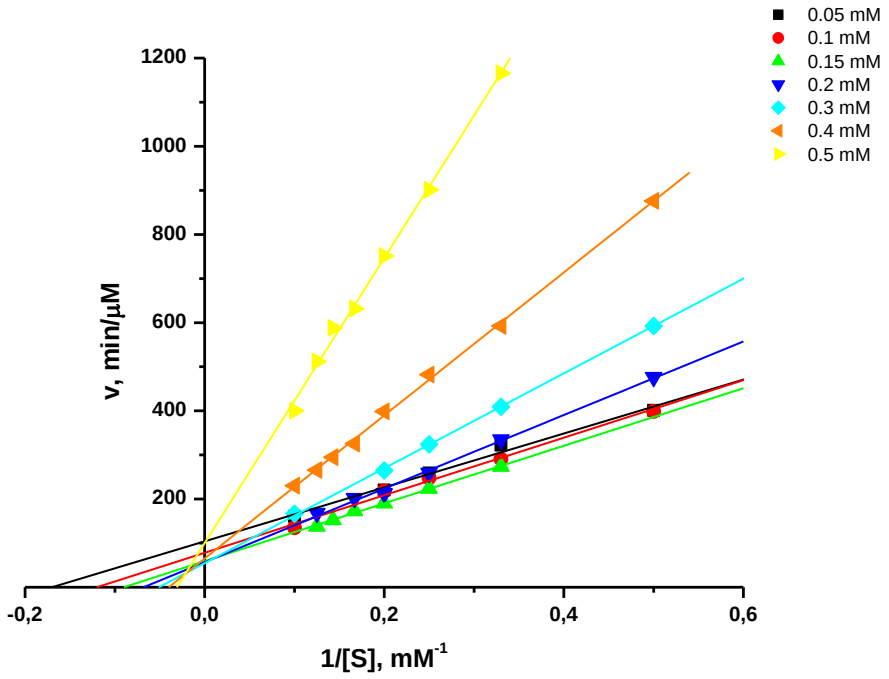

Figure 2: Lineweaver–Burk plot (or double reciprocal plot); a graphical representation of the Michaelis–Menten equation of enzyme kinetics from non-inhibitory to inhibitory coenzyme concentrations.

The effect of NADH concentration on K^S_M (A) and k_{cat} (B) of cyclohexanone is reported in Figure 3.

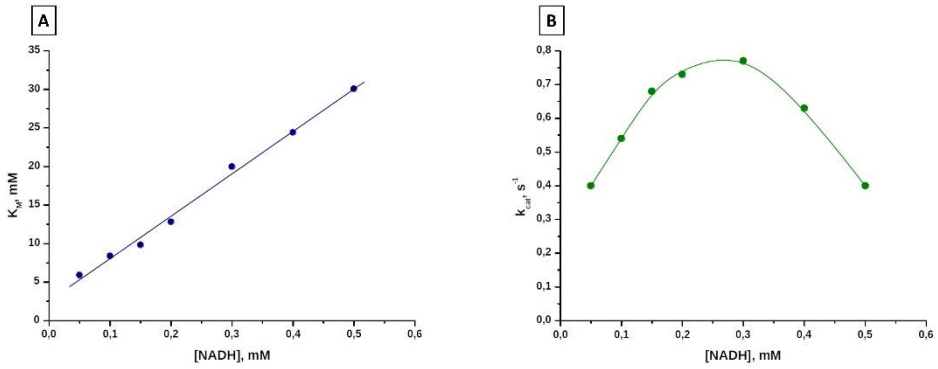

Figure 3: Trends of K^S_M (A) and k_{cat} (B) of the reduction reaction as coenzyme concentration rises from non-inhibitory to inhibitory range.

From the trend shown in Figure 3A it is evident that, as the coenzyme concentration increases, there is a noticeable rise in K^S_M, from 6 to 30, going from 0.05 mM to 0.5 mM of NADH, indicating a rapidly decrease in the affinity of the enzyme for the substrate. At the same time, the catalytic constant (Figure 3B) shows a bell-shaped trend, suggesting that the enzyme catalytic efficiency initially increases from 0.4 to 0.8 s^{-1} at 0.3 mM of NADH and then decreases to 0.4 s^{-1} with rising NADH concentration up to 0.5 mM. Based on these experimental results, a simple analysis of K^S_M and k_{cat} values does not provide information on the microscopic mechanisms occurring at inhibitory cofactor concentrations. Therefore, in the following sections, the results obtained from a series of molecular dynamics simulations performed by adding supplementary non-catalytic NADH molecules to clarify this anomalous behavior are reported.

5.1.3 Molecular Dynamics Simulations

To rationalize the different behavior of HLADH at low and high concentrations of NADH, two sets of molecular dynamics (MD) simulations were conducted starting from the crystallographic structure with PDB_ID 7K35. All graphical representations of the computational part were made with VMD software. In the first set, labelled as '2-NADH', simulations were performed on the holo-protein with one catalytic NADH and one substrate molecule present in each of the two catalytic sites (see panel A of Figure 4 for a representative configuration of the active site). According to the X-ray-derived structure[9], the reaction cavity has two potential entrances: a larger one primarily for cofactor binding and a smaller one for substrate binding (see panel A of Figure 4).

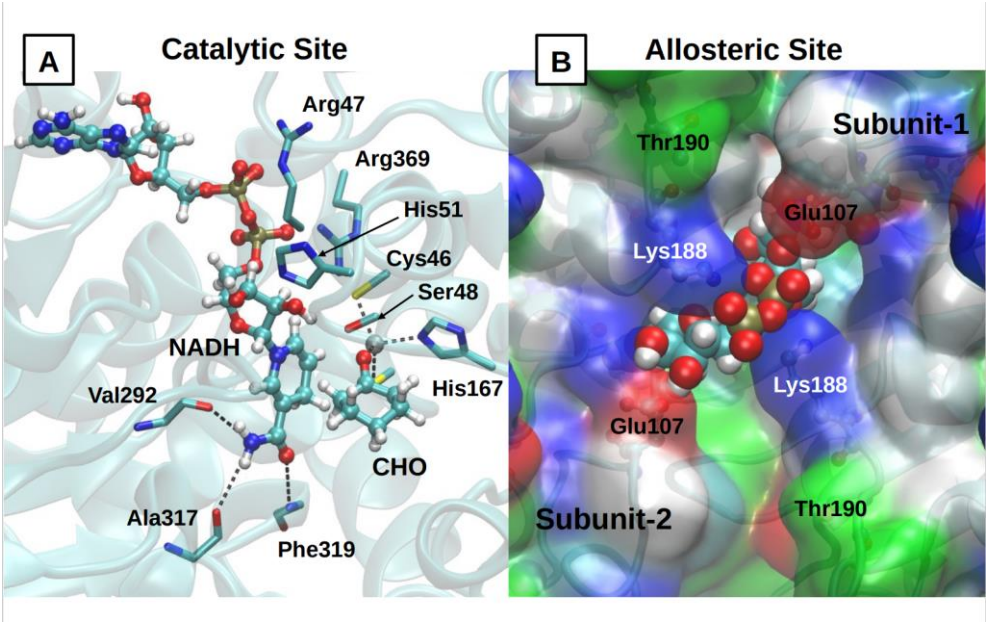

Figure 4: Focus on the reaction site and allosteric site of the cofactor are reported. In panel A, interactions with Arg47, Val292, Ala317, Phe319, and Arg369 that stabilize the NADH in the catalytic site are shown. In panel B, interactions with the

two Lys188 and Glu107, which constitute the allosteric pocket for the additional NADH, are highlighted.

In the second set, the simulations were conducted with additional NADH molecules placed in contact with different parts of the enzyme using docking procedures with the program Vina[22]. Two of the three lowest-energy docking configurations have the additional NADH molecule in close proximity to the active site, one at the cofactor entrance and the other at the substrate entrance (see Figure 5).

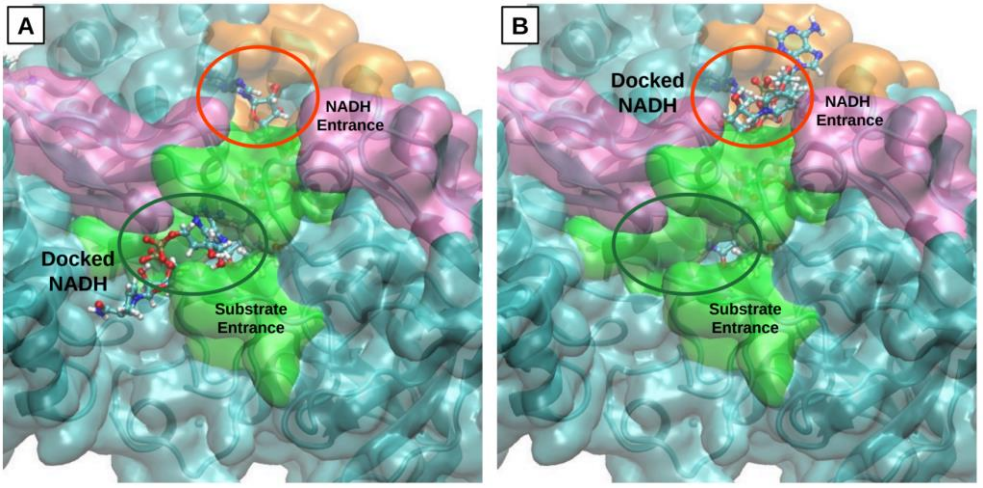

Figure 5: Docked NADH configurations at substrate (panel A) and cofactor (panel B) entrances obtained with docking procedure.

Interestingly, the lowest-energy docking configuration found the additional NADH molecule localized on the opposite side of the catalytic site, in a cavity between the two subunits of HLADH (see panel B of Figure 4 for a representative configuration). We refer this cavity as the allosteric site for the reasons given below. In summary, the three identified docking sites are: (i) at the substrate entrance of the reaction cavity (see Figure 5 panel A); (ii) at the NADH entrance of the reaction cavity (see Figure 5 panel B); (iii) in the

allosteric site, between the two enzyme subunits (Figure 4 panel B). Three preliminary 100 ns-long MD simulations were performed starting from the three docked configurations to assess their stability. The Root Mean Square Deviation (RMSD) of the additional NADH molecule with respect to the corresponding starting structure, calculated over the three simulations (reported in Figure 6), shows that only the allosteric-docked configuration is stable.

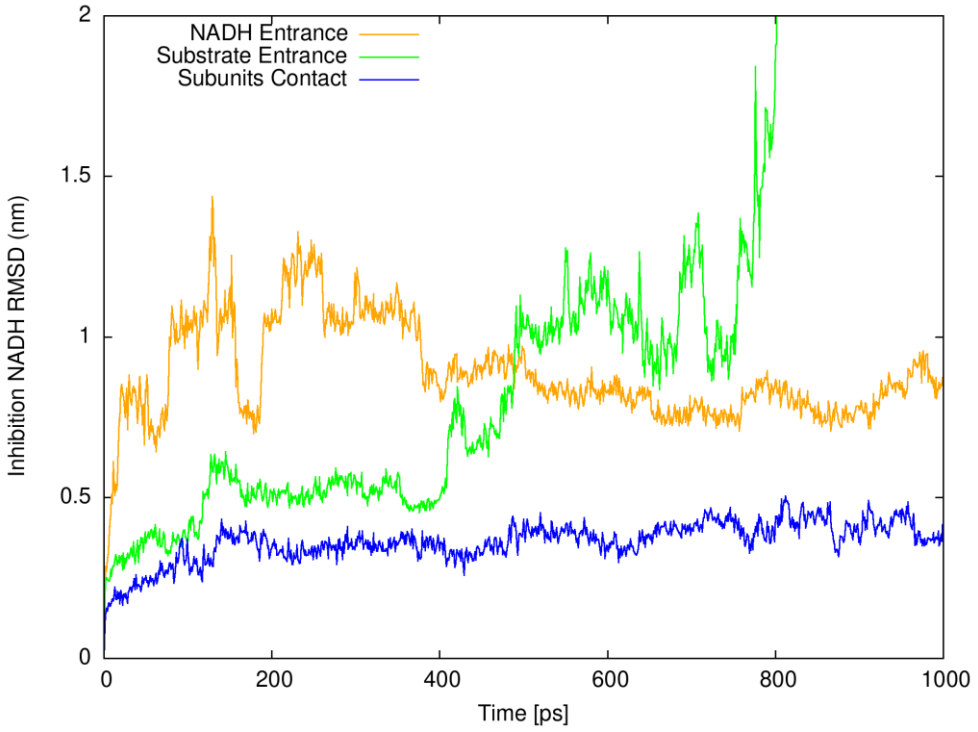

Figure 6: Docked NADHs Root Mean Square Deviation (RMSD) comparison over 100 ns MD simulations.

The residues primarily responsible for stabilizing the additional cofactor molecule at the allosteric site are two Lys-188 residues, one in each monomer, which interact with the two phosphate groups of NADH (see Figure 4 panel B). Additionally, the Glu-107 side chains from each monomer

play a role in stabilizing the hydroxide from the ribose groups. In the other two cases, the additional NADH molecule instead moves away from its initial position. On the basis of these results, in the following we only consider simulations of the allosteric-docked configurations for comparison with the simulation of the 2-NADH system. We will refer this set of simulations as '3-NADH'. For both the 2-NADH system and the 3-NADH one, we performed three 100-ns long simulations using different initial velocities. The Root Mean Square Fluctuation (RMSF) per residue was then calculated over all protein configurations sampled throughout the 300 ns of simulation for both the 2-NADH and 3-NADH systems. As shown in panel B of Figure 7, the RMSF is consistently lower in the allosteric-docked system (red line) compared to the 2-NADH system (blue line). This difference is further highlighted by examining the difference of the RMSF per residue between the two systems (black line in the same figure).

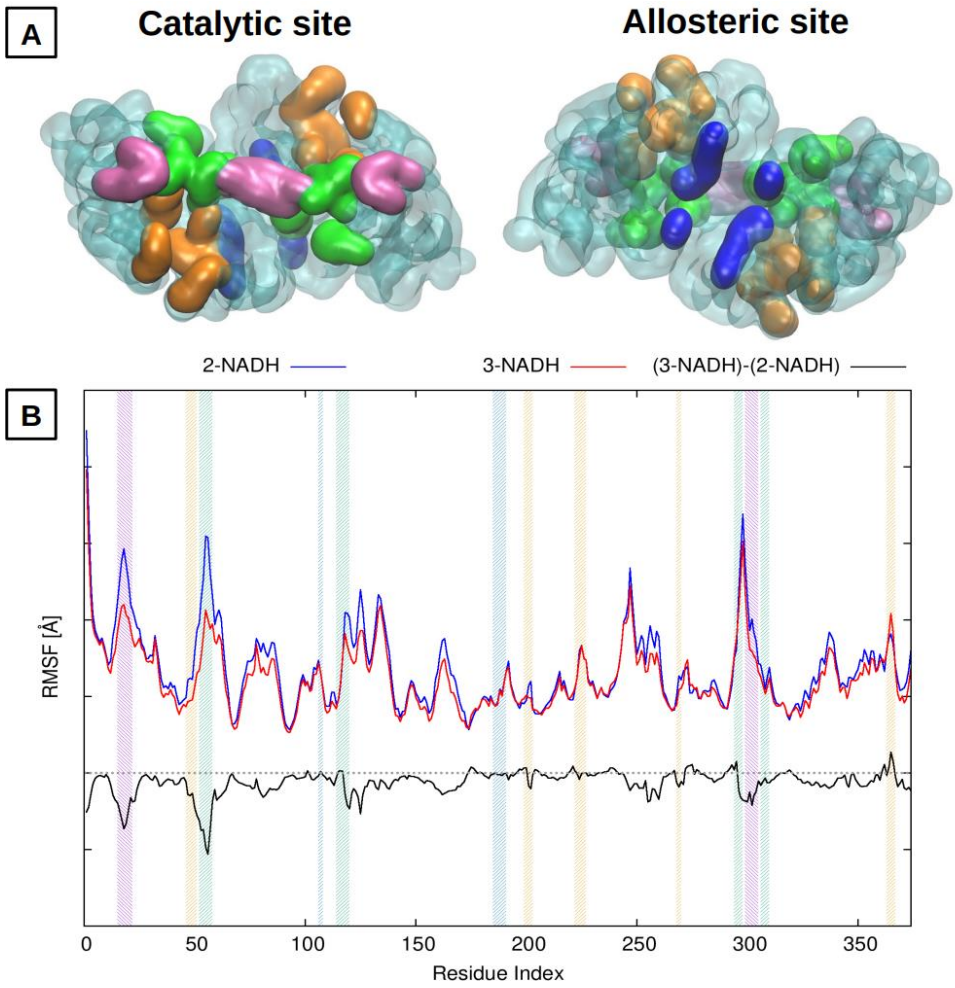

Figure 7: The protein and its secondary structure elements are reported in transparency in panel A. The protein portion constituting the NADH cavity (orange), the substrate cavity (green) and allosteric cavity (blue) are highlighted. The pink regions correspond to residues that are not directly connected to the catalytic site but are strongly influenced by the NADH inhibition effect in the simulations. Root Mean Square Fluctuation per residue averaged over the two subunits for the two sets of simulations are shown in panel B. The RMSF difference between the 3-NADH simulations and 2-NADH ones is also reported in black. The residues constituting the substrate and NADH cavity are reported in green and orange, respectively. Also, two regions with a significant RMSF variation, but not corresponding to any specific cavity, are reported in pink.

The figure also highlights the protein regions corresponding to the entrance of the catalytic NADH and the substrate, depicted in Figure 7A as orange

and green regions, respectively. Also, the residues responsible for the allosteric site are shown in blue. The residue indexes corresponding to these regions are similarly highlighted with their respective color palette in the RMSF plot in panel B. Additionally, regions with high structural flexibility are highlighted in pink in both panels. Overall, it is evident that the occupation of the allosteric site induces a global stiffening of the protein structure and in particular of the regions corresponding to the access points to the catalytic cavity. For this reason, we named this occupation site as the allosteric site. Residues 50-60 and 295-300, which define the protein surface separating the two entrances (the two green regions in contact, and surrounded by the pink ones), exhibit considerable structural flexibility in the 2-NADH system. In particular, the protein region composed of the residues between Asp-50 and Pro-60 shows the largest RMSF difference. High fluctuations between these regions result in a widening of the catalytic cavity, forming a unique crevice that exposes both the nicotinamide moiety of the catalytic NADH and the substrate to the solvent. The second region that exhibits the most significant difference between the two sets is formed by the residues from Trp-15 to Pro-20 (pink region). This region has direct interactions with the portions between residues 50 and 60 from each subunit (green regions), thus exhibiting concerted movements with such regions. To gain a deeper understanding of possible correlated motions induced by the presence of the additional NADH, an essential dynamics (ED) analysis was performed using the whole conformational space sampled along all sets of simulations. The ED analysis performed on the backbone atoms revealed that the two systems exhibit quite different dynamics. In fact, projection of the 2-NADH and 3-NADH simulations onto the first eigenvector, which accounts for the largest backbone fluctuations, reveals rather distinct distributions (see Figure 8).

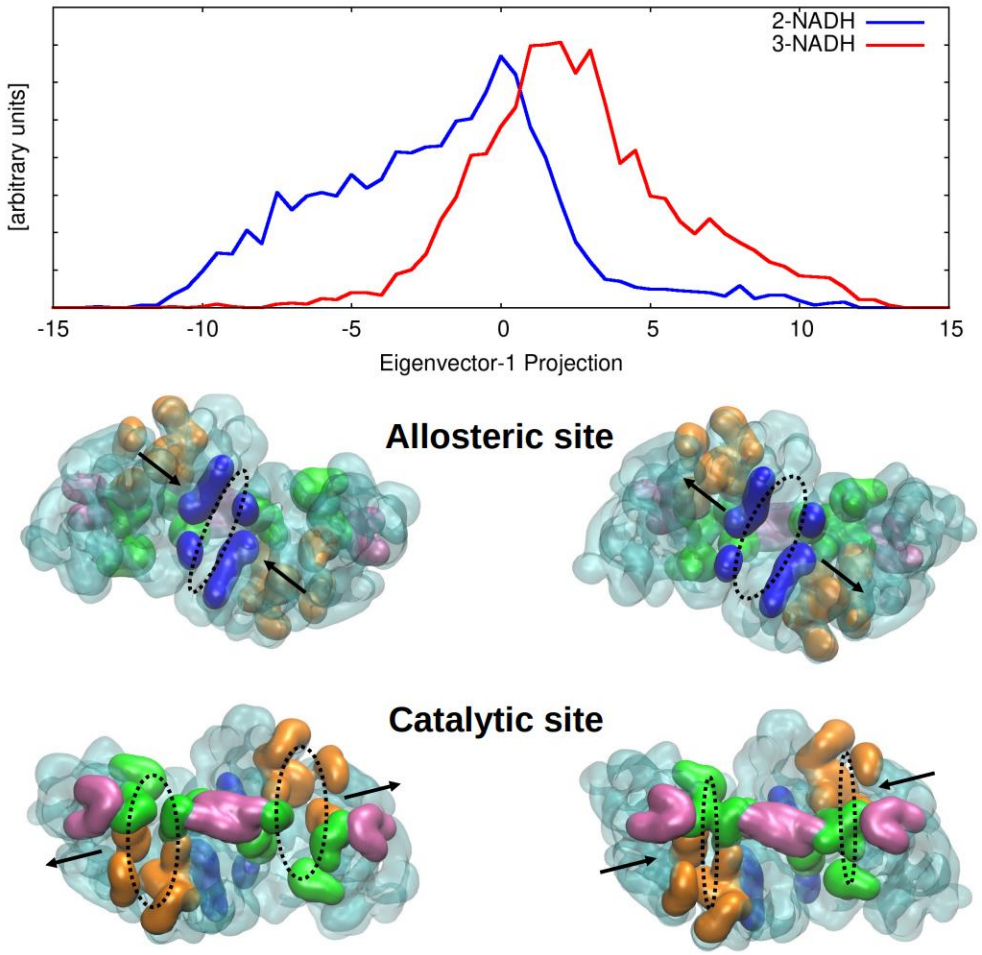

Figure 8: Projection of the system's configurations sampled in the 2-NADH and 3-NADH MD simulations on the first eigenvector obtained from an Essential Dynamics analysis of the backbone atoms. Negative values correspond to a wider reaction site and smaller allosteric cavity. Conversely, positive values correspond to a narrower reaction site and a larger allosteric cavity. The protein region corresponding to the entrance of the catalytic NADH is highlighted in orange, the one corresponding to the substrate entrance in green and the allosteric cavity in blue.

The first eigenvector involves correlated motions of the catalytic cavity and the potentially inhibitory allosteric site. In particular, the motion of the two cavities shows an anticorrelated behavior: as the catalytic cavities widen, the

allosteric site contracts, and vice versa. Generally, in the 2-NADH simulations, the enzyme shows broader catalytic cavities (blue line in Figure 8), resulting in a smaller size of the cavity that could accommodate the additional NADH. Conversely, in the 3-NADH simulations, the presence of the additional NADH leads to a widening of the allosteric site and a narrowing of the catalytic site. This result is consistent with data reported in a crystallographic study[4] in which the catalytic site occupation was shown to induce a tilt of the two subunits, resulting in a "squeezing" of the cavity present between the two monomers. Hence, it is plausible to speculate that such a cavity may serve as a true allosteric site, influencing the geometric features of the catalytic site located on the opposite side of the enzyme. Based on the insights into the protein dynamics captured by the MD simulations, it is possible to infer the structural rationale behind the inhibitory effect of a high concentration of the NADH cofactor on the catalyzed carbonyl reduction.

On the basis of the structural and dynamical features derived from the computational data, it is possible to hypothesize a molecular rationale behind the unconventional kinetic behavior of HLADH. Concerning the measured k_{cat}, two distinct regimes were observed at low and high concentrations of NADH: up to a 0.2 mM (i.e. at non-inhibitory NADH concentrations), the k_{cat} increases, as expected for a Michaelis-Menten scheme; after reaching this turning point (i.e. at inhibitory NADH concentrations), the k_{cat} decreases. We attribute this effect to the presence of the NADH cofactor, not only in the catalytic cavity but also in the allosteric site. Previous studies[4] identified the reaction mechanism depicted in red in Scheme 1 as the prevalent path. The alternative scenario depicted in blue, where the substrate/product is associated/released before the cofactor, has been proposed as a minor path.

For the first reaction pathway in the scheme, the rate-limiting step (k_{cat}) is associated with the release of the "exhausted" cofactor, NAD^+. Although, no rate-limiting step was clearly identified for the second path, it is reasonable to expect that also in this scenario, the release of the product or the exhausted cofactor remains the rate-limiting step. In both mechanisms, the overall increased stiffness induced by the presence of the allosteric NADH would inevitably reduce the ability of the protein of release either the cofactor or the product after the conversion. Therefore, the critical concentration value can be associated with the point in which a significant amount of the enzymes in solution have an occupied allosteric site. Understanding the molecular determinants associated with allosteric regulations can play an important role in pharmaceutical compound design and, therefore, in medical treatments[23,24]. In particular, the HLADH behavior might serve a biological purpose in a possible negative feedback scheme induced by excess NADH, preventing over-reduction of crucial biomolecules. Below, we propose also a speculative explanation for the observed linear increase in K^S_M with increasing NADH concentration. This type of behavior has been observed also by others[5,16] but it was not discussed in detail. An increase of K^S_M could be explained by a decrease in the association rate of the substrate (which is at the denominator of K^S_M), and/or an increase in the dissociation rate of the product (which is at the numerator of K^S_M). The formation of the active E-cofactor-substrate ternary complex can be obtained either by an early association of the substrate to the apo-enzyme (k'_{-5} in the blue path of Scheme 1) or by its binding to the E-NADH complex (k_{-4} in the red path of Scheme 1). If both pathways are active, as proved in previous studies[5], the apparent substrate association constant will be a combination of the two. Therefore, the variation in the relative

population of the two paths will affect the K^S_M value. As reported in a previous crystallographic study[4,25], the association of the cofactor in the primary mechanism induces a conformational change that reduces size of the reaction cavity. Thus, we can assume that k_{-4} is smaller than k'_{-5}. Given that the amount of E-NADH complex depends on the NADH concentration, the increase in the latter will further shift the reaction ratio in favor of the early association of the complex E-ROH-NADH. This ternary complex would result from replacing the oxidized NAD^+ with a new NADH after the catalytic reduction reaction but before the release of the ROH product. From this branch, it has been proposed that both the product and the NADH would dissociate more rapidly than the product alone due to the interaction with a non-affine counterpart[8]. The formation of this complex would depend on the NADH concentration and, as its concentration increases, the likelihood of E-NADH-ROH complex formation would also increase. If the product dissociates more rapidly from this abortive ternary complex, this implies an increase in the apparent dissociation constant. This results in an increase in the numerator of K^S_M, and consequently, of K^S_M itself. Although the hypothesis of the discussed abortive ternary complex is not directly supported by measurements, it can help to explain the increase in K^S_M with the increasing cofactor concentration.

5.1.4 Conclusions

The study presented here on Horse Liver Alcohol Dehydrogenase (HLADH) offers a profound understanding of its kinetic behavior and structural dynamics, unraveling complex mechanisms governing its catalytic activity and cofactor interactions. Deviation from traditional Michaelis-Menten kinetics, showcasing a slowdown in the catalytic rate in the presence of high

NADH concentrations, is observed. Through molecular dynamics simulations, a potential allosteric site is identified, elucidating how excessive cofactor concentrations influence protein dynamics and catalytic properties. Specifically, structural changes induced by inhibitory NADH concentrations are demonstrated to reduce protein flexibility and alter the size of the catalytic cavities, offering insights into the inhibitory mechanism at high cofactor concentrations. This comprehensive investigation into HLADH's kinetics and structural dynamics has revealed intricate aspects of its catalytic mechanisms, laying a foundation for further exploration in enzymology and biocatalysis.

5.2 HLADH entrapped in alginate beads.

The utilization of alginate beads for enzyme entrapment has gained widespread popularity due to its simplicity, rapidity, cost-effectiveness, and eco-friendliness[26]. Nevertheless, this support material is not free from defects, as it often exhibits low mechanical strength and experiences substantial loss of encapsulated biomolecules. These issues arise from the open structure, large pore size, and high hydrophilicity of alginate beads, which promote swelling behavior, ultimately diminishing the stability of the biocatalysts, and hindering their recyclability[27]. Specifically, alginate is a hydrophilic and water-soluble anionic polysaccharide that can be transformed into a more stable form when crosslinked with Ca^{2+} ions in an aqueous environment. However, when exposed to a sodium phosphate buffer solution, it has been theorized that an ion exchange process takes place between the Na^{+} ions of the external solution and the Ca^{2+} ions bound to the carboxylate groups of the polymannuronate sequences[28]. This ion exchange process amplifies the electrostatic repulsion between the carboxyl groups, leading to the relaxation

of the polysaccharide chains and an increase in gel swelling. This hypothesis is supported by the appearance of turbidity in the solution, which results from the release of calcium ions from the beads that react with phosphate, forming an insoluble salt under neutral or alkaline conditions. As the swelling process progresses, Ca^{2+} ions, which were initially bound to the carboxylate groups of the polyguluronate units responsible for crosslinking the hydrogel, are also exchanged with the Na^{+} ions of the buffer medium. This, in turn, reduces the degree of crosslinking in the support structure, causing a gradual collapse of the matrix. To address these limitations and enhance the stability of the matrix, and consequently, the controlled release of enzymes, researchers have explored the combination of sodium alginate with various synthetic and natural polymers[29–31]. This strategic blending has been shown to improve the characteristics of the material, making it suitable for a wide range of biomedical applications[32]. By improving matrix stability and controlling enzyme release, this approach allows to overcome the issues associated with pure alginate beads and expanding their utility in various fields. However, in our effort to address the swelling phenomenon, we have avoided using hybrid supports that would complicate the preparation process, extend the timeframe, increase costs, and produce a denser and less porous structure compared to the original support materials. Instead, we pursued two distinct methodologies. In the first approach, reported in the previous chapter, we entrapped *Candida rugosa* lipase within pure alginate beads and employed distilled water as the reaction and storage medium, thus avoiding the challenges associated with phosphate buffer. Conversely, in the second scenario, concerning the immobilization of horse liver alcohol dehydrogenase, we found a pronounced sensitivity of the enzyme to pH fluctuations within the reaction environment. Consequently, we opted to

replace the phosphate buffer with Tris-HCl buffer. That buffer, featuring a bulkier cation, resulted in a slower and more intricate exchange of calcium ion. Although this second improvement strategy was not entirely resolutive, we contemplated introducing calcium ions into the reaction and storage buffer to "reincorporate" them into the system.

5.2.1 Horse Liver Alcohol Dehydrogenase

Horse Liver Alcohol Dehydrogenase (HLADH) is an enzyme whose practical application is steadily increasing, as it shows a very broad substrate specificity; however, it has mainly been used in soluble form, and there are few publications in the literature concerning its immobilization. In particular, HLADH has been immobilized by adsorption on hydrophilic polymeric materials[33] and on porous silica particles both for enzymatic catalysis and for cofactor recycling in organic media[34]. It has also been covalently bonded onto glyoxyl-agarose[35], functionalized silica particles[36], epoxy resins[37] and poly(pyrrole) glass supports for electrochemical regeneration of the cofactor[38]. Here we report results on HLADH encapsulation onto alginate beads; in fact, unlike YADH, there are no papers, as far as we know, which involve its immobilization in these supports. To improve the stability of the biocatalyst, given the problems mentioned above, the phosphate buffer was replaced with Tris-HCl. Then, the experimental reaction and storage conditions were varied and the effect on bead features was studied with different techniques to obtain an active, stable, and recyclable biocatalyst.

5.2.2 Materials

Alginic acid sodium salt from brown algae (low viscosity), Horse Liver Alcohol Dehydrogenase (HLADH recombinant, expressed in E. coli, ≥ 0.5U/mg), β-nicotinamide adenine dinucleotide hydrate (NAD^+, grade ≥

96.5%), β-nicotinamide adenine dinucleotide reduced disodium salt hydrate (NADH, grade ≥ 94%), calcium chloride ($CaCl_2$), cyclohexanol (CH-ol) and cyclohexanone (CH-one) were purchased from Merck. Enzyme and substrate were used with no further purification. All other chemicals used were of analytical grade.

5.2.3 Free HLADH activity assay

The catalytic activity of HLADH was evaluated by the oxidation reaction of cyclohexanol to cyclohexanone, which is coupled with the reduction reaction of NAD^+ to NADH. The standard assay was performed in Tris-HCl buffer solution (10 mM, pH 8.0) containing cyclohexanol (20 mM), NAD^+ (1 mM) and HLADH (0.5 mg/ml) at 25 °C. The enzyme activity was measured spectrophotometrically at λ= 340 nm by monitoring the increase in NADH absorbance using the Shimadzu UV-160A instrument; each measurement was repeated at least three times.

5.2.4 Immobilized HLADH activity assay

The beads were prepared using the same procedure described in the previous chapter for the CRL. The catalytic activity of HLADH encapsulated in beads was evaluated by the oxidation reaction of cyclohexanol to cyclohexanone, coupled with the reduction reaction of NAD^+ to NADH, and on the reverse reaction. The operating procedure was adapted from our previous work to this case study[39]. The beads (1.4-1.8 g - 1 mg HLADH), formulation n° 3 ($CaCl_2$ 2%, 30 min) were placed in a thermostated reaction vessel containing 9 ml of a substrate solution in pure Tris-HCl buffer (10 mM, pH 8.0) or with the addition of 2 mM calcium chloride. The substrate concentration was 20 mM and 10 mM in the case of cyclohexanol and

cyclohexanone, respectively. Then, to start the reaction, 1 ml of stock solution of NAD^+ or NADH in Tris-HCl buffer, pH 8.0 was added to the vessel to obtain a final concentration of 0.1 mM and 1 mM, respectively. The reaction was conducted at 25 °C under gentle stirring and monitored spectrophotometrically by measuring the absorbance of NADH at λ=340 nm.

5.2.5 Replacement of phosphate buffer with Tris-HCl

Alginate beads are widely used supports for trapping enzymes, but their poor stability in phosphate buffer solution leads to gradual collapse of the crosslinked structure. In our previous study, excellent recyclability of lipase from *Candida rugosa* immobilized in alginate beads was found, with a relative activity above 80% at the tenth reaction cycle. The reactions were performed in pure water since the enzyme was active even in the absence of a buffer solution, thus avoiding the swelling of the beads and the loss of the enzyme[39]. Unfortunately, HLADH needs a buffer solution to react, and then, to obtain an active and stable biocatalyst over time, the phosphate buffer was replaced with Tris-HCl. Initially, all six bead formulations reported in the previous work were tested, and preliminary recycling tests were conducted to identify the most suitable formulation for this study. The most efficient formulation turned out to be Beads 3, which involves a hardening solution with 2% calcium chloride, and the beads are crosslinked for 30 minutes. The oxidation reaction of cyclohexanol to cyclohexanone and the reverse reduction reaction catalyzed by HLADH trapped in the beads were conducted in 10 mM Tris-HCl buffer at pH 8.0. The progress of the reactions was monitored over time, and the results are shown in Figure 9.

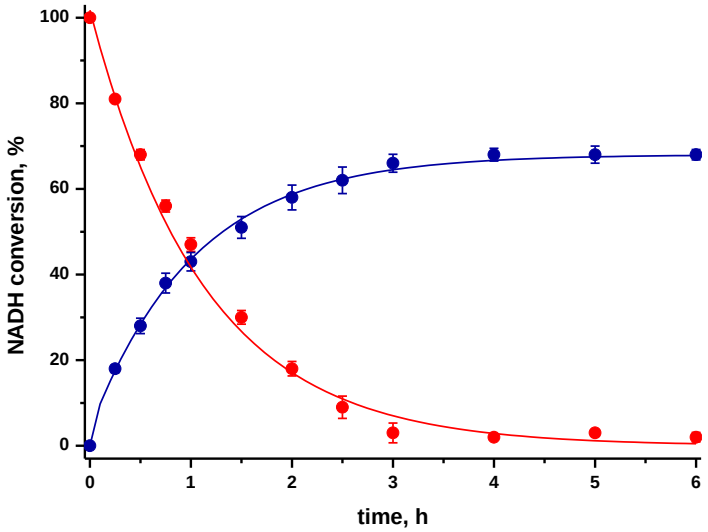

Figure 9: Percentage of conversion of NAD⁺ to NADH (●) in the oxidation reaction of cyclohexanol (CH-ol) and percentage of NADH consumption (●) in the reduction reaction of cyclohexanone (CH-one) as a function of time. Reaction conditions: [CH-ol] = 20 mM, [NAD⁺] = 0.1 mM; [CH-one] = 10 mM, [NADH] = 1 mM; 10 mM Tris-HCl buffer pH = 8.0; T = 25 °C.

The data presented in the figure indicate that the reduction reaction of cyclohexanone is completed after 3 hours, while the maximum conversion of NADH produced in the oxidation of cyclohexanol reaches about 70% and remains constant even with prolonged reaction times (up to 6 hours). These findings suggest a competitive interaction between the oxidized and reduced coenzyme for the enzyme's active site, with the enzyme exhibiting a higher affinity for the reduced form of the cofactor than the oxidized form. Consequently, when the concentration of NADH exceeds that of NAD^+, the enzyme preferentially binds the coenzyme in its reduced form, leading to the cessation of the oxidation reaction. The reaction restarts with the addition of another aliquot of NAD^+ to the reaction vessel after 3 hours but stops again at high NADH concentrations, validating the proposed hypothesis. In any case, a reaction time of 3 hours was selected for the preliminary recycling

tests. The conversion achieved in the first cycle was defined as 100% in both cases, and the relative activity was established as the ratio between HLADH activity at each cycle and the initial activity of HLADH encapsulated in the beads (100%). The recycling stability of the encapsulated HLADH was assessed through a repetitive batch procedure, and the results are depicted in Figure 10.

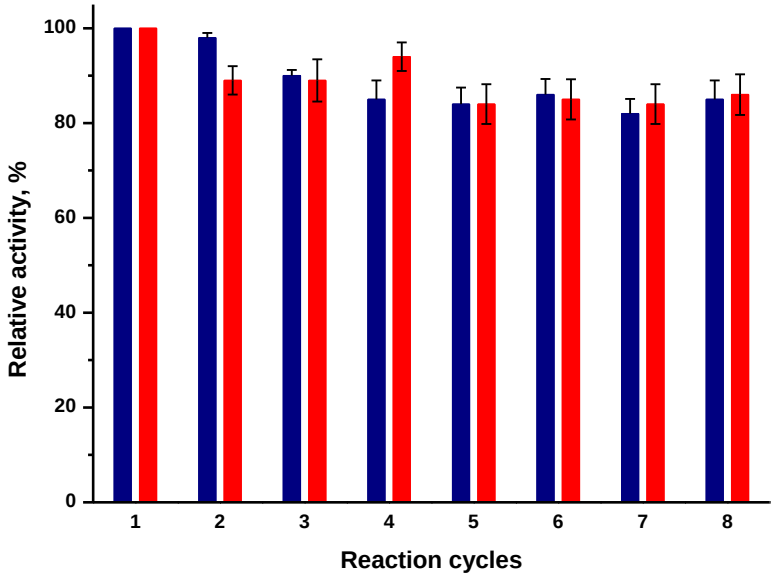

Figure 10: Recycling stability of encapsulated HLADH in oxidation (blue bars) and reduction (red bars) reactions. Storage conditions: 10 mM Tris-HCl buffer pH = 8.0. Reaction conditions: [CH-ol] = 20 mM, [NAD+] = 0.1 mM; [CH-one] = 10 mM, [NADH] = 1 mM; 10 mM Tris-HCl buffer pH = 8.0; T = 25 °C; t = 3h.

The data presented in the figure indicate that both reactions can be repeated for up to eight cycles with a residual activity greater than 80%. However, during the reaction cycles there is a noticeable change in bead size, observable to the naked eye, which ultimately leads to the breakdown of the trapping system after the final cycle. Consequently, despite the selection of a sodium-ion-free buffer system, the phenomenon of swelling to breakage

persists, resulting in a reduction of the crosslinking agent within the system and the subsequent collapse of the alginate gel network. To counteract the depletion of Ca^{2+} ions from the beads, we chose to reintroduce calcium ions into the biocatalyst by incorporating calcium chloride into both the reaction and storage solutions. Numerous experiments were then conducted to assess the impact of calcium ion concentration on the properties of the immobilization system, with the aim to identify the optimal concentration. The results of all experiments conducted to optimize the encapsulation system are detailed below.

5.2.6 Characterization of Ca-alginate beads properties

To obtain information on the structure of the beads as a function of Ca^{2+} concentration, among the different techniques used for this purpose, we have selected gravimetry, calorimetry, optical and electron microscopy, and EDS microanalysis. In particular, the analyzes were carried out on spheres subjected to three "simulated" cycles for 2 days in Tris-HCl buffer or in buffer added with different concentrations of $CaCl_2$ and then stored overnight in the same solution.

Gravimetry

The evaluation of swelling behavior is crucial for assessing the stability and lifespan of alginate hydrogel systems. This characteristic property can compromise mechanical strength, thermal stability, and recycling efficiency. Consequently, addressing this phenomenon becomes particularly challenging, especially when the encapsulation system is employed for enzyme recycling. To tackle this challenge, gravimetric measurements were conducted to determine the optimal concentration of $CaCl_2$ to add to both the reaction and storage solutions. This addition aimed at maintaining the

stability of the beads' weight over time. In particular, the freshly prepared calcium alginate beads were weighed (W_i) and then immersed in a pure Tris-HCl buffer solution (10 mM, pH 8.0) or added with calcium chloride (1 ÷ 100 mM). The beads were kept at room temperature under magnetic stirring. At certain time intervals, the beads were washed, filtered, and weighed again (W_n) before being reintroduced into the buffer solution. This operating procedure allows to simulate the reaction cycles of the beads during the recycling tests. The degree of swelling (S_w) was calculated with the following equation (eq. 1)[40].

$$S_w(\%) = \frac{W_n - W_i}{W_i} \times 100 \qquad (1)$$

The change in weight over time as a function of calcium ion concentration is shown in Figure 11A.

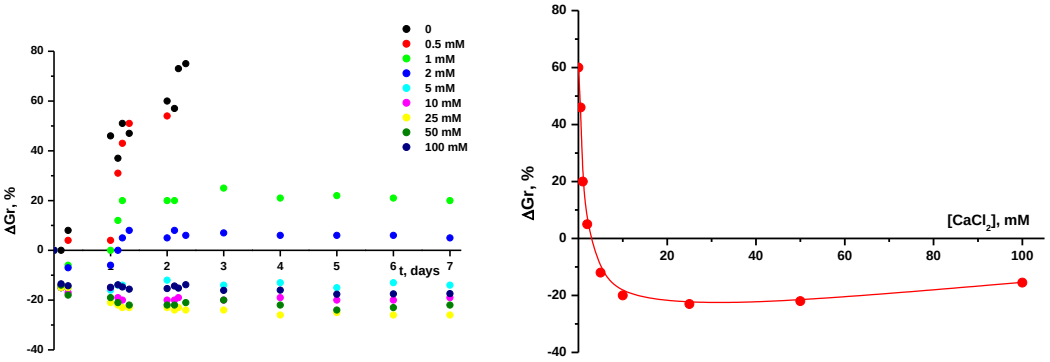

Figure 11: (A) Variation of the weight percentage over time of the beads placed in Tris-HCl buffer in the absence and in the presence of different calcium ion concentrations both in the reaction and in the storage solutions. (B) Percentage change in weight of each set of beads at 48 h as a function of the calcium chloride concentration added to Tris-HCl buffer.

In Fig. 9A, it is evident that, in the absence or presence of low Ca^{2+} concentrations (*i.e.*, 0.5 mM), the beads increase in weight and break down

after two days. Conversely, with higher concentrations of calcium ions, the beads exhibit either an increase or decrease in weight during the initial two days, followed by a stable weight over time. The 48-hour limit appears to be the time required for the system stabilization. Figure 11B presents the percent weight change (ΔGr, %) of various sets at 48 hours, correlating with the concentration of calcium chloride added to the Tris-HCl buffer. The influence of Ca^{2+} concentration on bead weight is evident, and conditions facilitating minimal change in the initial weight require a buffer solution containing 2 mM $CaCl_2$. Specifically, at low calcium ion concentrations, the beads swell, while concentrations exceeding 2 mM cause shrinkage. Above 10 mM $CaCl_2$, the beads undergo approximately a 20% reduction in their initial weight. Table 3, column 1, provides a comprehensive overview of all weight percentage changes (ΔGr, %) obtained from gravimetric measurements, relative to freshly prepared beads used as a reference.

Table 3: Effect of $CaCl_2$ concentration on some structural features of alginate beads subjected to three simulated cycles and stored in Tris-HCl buffer pure or added with $CaCl_2$.

[$CaCl_2$], mM	ΔGr, %	H_2O,%	V, mm^3
–	+60	94	23.2
1	+20	84	16.5
2	+5	83	11.2
10	-20	79	10.4
25	-20	77	10.8
100	-16	74	10.1
freshly prepared	–	80	9.0

Calorimetric measurements

The quantification of water content within the beads was carried out by thermal analysis using a Mettler Toledo DSC 3 differential scanning calorimeter. The individual samples, approximately 10 mg each, were placed in 40 µl aluminum pans and weighed before insertion into the thermal chamber. Measurements were conducted in the temperature range of -50 °C to +200 °C with a heating rate of 10 °C/min. DSC scans were executed in a nitrogen atmosphere with a flow rate of 50 ml/min. For each sample, the latent heat of the melting process was compared to that of pure water (333.5 J/g) to determine the percentage of water content within the beads. All thermograms exhibit a pronounced broad endothermic peak between -5 and +10 °C, corresponding to the transition of water from the solid to the liquid state. The percentages of water inside the beads, depending on $CaCl_2$ concentration in both reaction and storage solutions after 48 hours, are detailed in Table 3, column 2. The quantity of water inside the beads diminishes with increasing $CaCl_2$ concentration. Specifically, the percentage of H_2O in pure buffer and in the presence of 100 mM $CaCl_2$ is 94% and 74%, respectively. In the remaining beads, this percentage is quite similar, ranging from 77 to 84%. The water content in freshly prepared beads is 80%, a value closely aligned with beads stored with 1 to 25 mM $CaCl_2$, maintaining constancy over time, exceeding 48 hours.

Optical Microscopy

Stereomicroscope measurements, which allow the determination of bead structure, including shape, size, and sphericity, were conducted on 25 beads per sample due to their relatively uniform dimensions (CV < 5%). The

instrument utilized and the formulas for calculating the dimensional parameters of the beads are reported in Chapter 4, paragraph 4.1.3.

The images of all bead set are depicted in Figure 12.

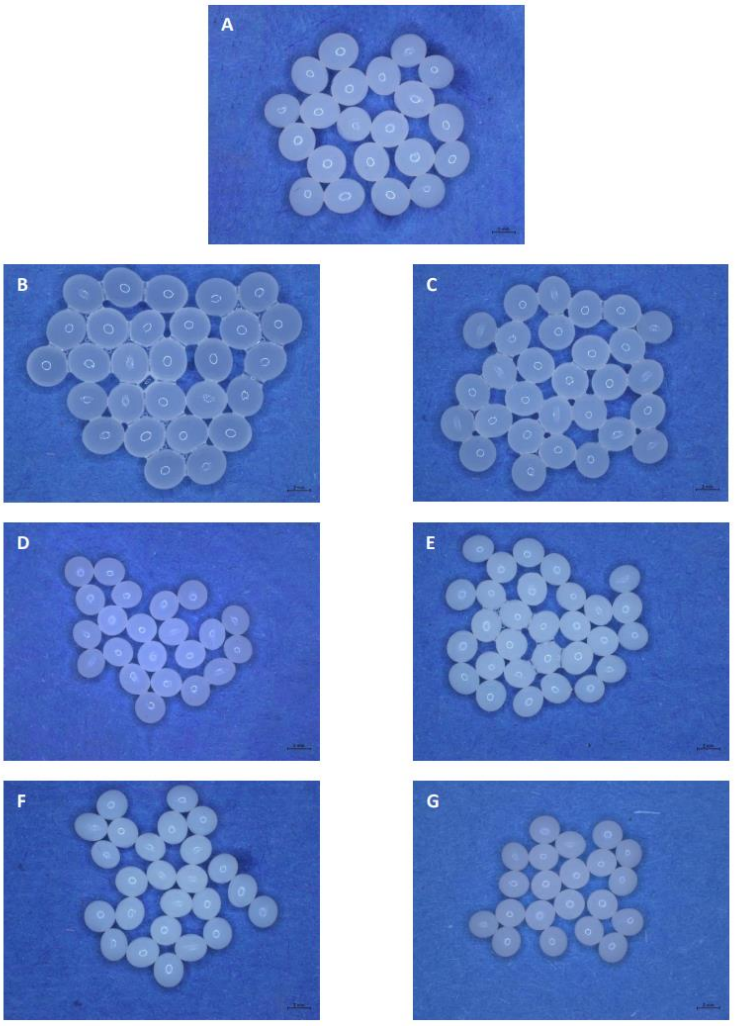

Figure 12: Stereomicroscope images at 4x magnification of freshly prepared beads (A), beads stored in pure Tris-HCl buffer (B), and beads stored in buffer added with 1 mM (C), 2 mM (D), 10 mM (E), 25 mM (F) and 100 mM (G) $CaCl_2$

The beads subjected to three "simulated" cycles for 2 days and subsequently stored in Tris-HCl buffer with added Ca^{2+} ions exhibit larger dimensions than

the freshly prepared beads, regardless of $CaCl_2$ concentration. Specifically, the size of beads stored without Ca^{2+} ions or with 1 mM $CaCl_2$ is approximately 40% and 25% greater than freshly prepared ones, respectively. In contrast, the difference with all other samples is about 10% or less. All beads are slightly ellipsoidal, except those stored in the presence of 2 mM $CaCl_2$, with a sphericity factor less than 0.05. The shape of these beads, measured after a week, remains nearly unchanged, supporting the observation that the system achieves stability after two days, as corroborated by gravimetric tests. Although the aspect ratio of all beads is close to unity, typical of a sphere, it's worth noting that this parameter provides a good description in case of large deformations but is less sensitive to small distortions than the sphericity factor[41]. The average volume of the beads was calculated using equation 5 (see Experimental section), and the values obtained are presented in Table 3, column 3. As anticipated, the volume of the beads stored in pure Tris-HCl buffer and with the lowest $CaCl_2$ concentration is 2.6 and 1.8 times higher, than freshly prepared beads, respectively. For the other formulations, however, an increase in volume of 10-20% is observed. The analysis of the data collected shows an evident correlation between the percentage of water inside the beads, their volume, and the change in weight variation. The increase in weight corresponds to an increase in both the percentage of water within the beads and their volume, demonstrating a linear relationship ($R^2 > 0.92$) (Figure 13).

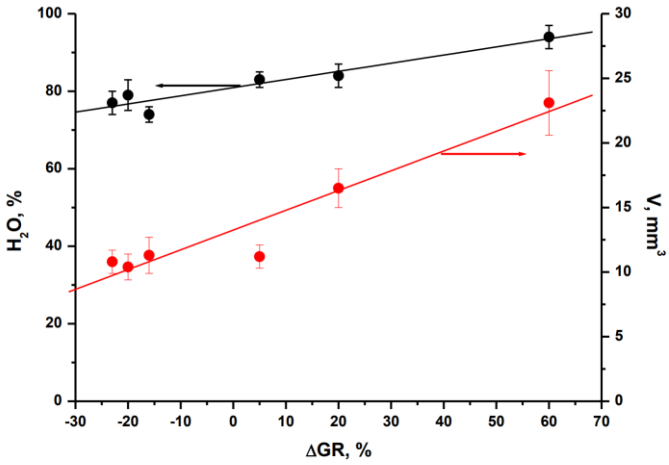

Figure 13: Correlation between the percentage of water inside the beads (●) and their volume (●) as a function of the weight variation.

SEM-EDS

The external and internal microstructures of the hydrated beads were examined using a scanning electron microscope (SEM) equipped with a Peltier cooling device, allowing investigations under conditions closely resembling those used for catalytic tests[42]. For these experiments, four formulations were chosen: beads subjected to three "simulated" cycles for 2 days in pure Tris-HCl buffer or in buffer containing 2 or 100 mM $CaCl_2$, followed by overnight storage in the same type of solution, and freshly prepared beads used as reference. SEM images were acquired at 26× magnification to examine the morphology of both external and internal surfaces, and at 300× magnification to emphasize the different internal compactness of the selected beads. As depicted in Figure 14, images of the external surface at lower magnification enable the visualization of the entire bead structure and confirm the size discrepancies observed in stereomicroscope investigations. The cross-sectional analysis at both magnifications reveals that the internal compactness of the beads is strongly

influenced not only by the presence of calcium ions but also by their concentration. In pure Tris-HCl buffer, the internal structure of the bead appears more porous than that of the freshly prepared bead, displaying numerous wide voids of different sizes (Figure 14B). The addition of Ca^{2+} to the buffer solution results in a more homogeneous matrix, with compactness increasing as the Ca^{2+} concentration rises. Specifically, with 2 mM $CaCl_2$ present in both reaction and storage solutions, the internal structure, though more compact, exhibits cavities similar to those of the reference bead (Figure 14C). These cavities disappear completely at high Ca^{2+}. concentrations Indeed, the beads treated with 100 mM $CaCl_2$ exhibit a highly compact and homogeneous structure (Figure 14D).

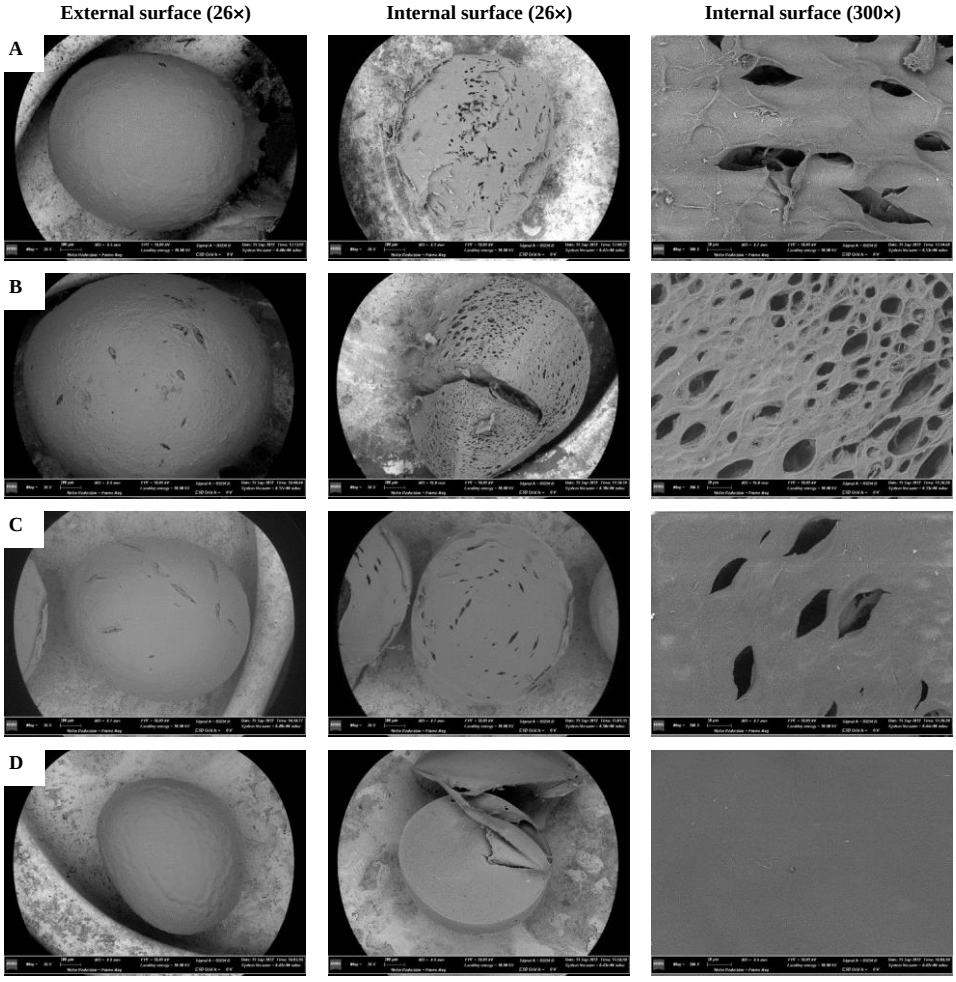

Figure 14: SEM images at 26x magnification of the external structure and at 26x and 300x magnifications of the internal structure of freshly prepared beads (A), stored in pure Tris-HCl buffer (B), stored in Tris-HCl buffer plus 2 mM (C) and 100 mM Ca^{2+} (D).

SEM/EDS analyses were performed with of Zeiss GeminiSEM 500 equipped with an EDS OXFORD Aztec Energy with INCA X-ACT detector with a working distance of about 8 mm and high voltage of 10 KeV.

The measurements were conducted in triplicate on both the reference samples and the three previously examined beads to quantify the amount of

calcium on the external surface of dried samples. An area of approximately 350 × 250 μm² was selected. The weight percentages of the most abundant elements, as depicted in Table 4, reveal that the Ca/C ratio increases as calcium ions are introduced into the Tris-HCl buffer, with variations depending on its concentration. Notably, the Ca/C value with 2 mM Ca^{2+} closely resembles that of the reference, indicating once again that this formulation enables the beads to maintain their initial structural features.

Table 4: Mean values of weight percentages of the most abundant elements obtained from EDS analysis carried out on dried beads.

	Wt (%)			
Element	Reference	Tris-HCl	Ca^{2+} 2 mM in Tris-HCl	Ca^{2+} 100 mM in Tris-HCl
C	43±1.5	44±0.5	42±1.1	38±0.6
O	50±0.8	49±1.0	49±0.4	42±0.7
Ca	8±0.9	7±0.5	8±0.7	12±0.8
Cl	-	1±0.3	1±0.2	8±0.4
Ratio Ca/C	0.19	0.15	0.20	0.31

5.2.7 Reusability and storage stability of immobilized HLADH

To reduce the cost of large-scale applications, enzyme reusability is one of the most important issues. The main cause of inactivation in multimeric enzymes is subunit dissociation, prompting the development of various immobilization strategies to counteract this issue[43]. Numerous studies in the literature have explored the recyclability of YADH when immobilized on solid supports through covalent bonds[44–48] or encapsulated in hybrid beads[31,49]. Conversely, as noted previously, the literature has only sparingly

addressed immobilized HLADH. Notably, His-tagged HLADH covalently immobilized onto a metal-derivatized epoxy resin exhibited enhanced enantioselectivity and considerable reusability in the reduction of aliphatic and aromatic aldehydes[37]. Although the results presented above underscore the necessity of adding 2 mM Ca^{2+} to the buffer solution to maintain the structural integrity of the beads over time, they do not provide information on the preservation of enzyme activity within the beads. Therefore, the recycling stability of HLADH encapsulated in calcium-alginate beads was investigated through a repetitive batch procedure under the same conditions described in the section 4.3.3. After each cycle, the biocatalyst was filtered, rinsed thoroughly with water, and then reintroduced into a fresh reaction medium for a subsequent cycle or stored at 4 °C, in pure buffer or in buffer supplemented with 2 mM calcium chloride. Subsequent activity measurements were conducted and normalized by comparing them to the enzyme activity in the initial reaction cycle, defined as 100% activity. To examine the storage stability of immobilized HLADH, its activity was assessed after a 30-day incubation at 4 °C in Tris-HCl buffer containing 2 mM Ca^{2+}. Figure 15 illustrates the relative enzyme activity obtained after each 3-hour reaction cycle, defined as the ratio of the enzyme activity after

each reaction cycle to that determined in the initial reaction cycle, set to 100%.

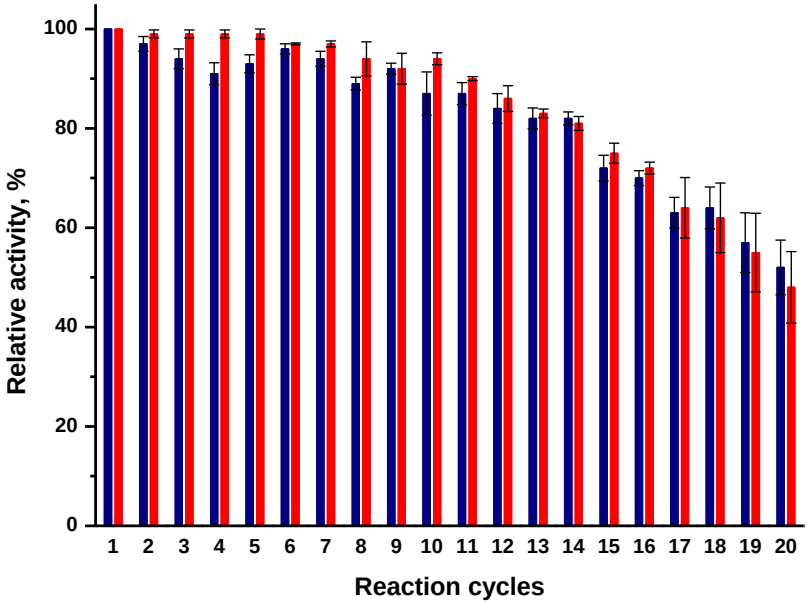

Figure 15: Recycling stability of encapsulated HLADH in oxidation (blue bar) and reduction (red bars) reactions. Storage conditions: 10mM Tris-HCl buffer pH=8.0 added with 2 mM $CaCl_2$. Reaction conditions: [CH-ol]=20mM, [NAD^+]=0.1mM; [CH-one]=10mM, [NADH]=1 mM; 10mM Tris-HCl buffer pH=8.0 added with 2 mM $CaCl_2$; T=25°C; t=3 h.

As depicted in the figure, the biocatalyst maintains more than 80% of its initial activity for the fourteenth cycles. Subsequently, the relative activity gradually diminishes to 52% and 48% for the oxidation and reduction reactions, respectively, by the twentieth cycle. However, following the last cycle, the relative activity reaches 100% after 8 hours of reaction time. This suggests that the enzyme inside the beads remains active, albeit requiring additional time to achieve performance comparable to the initial cycle.

The storage stability of HLADH was also assessed by incubating the enzyme in a Tris-HCl buffer solution supplemented with 2 mM $CaCl_2$ at 4 °C. After

30 days of storage, the retention of enzyme activity was 100%, compared to the activity measured after the initial incubation. Hence, the addition of Ca^{2+} to the buffer solution significantly enhances both the recycling and storage stability of the biocatalyst. This indicates that the experimental conditions employed to preserve the characteristics of freshly prepared beads actually allow the enzyme to maintain its catalytic activity for a prolonged period.

5.2.8 Thermal stability

A crucial property in biocatalysis for practical applications is the resistance of enzymes to thermal inactivation. This is particularly important since high temperatures are often required to enhance substrate solubility for industrial biotransformations. Studies have suggested that the increased thermostability observed in certain thermophilic ADHs may be attributed to a greater content of proline residues at specific positions, associated with a higher coil/loop percentage[50]. Notably, HLADH exhibits superior thermal stability compared to YADH, despite both being mesophilic enzymes. This increased stability is attributed to a greater number of Pro residues (20 vs. 13), contributing to increased rigidity, structural compactness, and reduced flexibility. These characteristics enable HLADH to maintain its active conformation even at higher temperatures[51]. Additionally, HLADH denaturation has been observed to begin above 45 °C, with dimer dissociation into two subunits at 46 °C, followed by aggregate formations as the temperature rises to 49 °C[52]. Thermal stability of free and immobilized HLADH was determined by storing the enzymes at various temperatures (40, 50, 60 and 70 °C) for different times, from 10 minutes to 24 hours. After the incubation period, the residual activity was evaluated as previously described in Sections 4.3.2 and 4.3.3. The thermal denaturation kinetics of HLADH was

estimated by a first-order exponential equation, and the thermal denaturation constants (k_d, h^{-1}) were calculated by plotting the logarithm of the ratio of the activity after incubation (A) to the initial activity (A_0) versus incubation time (t) (eq. 2)[49].

$$\mathrm{Ln}(A/A_0) = -k_d \times t \qquad (2)$$

The half-life ($t_{1/2}$) value for HADH thermal denaturation was calculated according to eq. 3.

$$t_{1/2} = \ln(2/k_d) \qquad (3)$$

The activation energy (E_d) for thermally denaturing HADH was calculated based on the Arrhenius equation (eq. 4)

$$k_d = c \times e^{-E_d/RT} \qquad (4)$$

where c was the pre-exponential constant, R was the gas constant (8.314 J/mol·K) and T (K) the incubation temperature. Specifically, E_d was extrapolated from the graph of the logarithm of the denaturation rate constant (ln k_d) as a function of the reciprocal of the incubation temperature (1/T).

Finally change in enthalpy (ΔH^0, KJ/mol), free energy (ΔG^0, KJ/mol) and entropy (ΔS^0, KJ/mol·K) for thermal denaturation of HLADH was calculated as follows (eqs. 5, 6, 7)[53].

$$\Delta H^0 = E_d - RT \qquad (5)$$

$$\Delta G^0 = -RTln\left(\frac{k_d \times h}{k_B \times h}\right) \qquad (6)$$

$$\Delta S^0 = \frac{\Delta H^0 - \Delta G^0}{T} \qquad (7)$$

where E_d is the activation energy for thermal denaturation, T is the absolute temperature, R is the gas constant, k_d is the deactivation rate constant (h^{-1}) kB is the Boltzmann constant (1.38×10^{-23} J/K), and h is the Planck constant (1.84×10^{-37}J·h).

Figure 16 shows the time trend of the residual activity, reported as the ratio between the HLADH activity after incubation and the activity at time zero, taken as 100%.

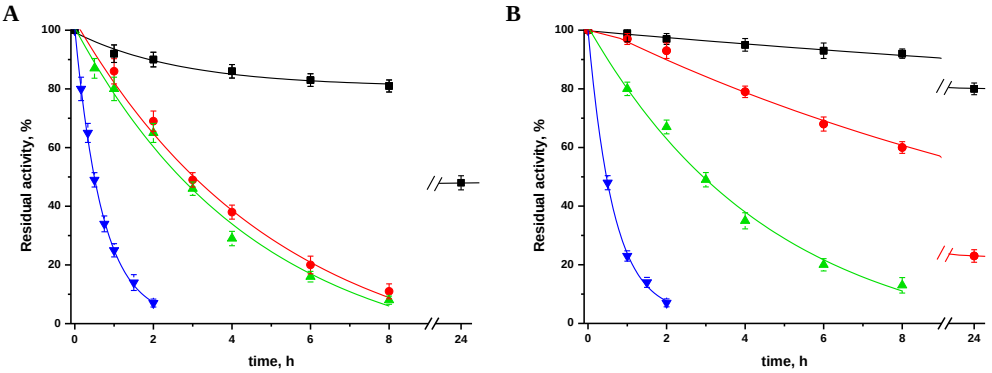

Figure 16: Thermostability of free (A) and immobilized (B) HLADH in Tris-HCl buffer, pH 8.0 added with 2 mM $CaCl_2$ at 40 (■), 50 (■), 60 (▲) and 70 °C (▼).

The results obtained with free HLADH (Figure 16A) showed that it is quite stable at 40 °C, its residual activity being equal to 80% after 8 h and then decreasing to about 50% after 24 h. However, a further increase in temperature leads to rapid deactivation, very similar at 50 and 60 °C and much faster at 70 °C. The enzyme immobilized in alginate beads (Figure 16B) has a higher relative activity than the free form at both 40 and 50 °C, but this stabilizing effect disappears at higher temperatures and the time trends are very similar. This outcome can be explained by assuming that at 50 °C the free enzyme exists in an aggregate state and the deactivation rate does not change significantly by increasing the temperature by another 10 °C. On the other hand, encapsulation of HLADH in alginate beads prevents the

formation of aggregates at least at 50 °C; at higher temperatures, other deactivation mechanisms may be involved. The data reported in the figure, however, do not take into account the differences in reaction rates at each temperature between the free and immobilized enzyme before incubation. Indeed, the slower diffusion of both the substrate and the coenzyme inside the beads causes a decrease in the reaction rate of about 50-60% than the free form at all temperatures, except at 50°C, where the decrease is by 30%. Thermal denaturation constants (k_d) and half-life ($t_{1/2}$), for HLADH, calculated by using a first-order deactivation model, along with the thermodynamic parameters (eqs. 16-18) are listed in Table 3.

Table 5: Deactivation constant (k_d), half-life ($t_{1/2}$) and change in enthalpy (ΔH^0), entropy (ΔS^0) and Gibbs free energy (ΔG^0) for the thermal denaturation of free and immobilized HLADH.

			free		
T(°C)	k_d (h^{-1})	$t_{1/2}$(h)	ΔH^0 (kJ/mole)	ΔS^0 (kJ/moleK)	ΔG^0 (kJ/mole)
40	0.03	22.5	99.79	-0.08	125.19
50	0.26	2.7	99.70	-0.07	123.48
60	0.31	2.2	99.62	-0.08	126.90
70	1.34	0.5	99.54	-0.08	126.62
			immobilized		
40	0.01	73.0	142.72	0.05	128.05
50	0.06	11.1	142.63	0.05	127.42
60	0.26	2.7	142.55	0.05	127.39
70	1.34	0.5	142.47	0.05	126.62

Compared to free HLADH, the encapsulated enzyme shows a lower k_d value and a higher $t_{1/2}$ value at the same incubating temperature up to 70 °C, where the same values are obtained. More precisely, the half-life of immobilized HLADH is three and more than four times higher than that of the free enzyme at 40 and 50 °C, respectively, while at 60 °C an increase of only 20% is obtained. In a previous study, the deactivation rate constants of free and

covalently immobilized HLADH on CNBr-Sepharose performed at 60 °C were 0.0064 and 0.0039 min^{-1}, respectively[53], values very similar to those of this work.

The enthalpy change, ΔH^0, is often used to determine the energy required to inactivate or denature the enzyme. In the case of the free and encapsulated enzymes, the ΔH^0 values both decrease as the temperature increases. This means that less energy is required to inactivate the enzyme at higher temperatures. This can be attributed to the fact that at higher temperatures the enzyme is more likely to undergo thermal denaturation, which requires less energy to occur. However, at the same temperature, the ΔH^0 value of the encapsulated enzyme is always higher than the free form. This indicates that encapsulation increases the thermal stability of the enzyme, since the immobilized biocatalyst is more stable due to the physical and chemical interactions established with the matrix, which can prevent or slow down denaturation processes[54].

Another parameter that allows to better understand the thermal deactivation process is the entropy. The entropy changes for a process can provide information about the level of disorder or randomness in the system. A negative entropy change for the free enzyme indicates that it has become more ordered, which can occur when aggregation processes take place[53]. Indeed, in our case study for the free enzyme the entropy of the deactivation process, ΔS^0, has negative values, thus contributing positively to the enzyme stabilization. Unlike the free enzyme, the activation entropy for the immobilized form is always positive, in part because the aggregation processes are not possible or at least more improbable and furthermore a misfolding of the enzyme structure may occur caused by interactions with the matrix.

Through the combination of these thermodynamic functions, ΔH^0 and ΔS^0, the variation in Gibbs free energy can be better explained. A high value of thermal denaturation free energy indicates that the protein is more stable and less likely to denature at a particular temperature, indicating its resistance to thermal unfolding. Therefore, the free energy of thermal denaturation is an important parameter for understanding the stability of enzymes under different conditions, including high-temperature environments[55]. For the immobilized biocatalyst, the positivity of ΔS^0 is counteracted by the contribution to stabilization due to enthalpy up to 50 °C, but at higher temperatures, the entropy term ($T\Delta S^0$) becomes predominant and thus negatively affects the thermal resistance of the encapsulating enzyme. Therefore, the ΔG^0 values are significantly higher for the encapsulated enzyme at lower temperatures, but decrease rapidly to achieve the same value of the free enzyme at 70 °C.

5.2.9 Conclusion

This study presents a straightforward method for encapsulating Horse Liver Alcohol Dehydrogenase into calcium-alginate beads. A key strategy to prevent bead swelling and breakage involves reintroducing calcium ions into the biocatalyst, effectively addressing the loss of the crosslinking agent responsible for these issues. The impact of Ca^{2+} addition on bead structure, explored through various techniques, has facilitated the identification of the optimal calcium chloride concentration for both reaction and storage solutions. The optimized biocatalyst demonstrates significant enhancements in recycling and both storage and thermal stability.

References

1 K. Dalziel, H. Dam, M. Moutschen-Dahmen, B. Noer and L. Reio, *Acta Chem Scand*, 1957, **11**, 1706–1723.

2 H. Theorell and B. Chance, *Acta Chem Scand*, 1951, **5**, 127–1144.

3 K. Dalziel, *Acta Chem Scand*, 1963, **17**, 27–33.

4 B. V. Plapp, *Arch Biochem Biophys*, 2010, **493**, 3–12.

5 K. Dalziel and F. M. Dickinson, *Biochem J*, 1966, **100**, 34–46.

6 F. M. Dickinson and K. Dalziel, *Biochem J*, 1967, **104**, 165–172.

7 V. C. Sekhar and B. V. Plapp, *Biochemistry*, 1990, **29**, 4289–4295.

8 K. Dalziel and F. M. Dickinson, *Biochem J*, 1966, **100**, 491–500.

9 B. V. Plapp and R. Subramanian, *Arch Biochem Biophys*, 2021, **701**, 108825.

10 G. L. Shearer, K. Kim, K. M. Lee, C. K. Wang and B. V Plapp, 1993, **32**, 11186–11194.

11 D. S. Sigman, *Journal of Biological Chemistry*, 1967, **242**, 3815–3824.

12 S. N. Chanquia, L. Huang, G. G. Liñares, P. D. de María and S. Kara, *Catalysts*, 2020, **10**, 1–8.

13 T. Itozawa and H. Kise, *Bull Chem Soc Jpn*, 1994, **67**, 3304–3308.

14 R. A. Kemper and A. A. Elfarra, *Chem Res Toxicol*, 1996, **9**, 1127–1134.

15 C. D. Dithugoe, J. van Marwijk, M. S. Smit and D. J. Opperman, *ChemBioChem*, 2019, **20**, 96–102.

16 N. Wen, W. Liu, Y. Hou and Z. Zhao, *Appl Biochem Biotechnol*, 2013, **170**, 370–380.

17 D. Giacomini, P. Galletti, A. Quintavalla, G. Gucciardo and F. Paradisi, *Chemical Communications*, 2007, **39**, 4038–4040.

18 H. Jørnvall, *Eur J Biochem*, 1970, **16**, 25–40.

19 M. Andersson and P. Adlercreutz, *Biotechnology Techniques*, 1999, **13**, 903–907.

20 A. Irwin, K. P. Lok, K. W. Huang and B. J. Jones, *Journal of Chemical Society, Perkin Transactions 1*, 1978, **12**, 1636–1642.

21 R. Pietriszico, K. Crawford and D. Lester, *Arch Biochem Biophys*, 1973, **159**, 50–60.

22 O. Trott and A. J. Olson, *J Comput Chem*, 2010, **31**, 455–461.

23 G. Colombo, *Curr Opin Struct Biol*, 2023, **83**, 102702.

24 A. Triveri, C. Sanchez-Martin, L. Torielli, S. A. Serapian, F. Marchetti, G. D'Acerno, V. Pirota, M. Castelli, E. Moroni, M. Ferraro, P. Quadrelli, A. Rasola and G. Colombo, *J Mol Biol*, 2022, **434**, 167468.

25 F. Chen, P. Wang, Y. An, J. Huang and Y. Xu, *Biochimie*, 2014, **108**, 33–39.

26 S. Aslam, A. Ali, · Muhammad Asgher, N. Farah, · Hafiz, M. N. Iqbal, · Muhammad Bilal and M. Bilal, *Catal Letters*, 2022, **152**, 1729–1741.

27 M. M. M. Elnashar, E. N. Danial and G. E. A. Awad, *Ind Eng Chem Res*, 2009, **48**, 9781–9785.

28 S. K. Bajpai and S. Sharma, *React Funct Polym*, 2004, **59**, 129–140.

29 L. De Matteis, R. Germani, M. V. Mancini, F. Di Renzo and N. Spreti, *Appl Catal A Gen*, 2015, **492**, 23–30.

30 S. W. Xu, Z. Y. Jiang, Y. Lu, H. Wu and W. K. Yuan, *Ind Eng Chem Res*, 2006, **45**, 511–517.

31 Z. de Zhou, G. yin Li and Y. jian Li, *Int J Biol Macromol*, 2010, **47**, 21–26.

32 A. Ahmad, N. M. Mubarak, F. T. Jannat, T. Ashfaq, C. Santulli, M. Rizwan, A. Najda, M. Bin-Jumah, M. M. Abdel-Daim, S. Hussain and S. Ali, *processes*, 2021, **9**, 137.

33 T. Itozawa and H. Kise, *J Ferment Bioeng*, 1995, **80**, 30–34.

34 S. Parida, R. Datta and J. S. Dordick, *Appl Biochem Biotechnol*, 1992, **33**, 1–14.

35 J. M. Bolivar, L. Wilson, S. A. Ferrarotti, J. M. Guisán, R. Fernández-Lafuente and C. Mateo, *J Biotechnol*, 2006, **125**, 85–94.

36 G. A. Petkova, K. Záruba and V. Král, *Biochimica et Biophysica Acta (BBA) - Proteins and Proteomics*, 2012, **1824**, 792–801.

37 D. Quaglia, M. Pori, P. Galletti, E. Emer, F. Paradisi and D. Giacomini, *Process Biochemistry*, 2013, **48**, 810–818.

38 B. Ngamsom, A. M. Hickey, G. M. Greenway, J. A. Littlechild, T. McCreedy, P. Watts and C. Wiles, *Org Biomol Chem*, 2010, **8**, 2419–2424.

39 A. Vetrano, F. Gabriele, R. Germani and N. Spreti, *New Journal of Chemistry*, 2022, **46**, 10037–10047.

40 Y. Hu, T. Chen, X. Dong and Z. Mei, *Polymer Bulletin*, 2015, **72**, 2857–2869.

41 E. S. Chan, B. B. Lee, P. Ravindra and D. Poncelet, *J Colloid Interface Sci*, 2009, **338**, 63–72.

42 A. Wassilkowska and T. Woźniakiewicz, *Solid State Phenomena*, 2015, **231**, 139–144.

43 R. C. Rodrigues, Á. Berenguer-Murcia, D. Carballares, R. Morellon-Sterling and R. Fernandez-Lafuente, *Biotechnol Adv*, 2021, **52**, 107821.

44 S. Ghannadi, H. Abdizadeh, M. Miroliaei and A. A. Saboury, *Ind Eng Chem Res*, 2019, **58**, 9844–9854.

45 G.-Y. Li, Z.-D. Zhou, Y.-J. Li, K.-L. Huang and M. Zhong, *J Magn Magn Mater*, 2010, **322**, 3862–3868.

46 C. Ottone, C. Bernal, N. Serna, A. Illanes and L. Wilson, *Appl Microbiol Biotechnol*, 2018, **102**, 237–247.

47 G. Pietricola, M. Dosa, C. Ottone, D. Fino, M. Piumetti and T. Tommasi, *Waste Biomass Valorization*, 2022, **13**, 4043–4055.

48 K. Vasić, Ž. Knez and M. Leitgeb, *Sci Rep*, 2020, **10**, 19478.

49 P. Han, X. Song, H. Wu, Z. Jiang, J. Shi, X. Wang, W. Zhang and Q. Ai, *Ind Eng Chem Res*, 2015, **54**, 597–604.

50 A. Vitale, N. Thorne, S. Lovell, K. P. Battaile, X. Hu, M. Shen, S. D'Auria and D. S. Auld, *PLoS One*, 2013, **8**, e63828.

51 A. Barzegar, A. A. Moosavi-Movahedi, J. Z. Pedersen and M. Miroliaei, *Enzyme Microb Technol*, 2009, **45**, 73–79.

52 F. Moosavi-Movahedi, A. A. Saboury, H. H. Alijanvand, M. Bohlooli, M. Salami and A. A. Moosavi-Movahedi, *Int J Biol Macromol*, 2013, **58**, 66–72.

53 A. Pal and F. Khanum, *Process Biochemistry*, 2011, **46**, 1315–1322.

54 E. Marín, L. Sánchez, M. D. Pérez, P. Puyol and M. Calvo, *J Food Sci*, 2003, **68**, 89–93.

55 A. Tanaka and E. Hoshino, *Biochemical Journal*, 2002, **364**, 635–639.

Addendum

Cultural Heritage

A.1 The Role of Water

The significance of stone cultural heritage lies in its historical, architectural, and cultural value. Stones have been fundamental to the construction of numerous iconic structures, monuments, sculptures, and archaeological sites worldwide, serving as a testament to human craftsmanship, ingenuity, and societal development in different eras. Stone cultural heritage not only reflects the architectural and artistic achievements of past civilizations but also embodies cultural identity, traditions, and beliefs. These structures often hold historical narratives, stories, and knowledge that contribute to our understanding of ancient civilizations and their ways of life. Preserving stone cultural heritage is vital for maintaining our connection with the past, fostering cultural appreciation, and providing educational insights into human history and evolution. Furthermore, it serves as a source of inspiration and admiration for future generations, emphasizing the need for conservation efforts to protect these invaluable treasures for posterity.

Water assumes a pivotal role in the deterioration process of stones due to its ability to infiltrate the porous structure, causing harm through freezing-thawing or wetting-drying cycles. Additionally, it acts as a carrier for soluble salts that permeate the stone, leading to crystallization. This process triggers the development of efflorescence, generating mechanical stress and ultimately impacting the long-term durability of the material. Typically, porous materials exhibiting high open porosity and interconnected pores are more susceptible to significant damage. This susceptibility arises from

water facilitating the migration, entrapment, and partial dissolution of contaminants within the inner regions of the porous medium. Moreover, water contributes to the formation of biological patinas, especially in environments characterized by elevated humidity levels and exposure to light. Under these conditions, microorganisms thrive on stone surfaces, instigating the biodegradation of the stone[1–3]. Further structural damages can occur mainly either due to a thermal stress, i.e., when different surface portions of the same artifact are simultaneously affected by different temperatures, or when they are constituted of heterogeneous materials with different thermal expansion coefficients.

Therefore, the first study concerns the development and optimization of two hydrogels containing biocidal agents for the removal of biofilms from Lecce stone samples. Meanwhile, the second study focuses on prevention, specifically the application of hydrophobic agents to avoid undesired effects caused by water penetration into stones cultural heritage.

A.2 Alginate-biocide hydrogels against stone biodeterioration

One of the main problems encountered during the removal processes of microorganisms is represented by the concomitant presence of several species that can form the biological patina. In this sense, chemical treatments involving widespread biocides can be applied to counteract the proliferation of biocontaminants. As reported by Faimon et al.[4] oxidant species such as hydrogen peroxide and sodium hypochlorite are low cost and powerful biocides capable of effectively eradicate the most common microbial species, degrading the organic matter of which they are composed through the reaction represented below:

$$(CH_2O)_n + 2nOX \rightarrow nCO_2 + nH_2O + 2nRED$$

where $(CH_2O)_n$ is a hypothetical form of organic matter and OX is an oxidant species capable of transferring one electron reducing itself to the RED species. Although these chemicals exhibit strong biocidal properties, they can pose significant risks to the surface of the substrate, the health of operators, and the environment[5]. Specifically, when these biocides are administered in an aqueous solution, some residual by-products persist on surfaces, causing deteriorative effects like salt efflorescence or corrosion of the artifact's surface[6]. In recent years, various research groups have focused on enhancing traditional chemical treatments by encapsulating them within various types of inert matrices, both organic and inorganic. This research aligns with the ongoing investigation in the field, focusing on the encapsulation of two distinct biocidal agents within a biopolymeric alginate matrix. Specifically, the selected biocides were titanium dioxide (TiO_2) and sodium dichloroisocyanurate (NaDCC). The photocatalytic oxidation performed by the first compound has a great potentiality, being an effective process for preventing biofouling on stones[7]. Concerning the other oxidative biocide, the slow decomposition reaction of NaDCC can allow to moderate the amount of free hypochlorous acid in the hydrogel. Therefore, the side reactions responsible for the loss of hydrogel stability, observed using hypochlorite salts, should be drastically reduced.

A.2.1 Materials

Alginic acid sodium salt from brown algae (low viscosity), sodium dichloroisocyanurate dihydrate (NaDCC) and calcium chloride anhydrous were purchased from Sigma Aldrich; titanium dioxide (TiO_2) was obtained from Degussa in the form of anatase photocatalyst P25 (nanocrystalline

anatase with surface area of 50 m^2/g and a particle size of about 20 nm). For the activation of TiO_2, a Philips TL 6 W BLB wood lamp with an emission range between 340 and 400 nm and a radiant exitance of about 630 W/m^2 was used. "Pietra di Lecce" calcarenite samples of approximately 5×5×2 cm^3, composed of 93–97% calcium carbonate and a porosity of about 35%, were purchased from DÉCOR, Monteroni (LE), Italy. Agar was purchased from Sigma Aldrich as well as the salts employed for BG11 mineral medium preparation[8].

A.2.2 Hydrogel preparations and optimization

Hydrogels were prepared by dispersing sodium alginate in distilled water under vigorous magnetic stirring at room temperature. When a homogeneous solution was formed, both Ca^{2+} ions and the biocide were added. For what concern NaDCC as biocide, a solution obtained by mixing NaDCC and calcium chloride was added dropwise to the alginate solution, while in the case of TiO_2 it was dispersed as a powder directly in the sol system, and the resulting suspension was crosslinked with calcium chloride solution, added drop by drop. A homogeneous crosslinking was obtained by vigorous magnetic stirring. Different hydrogel formulations were designed by varying the amounts of alginate (from 2.5 to 5.0%), calcium ions (from 0.15 to 0.3%) and biocides (TiO_2 or NaDCC). In the case of hydrogel added with TiO_2, different parameters were changed: the concentration of TiO_2 (0.5 ÷ 2.0%), the distance of the sample from the light source (2 ÷ 16 cm), so that the intensity of the radiation reaching the surface was sufficient to stimulate the photocatalytic activity of titanium dioxide, and the irradiation time. The concentration of NaDCC ranged from 0.2 to 0.8%. To evaluate the stability of the two hydrogels, viscosity

measurements were performed at 25 °C by using a Fungilab Viscolead rotational viscometer (mod. ADV "L"). All the biocidal hydrogels (biogels) were applied on stone surfaces (0.1 g/cm^2, thickness of about 1÷1.5 mm) artificially colonized by filamentous cyanobacteria and green microalgae, identified by label LSA and LSB) as described previously[9]. The application was carried out with the aid of a cotton gauze, placed between the hydrogel and the stone surface, and after approximately 24h the dried gels were easily removed through a peeling process, thanks to the aid of the gauze.

As just described different hydrogel formulations were prepared and tested on biocolonized stone samples to find the optimal conditions needed for the complete removal of the biological patina. The best results were achieved with the following compositions:

- Alginate 5%, TiO_2 2% and CaCl2 0.15% (BIOGEL-1)
- Alginate 5%, NaDCC 0.4% and $CaCl_2$ 0.3% (BIOGEL-2)

Samples treated with BIOGEL-1 must be placed at a distance of 2 cm from the light source and irradiated with the wood lamp for 24 h. These two formulations, stored at 4 °C and, as regards BIOGEL-1, in the dark to avoid TiO_2 pre-activation, were tested over time to verify their effectiveness, and, after more than a week of storage, the two hydrogels retained both consistency and biocidal activity, overcoming the drawbacks encountered with hypochlorite-based hydrogels. The stability of both hydrogels was estimated by viscosimetric measurements as a function of storage time and compared with those obtained with a hydrogel containing 0.4% $Ca(ClO)_2$. First, the viscosity of the fresh alginate-biocide hydrogels was measured to determine their respective reference value. Then, the viscosity of all hydrogels was monitored over time. As regards BIOGEL-1, containing the

dispersion of TiO_2, up to one week of storage, no significant changes in viscosity were found, indicating that its oxidizing activity was inhibited by the absence of a light source. In contrast, the viscosity of the other two hydrogels, with hypochlorite salt and NaDCC as biocides, decreased exponentially by about 50 and 20%, after one day and 80 and 50% after three days, respectively. In fact, hydrogels containing ($Ca(ClO)_2$) or releasing (NaDCC) ClO^- ions exerted their oxidative action on the alginate structure by fluidifying the gel and losing their biocidal activity. However, the hydrogel containing the hypochlorite salt lost its consistency, and therefore its oxidizing activity, much faster than the one containing NaDCC.

A.2.3 Photographic and stereomicroscopic images

To assess the degree of biodegradation of stone materials and the effectiveness of hydrogel treatments, digital photos were taken with Canon EOS 1300D. Moreover, microscopic images of the colonized stones were acquired using a Leica S8APO stereomicroscope equipped with EC3 in reflecting mode, which allows to examine even thick samples, as in our case. Both photograph and stereomicroscopic images are collected in Figure 1.

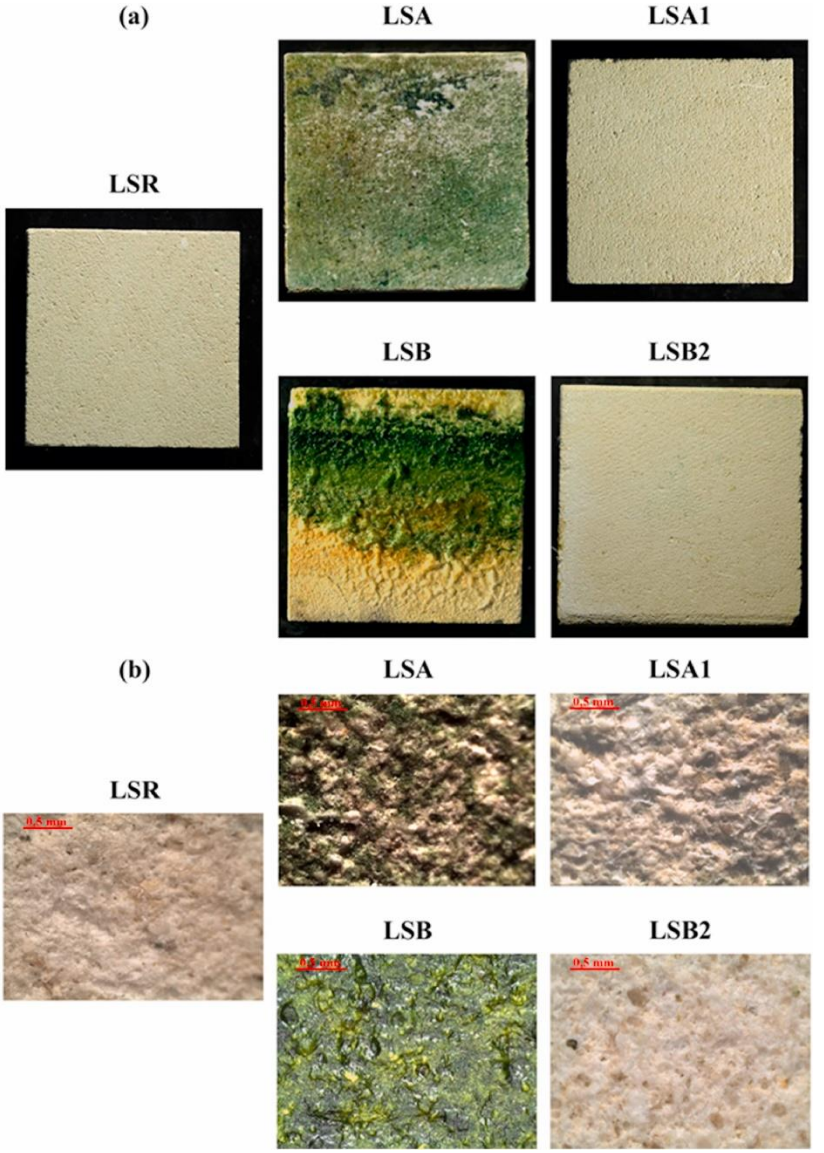

Figure 1: (a) Photographs and (b) stereomicroscopic images (magnification 4x) of the reference stone LSR, and the artificially colonized stones, before (LSA and LSB) and after hydrogel applications (LSA1 cleaned with BIOGEL-1 and LSB2 cleaned with BIOGEL-2).

Figure 1a shows the photographs of one reference stone (LSR) and two colonized stones before, LSA and LSB, and after treatment with, respectively, BIOGEL-1 (LSA1) and BIOGEL-2 (LSB2). These images allow

us a macroscopic view of the cleaning efficiency. Thanks to the 4x magnification stereomicroscope images, shown in Figure 1b, it is evident that both optimized hydrogels are able to remove the biopatina from the stone surface and that the cleaning was effective even for the microbial species present in the deepest pores.

A.2.4 Color variations

To evaluate the effect induced by the hydrogel applications, colorimetric values were determined by using the CIELAB color space proposed in 1976 by the International Lighting Commission (CIE)[10].

The color modification (ΔE*) was calculated using the following relation:

$$\Delta E^* = \sqrt{\Delta L^{*2} + \Delta a^{*2} + \Delta b^{*2}}$$

where ΔL*, Δa* and Δb* represent the difference of each chromatic coordinate between the measured samples and the reference. This parameter is important for aesthetic reasons, since a treatment must not induce ΔE* greater than 5, in order to preserve the original color of the surfaces[11]. The Sama Tools SA230 portable colorimeter was used for colorimetric analyses; measurements were made in SCE mode with an 8° standard observer, light D65 (average daylight, including the UV region, with the relative color temperature of 6504 K). The instrument was calibrated with the white reference. The measurements were performed in reflectance and 25 points per sample were taken in order to cover an overall surface of 60%. Colorimetric measurements were performed on several Lecce stone specimens taken as references. The average values of chromatic coordinates L*, a* and b* were respectively 80.5 ± 0.5, 3.3 ± 0.1 and 11.4 ± 0.4. Table 1 shows the mean changes of colorimetric

parameters between the reference (LSR), colonized (LSA and LSB) and cleaned samples (LSA1 and LSB2), along with the corresponding color differences, ΔE*.

Table 1: Chromatic coordinates - mean changes of the colonized (LSA and LSB), the respective cleaned (LSA1 and LSB2) samples with reference to untreated (LSR) one's and the corresponding color difference $\Delta E^* = [(\Delta L^*)^2 + (\Delta a^*)^2 + (\Delta b^*)^2]^{1/2}$. *The average values of L*, a* and b* of the LSR sample were respectively 80.5 ± 0.5, 3.3 ± 0.1 and 11.4 ± 0.4.*

	ΔL*	Δa*	Δb*	ΔE^*_{ab}
LSP-A	-34±9	-4±3	-4±5	35±8
LSP-B	-36±6	2±5	15±4	40±4
LSC1-A	-0.8±0.3	-0.45±0.02	-0.5±0.4	1.06±0.04
LSC2-B	0.2±0.6	-0.7±0.2	-0.8±0.6	1.2±0.3

The ΔE* value of both colonized samples, as expected, is very high but, after the treatments with the two hydrogels, the values of LSA1 and LSB2, that are 1.1 ± 0.4 and 1.2 ± 0.3 respectively, are well below the threshold perceived by the human eye.

A.2.5 SEM/EDS analysis

Scanning electron microscopy in combination with energy-dispersive X-ray spectrometry (SEM/EDS) is a proven forensic tool and is used to analyze several kinds of trace evidence. The X-ray detector, or more specifically, the EDS technique is used to determine qualitatively, and more often "semi-quantitatively", the elemental composition of an area of interest[12]. To examine the surface topography and composition of the samples, Zeiss GeminiSEM 500 equipped with EDS OXFORD Aztec Energy with INCA X-ACT detector was used with a working distance of 8.5 mm and an accelerating voltage of 15 KeV. The SEM/EDS analyses were carried out on the reference sample, LSR, and on two stones treated with the two hydrogels to evaluate the possible presence of residues after the cleaning

procedure. Figure 2 shows the SEM images of the untreated (LSR) and treated samples with BIOGEL-1 (LSA1) and BIOGEL-2 (LSB2) and the elemental analysis of some different areas selected for each specimen.

AREA 1	
	Wt%
O	49.2
Ca	39.6
C	9.4

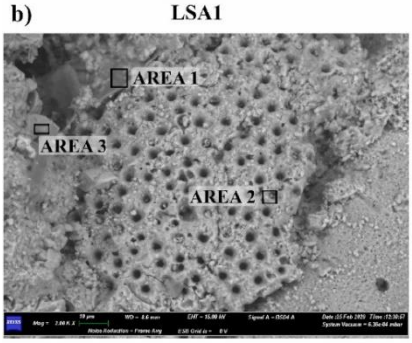

AREA 1		AREA 2		AREA 3	
	Wt%		Wt%		Wt%
O	47.4	O	55.7	O	47.6
C	22.0	Ca	31.7	C	22.3
Ca	18.2	C	11.2	Ca	20.7
Na	6.5	Ti	0.5	Na	4.2
Ti	3.9			Cl	3.1
Cl	1.6			Ti	0.8

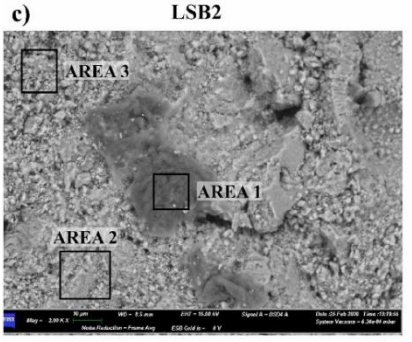

AREA 1		AREA 2		AREA 3	
	Wt%		Wt%		Wt%
O	32.4	O	50.0	O	49.6
C	31.9	Ca	38.3	C	36.3
Ca	17.5	C	10.0	Ca	8.1
Na	3.8			Na	0.9
Cl	3.7			Cl	0.8

Figure 2: On the left, SEM images of the LSR (a), LSA1 (b) and LSB2 (c) samples, being LSA1 and LSB2 the stones treated respectively with BIOGEL-1 and BIOGEL-2. On the right, the results of the elemental analysis, performed on some selected areas corresponding to the black frames in the SEM image.

The image and elemental composition corresponding to Area 1, shown in Figure 2a, relating to LSR, are typical of a calcarenite. On the other hand, images of the two treated samples (Figure 2b and c) showed some matted areas, randomly distributed, deserving to be investigated through the local elemental analysis. Areas 1, 2 and 3 (Figure 2b) correspond to three different examined zones of the Lecce stone sample treated with BIOGEL-1, LSA1. Low amounts of titanium were observed in the corresponding spectra, especially in the matted areas, highlighting the deposition of biocidal residues on the stone surface after the treatment. Moreover, the elemental analysis in both Lecce stone specimens treated with BIOGEL-1 and BIOGEL-2, highlights non-negligible percentages by weight of sodium and chlorine, derived from the crosslinking process, and an increase in the relative carbon content compared to the LSR sample. The presence of these elements is attributable to small residues of hydrogel mainly located in the matted regions of Figure 2b and c, whose presence could be due to the use of the cotton gauze that cannot avoid the contact between the hydrogel and the stone surface. In the other areas of the substrate, the concentration of calcium is very similar to that of untreated sample (Area 2 of Figure 2b and Areas 2 and 3 of Figure 2c), indicating that the crosslinker calcium chloride was not released on the specimen surface. Nowadays, we are studying the replacement of cotton gauze with other more uniform materials.

A.2.6 Hygroscopic properties with unilateral NMR

We studied hygroscopic behavior of the samples under analyses through NMR transverse relaxation time (T_2) measurements during water uptake[13]. The T_2 relaxation signal profiles and the equilibrium magnetization values

can identify adsorbed water with different mobility, i.e., water inside pores of different dimensions. Therefore, by comparing the T_2 distribution profiles of untreated, colonized and cleaned samples, it is possible to study the effects of the biofouling and cleaning operations on hygroscopic properties of the lithotype porous structure. The NMR equipment is a mq-ProFiler (Bruker, Italy), consisting of a surface probe and a portable electronic apparatus. The coil in use works at a Larmor frequency of 17.8 MHz, which can excite the sample up to a depth of about 2 mm and with a sensitive volume (x, y, z) of about $2 \times 2 \times 0.8$ cm^3.

The kinetics of water uptake in the sensitive volume were followed over the course of time keeping the device on the surface opposite to that in contact with the water source, starting from dry up to water saturated condition.

The capillary water absorption by using NMR instrument was performed according to the procedure described in the European Standard[14]; samples were dried in the oven at 40 °C until a constant weight was reached. Each stone sample was placed on filter paper (1 cm thick and 9 cm in diameter) and put in contact with the water source (dipped up to approximately 0.5 cm), through the selected surface, and with the NMR instrument on the opposite face. Details about the protocol used to determine the hygroscopic properties were previously reported[9]. In Figure 3a the mean LSR data is reported and used to compare its behavior with those of one of the two colonized stones, LSA; data of LSB were not reported since they are roughly overlapping with those of LSA.

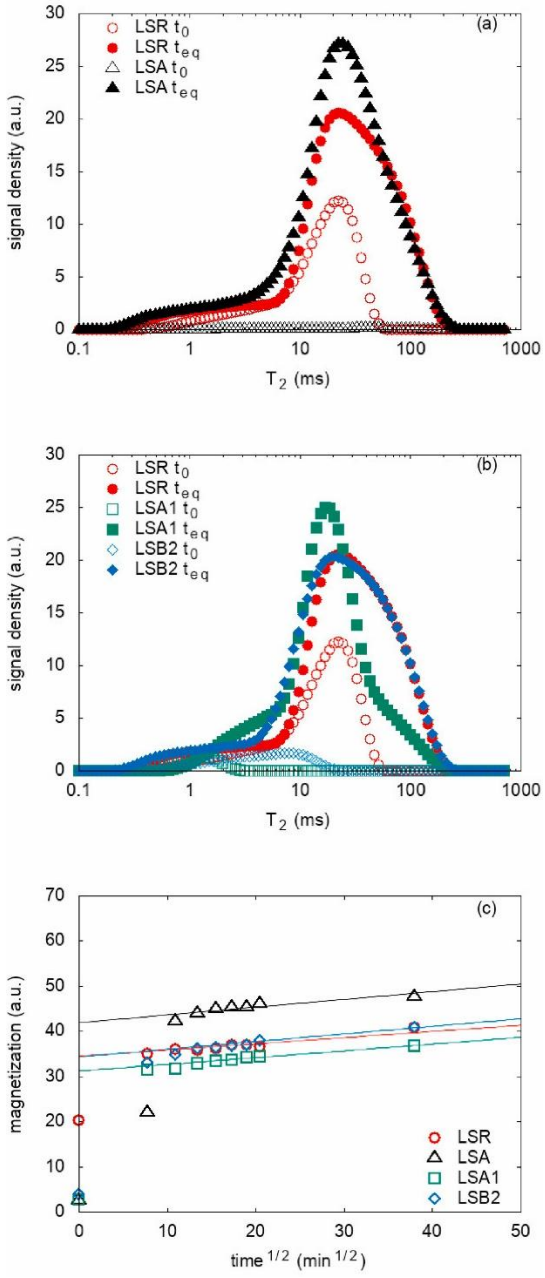

Figure 3: T_2 distributions during water uptake, at dry (t_0) and saturation conditions (t_{eq}), for Lecce stones: (a) in reference LSR and in biocolonized LSA samples; (b) in LSR and cleaned LSA1 and LSB2 samples. (c) Magnetization evolution during the first day of water uptake in LSR, LSA, LSA1 and LSB2.

Within the initial stage of LSR hydration, specifically at t_0, the mean signal amplitude reveals a T_2 population in the range 1 ÷ 50 ms, which should be assigned to the small pores filled and/or from large pores only partially hydrated[13]. On the contrary, for the colonized samples, within the first hour of absorption, no signal is detectable, indicating that microorganisms strongly affect the capillarity properties of the stone samples. After the cleaning treatment (Figure 3b) with BIOGEL-1 and BIOGEL-2, an appreciable difference compared to the reference is observed. There is a noticeable lowering of the signal in the t_0 curve attributable to the capillary rise inhibited by the presence of residual products, as evidenced also by SEM/EDS analyses, which slightly affect the surface porosity. At the end of water absorption, t_{eq}, the LSR's signal amplitude increases, and the distribution is shifted towards larger values of transverse relaxation times because, in the course of water uptake, the amount of water near the analyzed surface increases, and larger pores are gradually filled. The saturation condition for LSA sample (Figure 3a) shows a different behavior: the T_2 range is equal, but the corresponding magnetization values, which can be interpreted in terms of water content, override those of the reference sample. In Figure 3b, the saturation conditions for both stones treated with the two different hydrogels are compared with the reference one. While the curve of LSA1 appears shifted to lower value of relaxation time, sharp and higher than the reference, that of LSB2 t_{eq} overlaps the LSR profile. The area under the T_2 distribution gives the total magnetization and, as we have just mentioned, it is proportional to the mass of water in the lithotype pore spaces inside the sensitive volume of NMR probe. Figure 3c shows the magnetization evolution against the time square root for all the samples. The colonized sample shows a different behavior of hydration

compared to the reference. In fact, at lower absorption time, up to 2 h of absorption, a clear delay is observed, after which the magnetization values of the colonized samples override those of the reference. After the treatment with both the biocidal hydrogels, the hygroscopic behavior of the stone samples appears restored and comparable to the reference. However, for the sample cleaned with BIOGEL-1 a uniform drop of the time evolution of its magnetization confirms what previously discussed about the presence of titanium dioxide residues on the stone surface.

A.2.7 Test on biocidal activity

Agar plates and colonized stones were divided in two areas of the same dimensions: one side was subjected to the treatment with one of the two formulated hydrogels, while the other one was used as control. The evaluation of the effect of the biocide-hydrogels on the biofilms growing both on agar and calcareous stone was accomplished measuring the photosynthetic activity with a portable pulse amplitude modulated (Mini-PAM) fluorometer, coupled to WinControl Software (Walz GmbH, Effeltrich, Germany). During all measurements, the fibre-optic probe of the PAM was held in a stand to keep a distance of 5 mm from the biofilm. The maximum potential quantum yields (F_v/F_m) were assured by performing the measurements before and 24 h after the treatment, on dark-adapted samples; this was done by making measurements on samples kept in the dark for 30 min and the subsequent measurements were made in quasi-darkness (<1 μmol photon m^2s^{-1}). F_v is the maximal fluorescence yield, F_m the maximum variable fluorescence of the dark-adapted sample[15,16].

The biofilms collected with the adhesive tapes in correspondence of a calcareous surface in the Catacombs of SS Marcellino and Pietro with an

evident colonization of phototrophic microorganisms, formed a total covering in the four agar plates (Figure 4a). The observations carried out at the light microscope showed that the biofilms grown in the agar plates resulted from the following species of cyanobacteria: *Scytonema* sp. and *Symphyonemopsis* sp. (AP_1), *Scytonema* sp. and *Oculatella subterranea* (AP_2), *Leptolyngbya* sp. (AP_3), *Scytonema* sp. and *Leptolyngbya* sp. (AP_4). The same strains isolated in culture[17] were used to artificially colonize four calcareous stones (Figure 4b). The biofilms grown on agar plates were treated only with BIOGEL-2, due to the greyish color of activated-TiO2 that prevented the possibility to further evaluate the viability of the biofilm on agar plates. Two calcareous colonized stones were treated with BIOGEL-1 (CS_2 and CS_4) and two with BIOGEL-2 (CS_1 and CS_3). As shown in Figure 4a, the application of BIOGEL-2 on the half of each biofilm grown in the agar plates induced a total bleaching of the biofilms after 24 h from the application. The same results have been obtained with the application of both biogels on the half of each biofilm grown on the calcareous stones (Figure 4b).

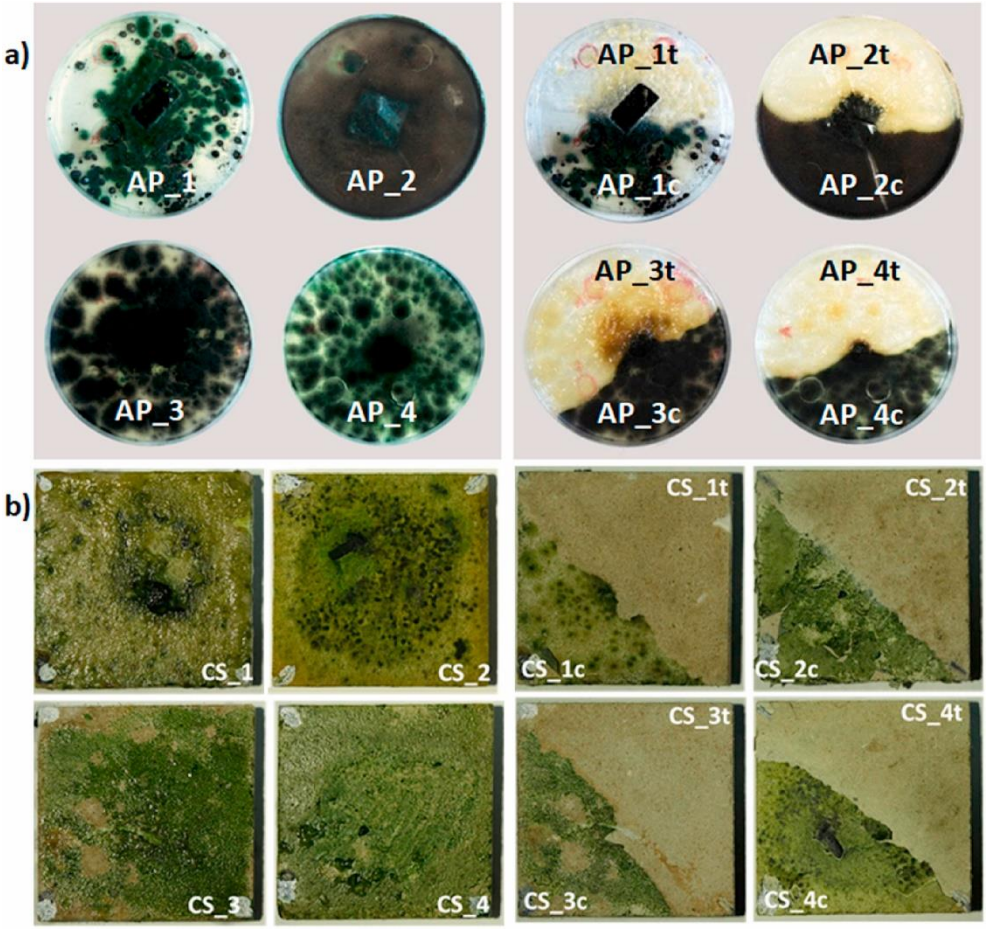

Figure 4: (a) Biofilm obtained by samples collected from the Catacombs of SS Marcellino and Pietro, before (on the left) and after (on the right) the biocide treatment with BIOGEL-2 on one half of their area (c = control; t = treated). b) Artificial biofilm obtained by inoculating a mix of the cyanobacterial strains Scytonema sp., Symphyonemopsis sp., Leptolyngbya sp. on calcareous stones, before and after the treatment with BIOGEL-2, CS_1 and CS_3, and BIOGEL-1, CS_2 and CS_4, (c = control; t = treated).

To evaluate the vitality of biofilms after treatments, the photosynthetic efficiency was measured on agar plates and stones, before and 24 h after the biogel applications (Figure 5). Typical curves of maximum potential quantum yields were obtained before the treatments (Figure 5a and c) on biofilm grown both on agar plates and stones; 24 h after the applications,

the biofilms on agar plates, treated with BIOGEL-2 (Figure 5b), and the biofilms on stones treated with both biogels (Figure 5d) underwent a drastic reduction in yields. After 1 month from the biocide applications, the mitigation effect on cyanobacterial biofilms persisted both on agar and stones.

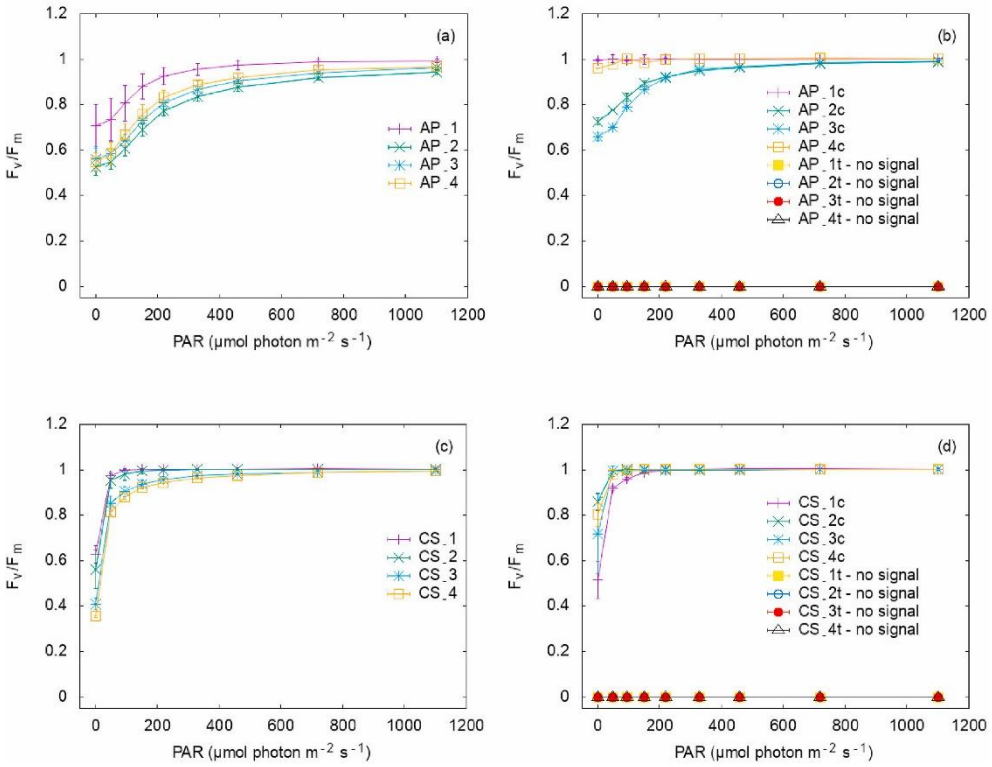

Figure 5: Photosynthetic yield (F_v/F_m) of cultured biofilms on a) agar plates (AP) and c) calcareous stone (CS) before treatments. In b) and d) F_v/F_m on control and treated areas, (c = control; t = treated), of items reported respectively in a) and c). 24 h after hydrogel applications, evaluation of F_v/F_m showed no signal in samples AP treated with BIOGEL-2 and CS treated with BIOGEL-1 (CS_2t and CS_4t) and BIOGEL-2 (CS_1t and CS_3t) respectively.

Colorimetric measurements were also performed on both halves of colonized/treated stones to evaluate if, after the cleaning, the color of the stones has been restored. As previously seen for the cleaning treatments on

LS specimens, the color difference, ΔE*, between the treated stones and the untreated ones was well below the just discussed threshold.

A.2.8 Conclusion

Two main formulations of alginate hydrogels, prepared with TiO_2 and NaDCC as biocides, were successfully used to remove filamentous cyanobacteria and green microalgae from artificially colonized Lecce stones. The effectiveness of the cleaning treatments was evaluated with different techniques, which revealed that the hydrogels not only completely remove the biopatina from the surface of the stone, but also do not modify the chromaticity and capillary properties of the treated substrate. The biogels, applied on calcareous stones colonized by cyanobacterial biofilms collected in Roman Catacombs, showed a drastic reduction in their photosynthetic activity a few hours after the biocidal application and this effect lasted at least one month.

A.3 Protection: acrylic and silane coatings on limestone

To preserve the stone artworks, it is necessary to apply a protective barrier between the stone and the external agents, in particular water. For this purpose, it is necessary to reduce the wettability of the material without altering its original permeability to water vapor, allowing the rebalancing of the stone moisture content according to environmental conditions. Coatings have to penetrate inside the porous materials by covering their pores, but avoiding the formation of thin layer deposited on their surfaces that could hinder the natural exchanges of water vapor between stone and environment[18].

Since ancient times, natural hydrophobic compounds, such as oils, resins and waxes, are used as water repellents for the protection of stone surfaces[19], but continuously new natural and synthetic polymeric materials are proposed as protective and water-repellent products for stone artworks. In accordance with the current European Standard[20], they should possess some requirements when they are applied to stone: the reduction of liquid water absorption with a minimum change of the substrate permeability to water vapor, the maintaining of the original color and gloss of the substrate and of its physical and chemical properties. Moreover, they should not produce by-products that could be harmful to humans and the environment.

In the here presented work, five protective coatings were compared, three of which silane/siloxane-based, which were the most employed class of protectives in cultural heritage field[21,22], and two new acrylics, synthesized by Icap Leather Chem S.p.A. (Milan, Italy), not yet available for sale. Acrylic polymers are generally known as good hydrophobic materials but as aforementioned, they were no longer applied mainly due to their negative side effects of the treated surfaces. Protectives were applied on Lecce stone specimens, one of the main building materials in historical Baroque monuments in southern Italy. In particular, the effects of these products on the samples were assessed in terms of (i) surface hydrophobicity and chromaticity (ii) hygroscopic behavior during water uptake, (iii) porosity, (iv) distribution of the products on the stone surface and (v) their penetration depth into the stone volume.

In particular, NMR relaxometry was used as a non-destructive and non-invasive technique to evaluate the effect of treatment on both the open porosity and the diffusion of water inside the structure with respect to the untreated one[13,23–25]. Micro-FTIR or SEM-EDS analyses, according to the nature of the protective material, were performed as a very effective method to analyze point by point the coating distribution[12,26].

A.3.1 Materials

Lecce stone (LS) is a fine-grained calcarenite stone, composed of 93–97% calcium carbonate and with a characteristic pale-yellow color. The porosity is around 31–45%, with two Gaussian pore size distribution centered at 0.1 ÷ 0.2 μm and 0.5 ÷ 4 μm[27,28]. LS samples of approximately 5×5×2 cm^3 were purchased from DÉCOR, (Monteroni, Italy). The commercial coatings chosen for the experimentation were: ETS WR® (WR), a water-repellent tetraethyl orthosilicate-based consolidator in isopropyl alcohol by Mapei S.p.A. (Milan, Italy); Hydrophase® Acqua (HY), a water dispersed alkyl/alkoxysilanic resin with catalyst by Phase Restauro S.r.l., (Florence, Italy) and Nanoprotect (NP), an alkyl polysiloxane-based material in water by I.M.A.R. Italia S.p.A. (Rome, Italy). We also focused our attention on two newly synthesized water-based polyacrylic polymer coatings, Polyrest HR2 (HR2) and Polyrest HR3 (HR3), produced and kindly provided to us by ICAP Leather Chem S.p.A. (Milan, Italy).

A.3.2 Coating procedure and static contact angle

Three LS specimens of similar mass (~80 g) were selected for each treatment; before applying the protective products, the samples were dried in an oven at 60 °C, until they reached the dry weight.

The WR, HY and NP as provided by the producers, and HR2 and HR3 as water dispersions (10%), were homogeneously distributed on one of the stone surfaces (25 cm^2) using a graduated pipette until surface saturation, to accurately control the amount of protective added to the specimens. The solvents were allowed to evaporate in air for eight weeks and then the stone specimens were dried in an oven at 60 °C to determine the dry residues, Q. It was determined according to the following equation:

$$Q = \frac{(m_A - m_B)}{m_B} \times 1000 \qquad (1)$$

where m_B and m_A are the stone dry masses, before and after the treatment. The wettability of the stone surface was monitored by the measurement of the static contact angle, using a Krüss Drop Shape Analyzer DSA100 instrument. For each measurement, a deionized water droplet (5 μL) was deposited on the sample surface at room temperature. The drop profile was extrapolated using an appropriate fitting function, and, considering the natural inhomogeneity of the stone material, the mean contact angle of a surface was achieved by averaging on nine measurements performed on different points of the surface. Table 2 shows the mean dry weight values of the untreated Lecce stone samples, the mass of applied polymeric solution, the dry residue of polymer within the specimen volume, Q, determined by eq. (1), and static contact angle.

Table 2: For each coating, mean values of dry weight of the untreated samples, mass of added protective solution, dry residue of the product and static contact angle.

	Dry weight of untreated samples, g	Mass of protective solution, g	Q, %	Static contact angle, °
HR2	86.1 ± 2.1	1.6 ± 0.3	0.7 ± 0.4	136 ± 7
HR3	85.9 ± 1.4	1.7 ± 0.3	0.90 ± 0.04	135 ± 7
NP	85.3 ± 1.3	1.6 ± 0.3	0.28 ± 0.08	130 ± 5
HY	86.8 ± 2.8	3.4 ± 0.9	14 ± 8	141 ± 8
WR	83.2 ± 3.2	1.8 ± 0.2	11 ± 2	138 ± 9

In Table 2, when the coatings are compared to each other, strong differences are found out in terms of amount of polymer dry residues, which range from 0.28% to 14%. Acrylic polymers HR2 and HR3, whose aqueous dispersions contain the same concentration of product, show very similar values of dry protective deposited, comprised between 0.7% and 0.9%. On the contrary, among silane-based coating, NP-coated samples show the lower Q value, while HY and WR are the products with the higher dry residues. These differences in the amount of polymer deposited may be due to the different concentration of silane precursors, not reported by the suppliers. A comparison of our results with previously published data is not trivial, since the coating uptake, as well as the class of the protective agent, depends on the type of stone, i.e., on its porosity and composition, and on the type of application. In fact, in a recent study, the amount of product applied on marble was approximately thirty times lower with respect to Lecce stone samples, due to its greater compactness which limited its penetration[29]. The method of application is also crucial as reported by Adamopoulos et al.[30] for marble samples. In fact, the product uptake was

very different when it was deposited on the specimens by brush, spray or dip coating. For what concerns the macroscopic effect of a hydrophobic coating, the contact angle of water with the sample surface (CA) is the more classical evaluation method. Due to the fast absorption of the water droplet, CA of the untreated reference samples could not be measured. Although the strong differences between the coating dry residues, CA values result very similar and, regardless of the nature of the applied polymer, they range around 135°, indicating a good hydrophobicity of all the coated surfaces.

A.3.3 Colorimetric Measurements

Another important aspect of the protection treatment is the changes in colorimetric properties induced by the protective on the surface of the substrates; in fact, during the restoration interventions, particular attention has to be addressed towards the color alteration of the coated surfaces with respect to the original chromaticity of the materials. Indeed, chromatic changes of stone surfaces induced by the protective coatings were evaluated by colorimetric analysis performed before and after polymer applications following the procedure illustrated in paragraph A.2.4. The colorimetric coordinates of all samples of Lecce stone before the treatment were acquired and averaged to obtain the reference values of L*, a*, b* and E* that corresponded to 76.4 ± 1.3, 4.4 ± 0.5, 13.3 ± 1.0 and 77.7 ± 1.5, respectively. Mean colorimetric variation values and standard deviations of samples treated with all protective coatings are listed in Table 3.

Table 3: For each coating, mean values of colorimetric coordinates variations of the treated surface with respect to the reference one.

Sample	ΔL*	Δa*	Δb*	ΔE*
HR2	−1.9 ± 1.3	0.8 ± 0.7	2.3 ± 1.3	3.1 ± 1.4
HR3	−2.5 ± 0.8	0.9 ± 0.4	2.3 ± 0.9	3.5 ± 1.5
NP	0.0 ± 1.3	−0.1 ± 0.7	0.8 ± 0.9	0.8 ± 0.5
HY	−6.0 ± 1.3	1.8 ± 0.5	4.9 ± 1.9	8.0 ± 2.2
WR	−1.1 ± 1.3	0.3 ± 0.6	1.1 ± 1.0	1.6 ± 0.7

According to the literature, color differences between coated and uncoated samples below 3 are not significant, being imperceptible to the human eye, while the accepted level for conservative purposes is a $\Delta E^* < 5$[31,32]. Samples treated with acrylic polymers, HR2 and HR3, appear slightly darker and yellower than the reference and the color differences of the specimens are not much higher than the perception limit and well below the accepted level for conservation purposes. Regarding the siloxane polymers, HY produces a considerable and visible effect on the stone surface, being the ΔE* value of 8.0. In particular, analyzing the individual colorimetric coordinates, the treated surface of HY-coated specimens appears noticeably darker and yellower than the reference. The other silane-based coatings are almost entirely ineffective on the three chromatic coordinates, keeping the color of the support practically unchanged with a chromatic variation lower than the perception limit of the human eye.

A.3.4 Hygroscopic properties and porosity

The NMR equipment mq-ProFiler (Bruker, Italy), consisting of a surface probe and a portable electronic apparatus, was used to study the

hygroscopic behavior and the porosity of the samples thorough NMR porosimetry, i.e., transverse relaxation time (T_2) measurements[13]. The NMR signals were acquired using the CPMG with the shortest echo-time $2\tau = 44$ μs to reduce the diffusion effect. For every measurement of T_2 it was necessary to acquire 3000 echoes to cover the entire relaxation curves. Moreover, each sequence was repeated every 2 s for 512 times to maximize the signal-to-noise ratio, within a reasonable measurement time (~15 min). The coil in use works at a Larmor frequency of 17.8 MHz, which can excite the sample up to a depth of about 2 mm and with a sensitive volume (x, y, z) of about $2 \times 0.2 \times 0.8$ cm^3. The water absorption tests were carried out by capillarity, during water uptake, both on reference and treated samples. In particular, the stone samples were dried in an oven at 60 °C until they reached the dry condition and placed on filter paper (thickness 1 cm and diameter 9 cm) constantly saturated with water, according to the European Standard[14]. While the face in contact with the water was the treated one, the other face was put in contact with the NMR surface probe. The NMR signals acquired at fixed times during the capillary absorption, were processed using the inverse Laplace transform with the UPEN algorithm (UpenWin, villiam.bortolotti@unibo.it), to obtain the T_2-distributions during the kinetics of water absorption. The extrapolated equilibrium magnetization, obtained by UPEN in arbitrary units, allowed estimating the material's water content in the sensitive volume of the NMR surface probe[33]. Open porosity of reference and treated samples was evaluated by immersion. The samples were immersed and left in water until they reached a constant weight indicating the full saturation (~7 days). The surface porosities were evaluated through the equilibrium magnetization

data acquired from the untreated as well treated surfaces. Lastly, the gravimetric ratios were determined according to the following equation:

$$G = \frac{(m_s - m_0)}{m_0} \times 100 \qquad (2)$$

where m_0 and m_S are the stone masses, in dry and water-saturated conditions.

One of the most important roles of protective coatings is to slow down the water absorption of the material from the environment, avoiding however to modify the porous characteristics of the material itself. The effect of the protective coatings was evaluated by performing the water uptake for capillarity of the reference specimens and of all the coated samples through their treated surfaces. The mean water absorption kinetics are reported in Figure 6.

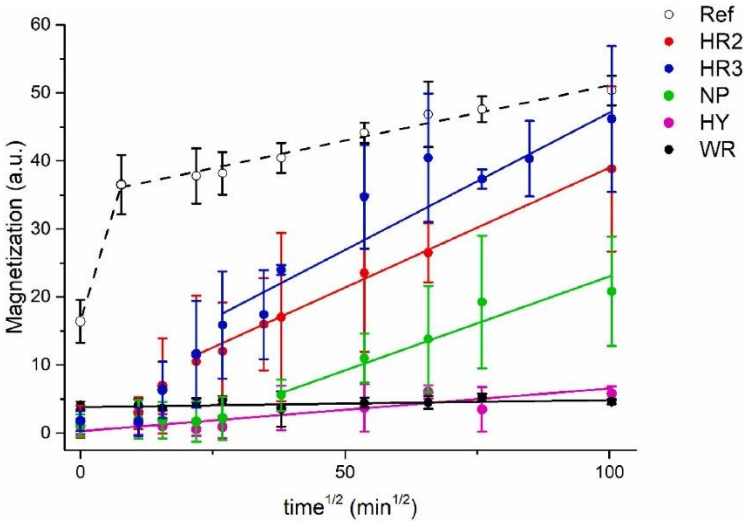

Figure 6: For each coating, mean kinetics behavior of water absorptions by capillarity through the treated surface of the sample. For comparison, in dashed black line, the mean kinetics through one face of the reference sample.

The reference LS specimen rapidly absorbs water showing two hydration phases: one, faster, during the first hour of water uptake and the second,

slower, recorded up to one week. The treated samples show a significantly different behavior from the reference one. In general, along the observation period, they are characterized by a complete hindrance of the water uptake for the first few hours, then by a single and more or less slow phase of hydration. The acrylic polymers, HR2 and HR3, induce a similar slowdown of the water absorption kinetics, however reaching an equilibrium water content similar to that of the reference. On the contrary, among silane-based polymers, HY and WR completely hinder water absorption during capillary uptake as highlighted by an almost constant value of magnetization, M_{eq} ~5. About samples treated with NP, over time, they absorb water very slowly and, after one week of absorption their mean magnetization was 2.5 times lower than that of the reference. However, unlike the other coatings, the three samples treated with NP show hydration behaviors with quite different slopes, as also highlighted in Figure 6 by the large error bars associated with this set of samples. The variabilities observed between the coated samples during water uptake are not perceived by the static CA measurements for which all the protectives are similar to each other. In fact, the measures of CA depend exclusively by the presence of the product on the substrate surface, while the NMR evidences are related to the distribution of the polymers within the specimen, which for our coatings is very different, as revealed by the microscopic observation reported in the next section.

To understand if the effects induced by the protectives were due to an increased hydrophobicity of the treated surface or to a change of the stone porosity, the reference samples and all the treated ones were water saturated by immersion and analyzed through NMR porosimetry. The measurements of T_2 distributions were performed on untreated and treated

surfaces of all water saturated samples. At the same time, their gravimetric ratios were also evaluated. Useful information can be obtained by comparing water content NMR data and gravimetric ratios as reported in Table 4, by recalling that gravimetric measurements provide details on the average behavior of the whole sample, while NMR analysis shows highly meaningful surface information.

Table 4: For each coating, values of gravimetric ratio and magnetization data of treated (MTS) and untreated (MUS) surfaces of the water saturated samples by immersion. The errors on all data are estimated around 5%.

	Gr, %	MTS, (a.u.)	MUS, (a.u.)
REF	18	—	49[a]
HR2	18	52	50
HR3	18	50	52
NP	18	45	51
HY	12	12	35
WR	13	25	51

Gravimetric and magnetization data do not highlight significant differences between the samples treated with the acrylic protectives and the reference one. On the contrary, considering the silane-coated specimens, some evidence is noteworthy. NP-coated sample, when compared with the reference, shows the same mean value of gravimetric ratio, but a slight decrease in the magnetization value if the NMR measurements are performed on the treated surface. Such evidence can be ascribed to a partial occlusion of the porosity only in the immediate vicinity of the NP-treated surface. The porous structure of HY- and WR-coated samples result drastically affected by the coating, being their gravimetric data reduced by about 30% compared to the reference. The magnetization values of the treated surfaces are in complete accordance with the gravimetric result; in

fact, they decrease, with the respect to the reference, by about 75% and 50%, respectively. Differently, the magnetization value of the untreated surface of HY-coated sample is reduced by about 30%, suggesting that the coating penetrates deeply throughout the stone, while that of WR-coated specimen is quite similar to the reference. It must be mentioned that during the immersion time of the WR-treated sample, part of the siloxane polymer comes out from the specimen making surfaces slimy, highlighting a partial dislocation in water of the coating polymer. This evidence was confirmed by ATR-FTIR spectrum of the quasi-dried spilled material, which shows the characteristic peak of the polymer at approximately 1070 cm^{-1}. Anyway, WR technical data sheet reports that the product could not be applied under counterthrust of water. For a further check, the same WR-coated sample was re-dried and subjected to a new water uptake for capillarity. In Figure 7 the results show a behavior similar to that of the reference stone, demonstrating the loss of a large amount of the polymer.

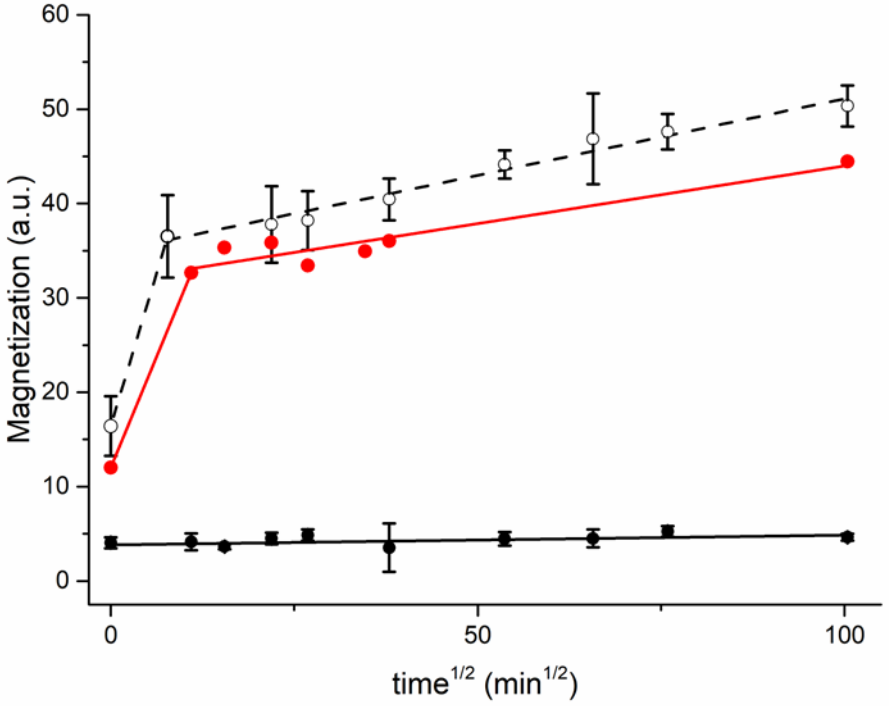

Figure 7: Kinetic of capillary water uptake profiles of reference sample (black dotted line) and of WR-coated specimen, before (black line) and after immersion in water (red line).

A.3.5 Microscopic analysis of coating distribution

Micro-FTIR and SEM-EDS techniques were used for the analysis of the surface and the determination of the coating penetration depth.

By micro-FTIR analysis, the distribution of the acrylic polymers HR2 and HR3, even on rough and inhomogeneous substrates[34], was monitored by using the Nicolet iN10 Infrared Microscope (Thermo Fisher Scientific) equipped with spatial motorized stage (in the x, y and z directions) of 70 × 127 mm^2. The micro-FTIR equipment is provided with IR source cooled with air, a KBr beam splitter and the acquisitions were performed using Cassegrain IR/VIS objective, always aligned at 15X/0.7 FWD 16 mm, with an MCT-A detector cooled with liquid nitrogen. FTIR spectra were

acquired in external reflection mode in the IR spectral region comprised between 4000 cm^{-1} and 675 cm^{-1} with a resolution of 8 cm^{-1} and 128 scans to increase the signal to noise ratio. All maps were composed by 100 spectra, organized in a 10 × 10 grid, each of which was acquired over an area of 100 × 100 μm^2. OMNIC Picta software was used to extrapolate the correlation maps for the reference, HR2-and HR3-coated samples by applying a first order correlation function in the region comprised between 1800 cm^{-1} and 1700 cm^{-1}; in fact, in this spectral region falls the characteristic absorption band of the carbonyl group of the acrylic polymers (at about 1750 cm^{-1}). The maximum value of correlation, equal to unity, was than assigned to the spectrum of the surface map, among all those acquired, which showed the highest intensity of the peak centered at 1750 cm^{-1}.

SEM-EDS technique was used to examine the surface topography and composition of the samples treated with silane-based products. Zeiss GeminiSEM 500 equipped with EDS OXFORD Aztec Energy with INCA X-ACT detector was used with a working distance of 9.0 mm and an accelerating voltage of 20 KeV. EDS microanalyses of reference and coated samples were acquired over an area of 1 mm^2 as a single map. Subsequently, all the treated samples were cut to evaluate the penetration of the products inside the substrates. Therefore, an incision was made with a saw on the untreated face of all the specimens and then they were divided in two parts using hammer and chisel, thus avoiding artificial alteration of the composition due to cutting. To rationalize the tests related to the penetration of the protective coatings into the samples, micro-FTIR and SEM-EDS results were spatially correlated to the observations

acquired by using an AxioZoom V16 (Zeiss) stereomicroscope equipped with the Zen Blue 3.3 software.

Analysis of the treated surface of the samples as well as of their sections allowed to rationalize the results described so far. In fact, micro-FTIR and SEM-EDS investigations were performed to understand the homogeneity of the protective coating on the stone surface and, by correlating them with the stereomicroscopic observations, the diffusion of the protective into the specimens[34]. For this purpose, the choice between the two selected techniques was accomplished according to the nature of the polymer applied. On the one hand, samples coated with acrylic coatings, HR2 and HR3, were analyzed using micro-FTIR due to the presence of the strong stretching band of carbonyl groups of the polymers, as highlighted by the spectra of reference and HR2-treated sample reported in Figure 8. On the other hand, silane-coated samples were studied using the SEM-EDS microanalysis focusing on silicon due to the low content of this element in the reference sample.

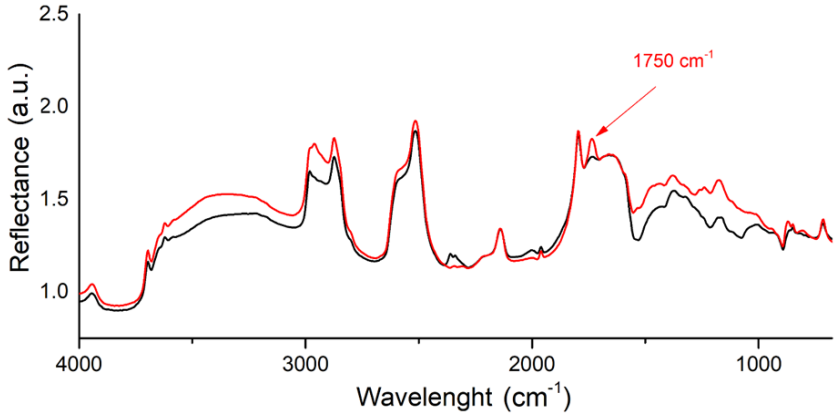

Figure 8: FTIR spectra acquired in total reflectance mode of HR2 product applied on the sample (red line) compared to the spectra of untreated Lecce stone (black line).

Acrylic coatings

Figure 9 shows the correlation maps resulting from the micro-FTIR analysis of the reference (a) and acrylic-coated samples: HR2 (b) and HR3 (c).

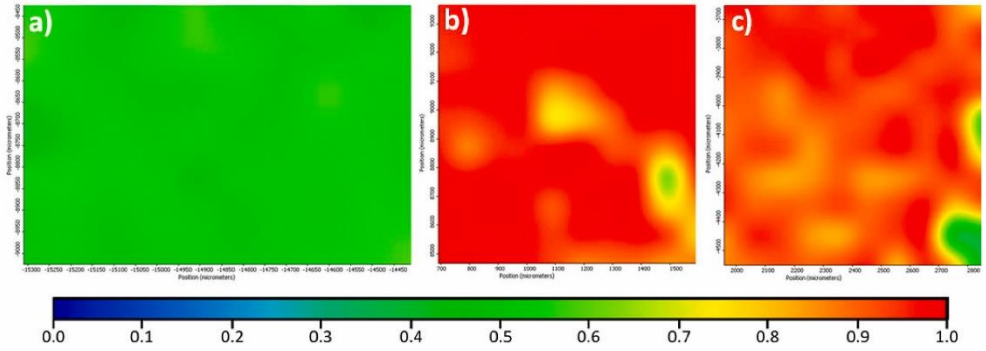

Figure 9: Correlation map of reference (a), HR2-coated (b) and HR3-coated (c) samples

The correlation factor (CF), ranging from 0.0 (full anticorrelation) to 1.0 (full correlation), is related to the presence of the stretching band of carbonyl groups along the surface and it is reported according to the map color bar. The image of the reference sample (Figure 9a) is fully homogeneous, and its intensity corresponds to the middle of the map color bar with CF = 0.5, which means no correlation. Differently, high correlation colormaps (CF > 0.9) are obtained for specimens covered with the acrylic polymers indicating that the coatings are homogeneously dispersed on the treated surface, except for some small green areas. To understand the degree of penetration of these coatings inside the stone material, the correlative analysis between stereomicroscope images and micro-FTIR data was carried out along the 2 cm section of the cut samples; the results are reported in Figure 10.

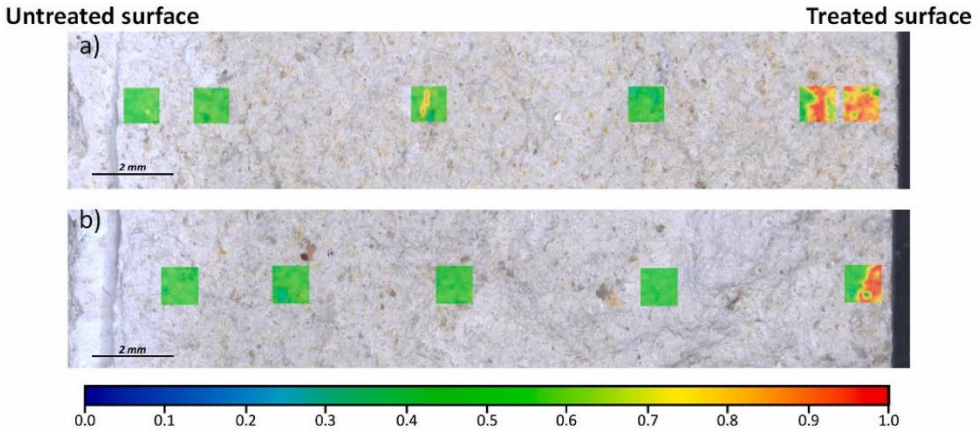

Figure 10: Stereomicroscope images correlated with micro-FTIR analysis of the samples treated with acrylic polymers HR2 (a) and HR3 (b).

The images clearly show that HR2 (Figure 10a) penetrates deeper inside the stone samples than the HR3 polymer (Figure 10b); in particular, HR2 reaches the correlation value of the reference at about 2.3 mm from the surface, but its presence is identified also in the middle of the sample at about 12 mm of depth. On the contrary, HR3 diffuses only up to 1 mm from the treated surface.

Silane-based coatings

Figure 11 shows the SEM images of reference and silane-coated samples, where the distribution of silicon, determined by EDS microanalysis, is evidenced in red.

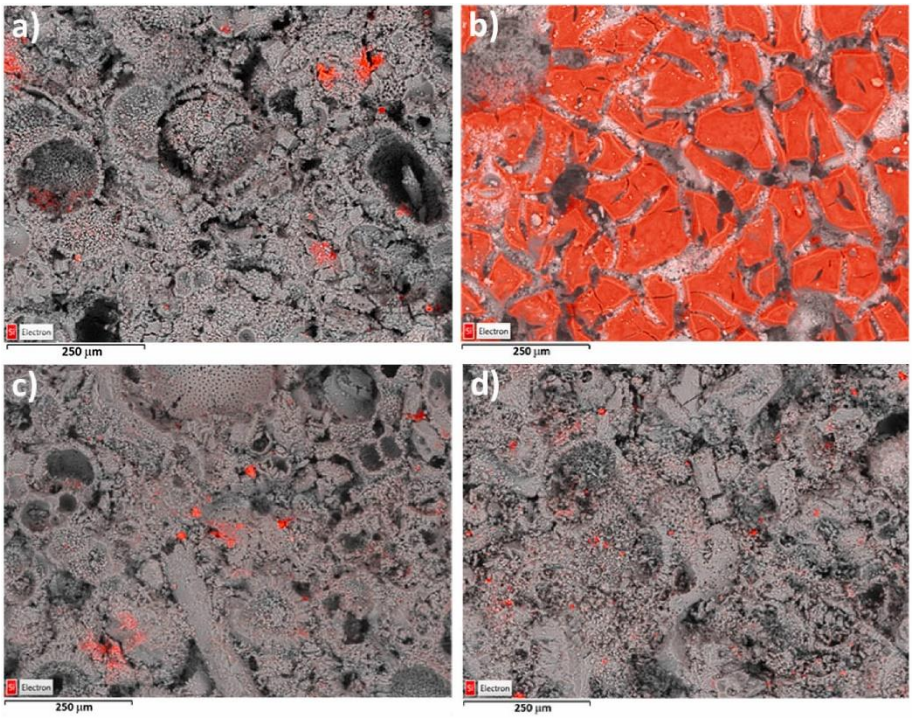

Figure 11: SEM-EDS images of the reference (a) and of the samples coated with NP (b), HY (c), and WR (d). The presence of silicon, highlighted by EDS, is evidenced in red.

The EDS microanalysis of the reference sample (Figure 11a) shows some red spots associated with the presence of silicon portions that could be due to inclusion of silicates into the carbonate matrix of Lecce stone. SEM-EDS images of the treated surfaces show, over the typical silicon spots of the reference, a uniform red patina due to the ubiquitous presence of silicon. In particular, for NP-coated sample (Figure 11b) a drastic change in morphology was observed, as highlighted by the formation of plaques of siloxane polymer on the stone surface. On the contrary, HY- and WR-coated samples (Figure 11c and d) appears very similar to the reference in terms of morphology, but with a slight red coloration over all the investigated areas, indicating a widespread increase in silicon content.

Even with silane-based polymers, the degree of penetration of the coating, along the 2 cm section of the cut sample, was studied by correlating stereomicroscope images and SEM-EDS analysis. The results are reported in Figure 12.

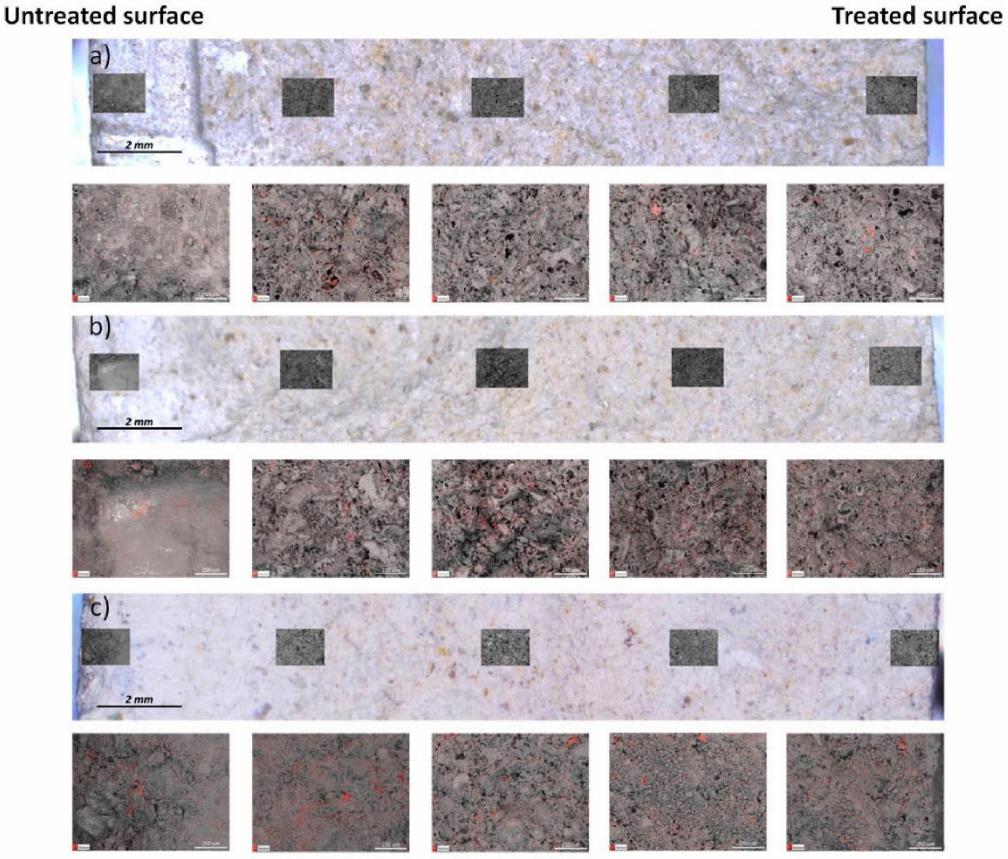

Figure 12: Stereomicroscope images correlated with SEM-EDS microanalysis of specimens coated with silane-based polymers, NP (a), HY (b) and WR (c).

All the investigated samples show the previously described red patina independently of the distance from the treated surface, clearly indicating the presence of silane-based polymers up to the untreated face, much more evident for the HY- and WR-coated specimens than for the NP-coated one.

To deal with the distribution of the protectives in the stone specimens, it was needed a more quantitative approach for analyzing the SEM-EDS images. As for silicon, also low content of aluminum was detected on the reference sample, due to the presence of aluminum-silicate inclusions in the lithotype. In fact, by assigning the yellow color to alluminum on the SEM images, the red spots ascribed to silicon became orange. The Si/Al ratio determined on six different areas of the reference stone surface resulted to be always about 2.0. Then, this ratio was set as a threshold value to discriminate intrinsic silicon from that added with silane-based polymers.

A.3.6 Comparison between the effect of acrylic and silane-based coatings

The means of the correlation factors of the micro-FTIR color maps (Figure 9) and of Si/Al ratios evaluated from SEM-EDS (Figure 11), concerning the reference and the treated surfaces for each coating, are reported in Table 5.

Table 5: For reference and coated samples, (on the left) mean correlation factors of surfaces treated with acrylic HR2 and HR3 polymers; (on the right) mean value of Si/Al ratios for surfaces treated with silane-based NP, HY, and WR polymers.

Correlation factor			Si/Al ratio			
REF	HR2	HR3	REF	NP	HY	WR
0.52 ± 0.04	0.97 ± 0.05	0.91 ± 0.09	1.9 ± 0.2	70 ± 7	7.0 ± 0.9	4.0 ± 0.7

Compared to the reference, the acrylic coatings appear very similar, with mean correlation factors higher than 0.9. This similarity between the acrylic polymers is also found out by looking at the dry product residues that range around 0.8% for both protectives (Table 2). For the silane-treated samples, significantly different evidence is observed for Si/Al ratios as well as for the

amount of the polymer dry residues (Table 2). The NP-coated samples, with the highest mean value of the Si/Al ratio (equal to 70), have the least quantity of dry residue (0.3%), while the HY- and WR-treated samples show Si/Al values of only 3.5 and 2 times higher than that of the reference, despite the higher values of dry polymer residues, being respectively 14 and 11%. These evidences suggested that, while NP mainly remained on the stone surface, both HY and WR penetrated along the section of the samples. The coating penetration into the sample was evaluated plotting the mean correlation factors for acrylic polymers (Figure 13a), and the Si/Al ratios for silane-based ones (Figure 13b) along the sample depths just visualized respectively in Figure 10, Figure 12.

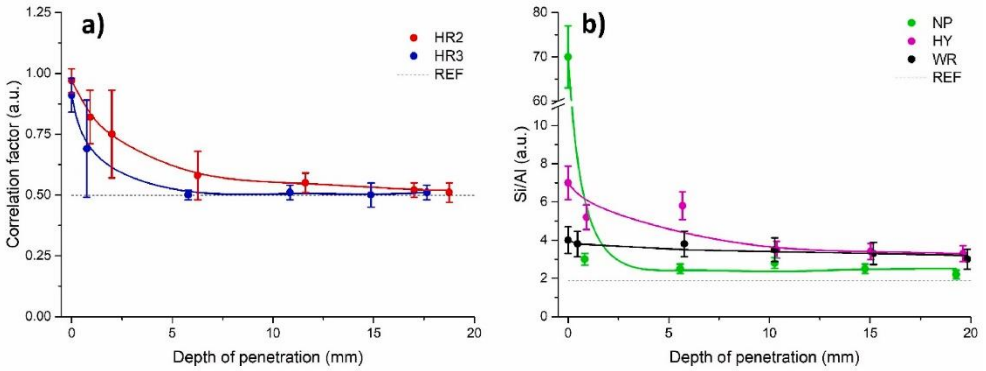

Figure 13: For each coating, penetration depth into the stone, expressed as mean value of the correlation factor (a), or of the Si/Al ratio (b). In each panel, the black dotted line corresponds to the threshold value of the reference.

It is evident from Figure 13a that HR2 penetrated deeper up to half section of the sample, while the degree of penetration of HR3 rapidly decayed to the reference correlation factor within the first 5 mm from the treated surface. The large error bars found for some points refer to those areas where the acrylic polymers and the constituent material coexist (Figure 10). Figure 13b confirms the previously formulated hypothesis about the silane

coatings; in fact, NP polymer remained almost completely on the treated surface and its content along the sample depth decreased rapidly towards a value slightly higher than the threshold one. Instead, HY and WR resulted more distributed from the treated to the untreated surfaces. Moreover, comparing the effect of these two polymers, significant amount of HY penetrates up to 5 mm from the treated surface, while the WR polymer diffuses more homogeneously from the treated surface to the untreated one. Despite the relative low surface amount of HY and WR, respect to NP, their persistence until the respective untreated surfaces are demonstrated by Si/Al ratios, that result double when compared with that of reference. The microscopic observations combined with micro-FTIR and SEM-EDS analyses were in complete accordance with the results obtained with the just discussed macroscopic characterization that allowed to discriminate the protectives according to their hygroscopic and porosity properties. In fact, the samples treated with the HR2 acrylic polymer, compared to the HR3-coated samples, showed a lower rate of water absorption by capillarity and a greater penetration of the coating inside the stone material. In both acrylic-coated samples, especially at short times of water absorption, the kinetics were very slow, demonstrating a relevant surface hydrophobicity of the treated samples. However, with nearly the same amounts of residual dry product, the acrylic-coated samples, when water saturated by immersion, showed similar gravimetric and NMR porosity data with respect to the reference samples, then revealing an open porosity equal to that of an untreated Lecce stone. Among the silane-coated samples, NP-coated ones showed an out-of-range fraction of polymer on the stone surface, in the form of more or less large plaques. According to the compactness of these plaques, water could be absorbed with different

timing, thus explaining the high variability of the water uptake rates of the three samples treated with this polymer. The water-repellent behavior of NP-coated samples mainly depends on the random morphology of polymer plaques, as also confirmed by the NMR porosimetry.

The other two silane-based polymers, HY and WR, according to microanalysis evidence, were ubiquitously distributed on the surface and on the entire volume stone, clearly highlighting a higher degree of penetration than that of the other products. This behavior, along with the higher amounts of dry residues, could explain the almost total occlusion effects observed during the entire capillary water uptake and under water-saturated conditions. For HY-coated sample, the low gravimetric factor as well as both magnetization values shown in Table 4 confirm this analysis. On the contrary, the porosity on both the faces of WR-coated sample does not seem to show the same behavior, probably due to the loss of polymer when the sample was subjected to water immersion.

A.3.7 Conclusions

This study reports the comparison between commercially available silane-based products and two newly synthesized acrylic ones, when they are used as water-repellent protective agents to prevent the deterioration of limestone. The macroscopic and microscopic investigations allowed to correlate the hygroscopic behavior of the treated stone with the distribution of the product on the stone surface and its penetration depth into the specimens. The results highlight that the two silane products, HY and WR, completely hindered the water absorption, spread from the treated to the untreated surface, occluding the pores of the stone. On the contrary, the two acrylic coatings, HR2 and HR3, and the silane-based NP product were

mainly distributed on the stone surface, slowing down the water-uptake but still reaching, at very long time, an equilibrium water content similar to that of the reference. Although there is not yet a standardized protocol to detect any kind of interference between protective product and stone material, in addition to contact angle, colorimetry and gravimetry, widely used for this purpose, here we used NMR relaxometry to test the hygroscopic properties and porous structure of the stone before and after the treatment. Furthermore, powerful analyses were performed, through micro-FTIR and SEM-EDS techniques, to go into details on the microscopic distribution of the coating on the surface and into the volume of the sample. It is beyond doubts that this kind of data could be useful to choose the most suitable product according to the artwork to be protected and the environment in which it is placed.

References

1 T. Warscheid and J. Braams, *Int Biodeterior Biodegradation*, 2000, **46**, 343–368.

2 Y. Nuhoglu, E. Oguz, H. Uslu, A. Ozbek, B. Ipekoglu, I. Ocak and I. Hasenekoglu, *Science of the Total Environment*, 2006, **364**, 272–283.

3 Stanaszek-Tomal,El˙zbieta, *coatings*, 2020, **10**, 1203.

4 J. Faimon, J. Štelcl, S. Kubešová and J. Zimák, *Environmental Pollution*, 2003, **122**, 417–422.

5 M. A. Kakakhel, F. Wu, J. D. Gu, H. Feng, K. Shah and W. Wang, *Int Biodeterior Biodegradation*, 2019, **143**, 104721.

6 J. S. Pozo-Antonio, T. Rivas, A. J. López, M. P. Fiorucci and A. Ramil, *Science of the Total Environment*, 2016, **571**, 1017–1028.

7 S. A. Ruffolo, F. De Leo, M. Ricca, A. Arcudi, C. Silvestri, L. Bruno, C. Urzì and M. F. La Russa, *Int Biodeterior Biodegradation*, 2017, **123**, 17–26.

8 R. Rippka, J. Deruelles and J. B. Waterbury, *J Gen Microbiol*, 1979, **111**, 1–61.

9 F. Gabriele, M. Tortora, L. Bruno, C. Casieri, M. Chiarini, R. Germani and N. Spreti, *J Cult Herit*, 2021, **49**, 106–114.

10 UNI EN 15886, *Conservation of cultural property–test methods–colour measurement of surfaces. Official Italian version of EN, 15886.*

11 G. Cappelletti, P. Fermo and M. Camiloni, *Prog Org Coat*, 2015, **78**, 511–516.

12 E. J. Vermeij, P. D. Zoon, S. B. C. G. Chang, I. Keereweer, R. Pieterman and R. R. R. Gerretsen, *Forensic Sci Int*, 2012, **214**, 96–104.

13 V. Bortolotti, M. Camaiti, C. Casieri, F. De Luca, P. Fantazzini and C. Terenzi, *Journal of Magnetic Resonance*, 2006, **181**, 287–295.

14 UNI EN 15801, *Conservation of Cultural Property - Test Methods - Determination of Water Absorption by Capillarity*.

15 W. Bilger, U. Schreiber and M. Bock, *Oecologia*, 1995, **102**, 425–432.

16 U. Schreiber, C. Neubauer and U. Schliwa, *Photosynth Res*, 1993, **36**, 65–72.

17 L. Bruno, L. Rugnini, V. Spizzichino, L. Caneve, A. Canini and N. T. W. Ellwood, *Ann Microbiol*, 2019, **69**, 1023–1032.

18 F. Gherardi, in *Conserving Stone Heritage. Cultural Heritage Science*, eds. F. Gherardi and P. Noni Maravelaki, Springer, Cham, 2022, pp. 137–176.

19 A. E. Charola, *APT Bulletin*, 1995, **26**, 10.

20 UNI EN 16581, *Conservation of Cultural Heritage - Surface Protection for Porous Inorganic Materials - Laboratory Test Methods for the Evaluation of the Performance of Water Repellent Products.*

21 M. Hosseini and I. Karapanagiotis, *Advanced materials for the conservation of stone*, Cham, Switzerland: Springer, 2018.

22 G. Wheeler, *Alkoxysilanes and the Consolidation of Stone*, Getty Publications, Los Angeles, 2005.

23 C. Casieri, C. Terenzi and F. De Luca, *Magnetic Resonance in Chemistry*, 2015, **53**, 15–21.

24 V. Di Tullio, N. Proietti, D. Capitani, I. Nicolini and A. M. Mecchi, *Anal Bioanal Chem*, 2011, **400**, 3151–3164.

25 V. Di Tullio, M. Cocca, R. Avolio, G. Gentile, N. Proietti, P. Ragni, M. E. Errico, D. Capitani and M. Avella, *Magnetic Resonance in Chemistry*, 2015, **53**, 64–77.

26 F. Rosi, L. Cartechini, D. Sali and C. Miliani, *Physical Sciences Reviews*, 2019, **4**, 1–19.

27 S. Bugani, M. Camaiti, L. Morselli, E. Van De Casteele and K. Janssens, *Anal Bioanal Chem*, 2008, **391**, 1343–1350.

28 A. Calia, M. L. Tabasso, A. M. Mecchi and G. Quarta, *Geol Soc Spec Publ*, 2014, **391**, 139–156.

29 Y. Cao, A. Salvini and M. Camaiti, *Prog Org Coat*, 2017, **111**, 164–174.

30 F. G. Adamopoulos, E. C. Vouvoudi, E. Pavlidou, D. S. Achilias and I. Karapanagiotis, *Coatings*, 2021, **11**, 1–12.

31 D. Pinna, *Int Biodeterior Biodegradation*, 2022, **172**, 105437.

32 A. Chatzigrigoriou, I. Karapanagiotis and I. Poulios, *Coatings*, 2020, **10**, 334.

33 C. Casieri, L. Senni, M. Romagnoli, U. Santamaria and F. De Luca, *Journal of Magnetic Resonance*, 2004, **171**, 364–372.

34 F. Casadio and L. Toniolo, *JAIC*, 2004, **43**, 3–21.

Curriculum Vitae

Education and training:

2024-ongoing **Research grant in CHIM/06**
University of L'Aquila
Project: "Cross-linking mass spectrometry and chemical proteomics applied to structural biology for mosquito control."
Responsible scientist: Prof. Claudio Iacobucci

2020 – ongoing **PhD in Physical and Chemical Sciences - Curriculum "Chemical Sciences", XXXVI cycle, SSD: CHIM/06**
University of L'Aquila
Thesis title: "Enzyme Catalysis: A Multifaceted Examination of Free and Immobilized Enzymes inside Alginate Beads."
Supervisor: Prof. Nicoletta Spreti

2018 – 2020 **Master's Degree in Chemical Sciences (LM-54), Curriculum "Chemistry of Organic and Bioactive Molecules"**
University of L'Aquila
Thesis title: "Heterogeneous enzymatic catalysis on a biopolymeric matrix: *Candida Rugosa* lipase in alginate hydrogel and beads."
Supervisor: Prof. Nicoletta Spreti
Graduation date: 25/07/2020; final grade: 110/110 C*um Laude*

2015 – 2018 **Bachelor's degree in Chemical and Material Sciences and Technologies (L-27), Curriculum "Chemistry"**
University of L'Aquila
Thesis title: "Idrogel di Alginato: Sviluppo ed applicazione ai beni culturali."
Supervisor: Prof. Nicoletta Spreti
Co-Supervisor: Prof. Cinzia Casieri
Graduation date: 28/07/2018; final grade: 110/110 C*um Laude*

Schools attended:

- CHESS 2022 - Conventional and High-Energy Spectroscopies for Inorganic, Organic and Biomolecular Surfaces and Interfaces. (February 21-25, 2022)

- VI National School of Chemical Teaching "Giuseppe Del Re" (November 17-30, 2021)
- XIII School of Educational Research and Chemical Teaching "Ulderico Segre" (November 17-30, 2021)

- "National Contest Catalysis at Play" (CIG 2021) Organized by the Interdivisional Catalysis Group of the Italian Chemical Society (July 27-30, 2021)

Teaching activity:

-Tutoring activity of Laboratory of Organic Chemistry II for students of the degree course in Chemistry (L-27), University of L'Aquila, a.a. 2020-2021.
-Tutoring activity of Laboratory of Organic Chemistry II for students of the degree course in Chemistry (L-27), University of L'Aquila, a.a. 2021-2022.
-supervision of a degree thesis in Chemical Sciences (LM-54) entitled: "Unconventional kinetics of Horse Liver Alcohol Dehydrogenase (HLADH): a combined experimental-computational study.", University of L'Aquila, 2023.
-supervision of a degree thesis in Chemical and Material Sciences and Technologies (L-27) entitled: "Studio dell'attività catalitica dell'alcol deidrogenasi equina incapsulata in perle di alginato", University of L'Aquila, 2022.
- supervision of a degree thesis in Chemical Sciences (LM-54) entitled: " Proprietà catalitiche della lipasi B da *Candida antarctica* (CALB): un approccio combinato teorico-sperimentale.", University of L'Aquila, 2021.

Seminars held:

-"When a metal meet Biochemistry", TMS (Thursday Morning Science), University of L'Aquila, February 6, 2020.

Publications

Unveiling Cofactor Inhibition Mechanisms in Horse Liver Alcohol Dehydrogenase: an Allosteric Driven Regulation
Alice Vetrano, Matteo Capone, Matteo Farina, Francesco Gabriele, Nicoletta Spreti, Isabella Daidone, submitted

"Prevention of Swelling Phenomenon of Alginate Beads To Improve the Stability and Recyclability of Encapsulated Horse Liver Alcohol Dehydrogenase."
Alice Vetrano, Francesco Gabriele, Nicoletta Spreti
ChemBioChem, **2023**, 24, e202300456
https://doi.org/10.1002/cbic.202300456

"A combined experimental and computational approach for the rationalization of the catalytic activity of lipase B from *Candida antarctica* in water–organic solvent mixtures."
Alice Vetrano, Isabella Daidone, Nicoletta Spreti, Matteo Capone
Journal of Chemical Technology and Biotechnology, **2023**, 98, 2429–2436
https://doi.org/10.1002/jctb.7467

"Evaluation of acrylic and silane coatings on limestone through macroscopic and microscopic analyses."
Francesco Gabriele, Cinzia Casieri, Alice Vetrano, Nicoletta Spreti
Materials Chemistry and Physics, **2023**, 307, 128194
https://doi.org/10.1016/j.matchemphys.2023.128194

"Characterization of lipase from *Candida rugosa* entrapped in alginate beads to enhance its thermal stability and recyclability."
Alice Vetrano, Francesco Gabriele, Raimondo Germani, Nicoletta Spreti
New Journal of Chemistry, **2022,** 46, 10037-10047
https://doi.org/10.1039/d2nj01160c

"New oxidative alginate-biocide hydrogels against stone biodeterioration."

Franesco Gabriele, Alice Vetrano, Laura Bruno, Cinzia Casieri, Raimondo Germani, Lorenza Rugnini, Nicoletta Spreti
International Biodeterioration & Degradation, **2021**, 163, 105281
https://doi.org/10.1016/j.ibiod.2021.105281

Conferences contributions

TMS Day of Science 2022 - September 14, 2023
-*Oral communication* entitled: "Improving Biocatalyst Stability and Recyclability: Immobilization of HLADH in Alginate Beads with Calcium Ion Reinforcement."
Alice Vetrano, Francesco Gabriele, Nicoletta Spreti

6th EuChemS Conference on Green and Sustainable Chemistry (6th EuGSC) September 3-6, 2023, Salerno
-*Poster communication* entitled: "Enhancing stability of HLADH immobilized in alginate beads: a promising approach for biocatalyst optimization."
Alice Vetrano, Francesco Gabriele, Nicoletta Spreti

XXXVIII Interregional Meeting of the Italian Chemical Society – Section Toscana, Umbria, Marche and Abruzzo (TUMA 2022), September 1-2, 2022, Perugia
-*Flash + Poster communication* entitled: "Biobased active food packaging: phytochemical compound as additives in biodegradable alginate film."
Alice Vetrano, Francesco Gabriele, Nicoletta Spreti

First Symposium for YouNg Chemists: Innovation and Sustainability (SYNC 2022) June 20-23, 2022, Rome
-*Oral communication* entitled: "Alginate beads: effect of the formulation on both internal morphology of the matrix and catalytic efficiency of entrapped enzymes."
Alice Vetrano, Francesco Gabriele, Nicoletta Spreti, Raimondo Germani

Merck Young Chemists Symposium 2021 (MYCS 2021) November 22-24, 2021, Rimini ISBN: 978-88-94952-25-4
-*Oral communication* entitled: "HLADH activity and recyclability: a kinetic approach."
Alice Vetrano, Francesco Gabriele, Nicoletta Spreti, Laura Goracci, Raimondo Germani

I giovani e la Chimica in Abruzzo, SCI Sezione Abruzzo July 5-6, 2021
ISBN 978-88-94952-22-3 (virtual)
-*Oral communication* entitled: "Immobilization of *Candida Rugosa* Lipase in alginate beads for catalytic purpose."
Alice Vetrano, Francesco Gabriele, Nicoletta Spreti
-*Oral communication* entitled: "Polysaccharide-based films as sustainable active food packaging."
Francesco Gabriele, Alice Vetrano, Nicoletta Spreti, Raimondo Germani

European Conference on Biodeterioration of Stone Monuments (ECBSM 2020) – 4th edition – November 5-6, 2020 (virtual)
-*Oral communication* entitled: "Effectiveness of oxidative alginate-biocide hydrogels for the removal of microbial contaminants from calcareous stone materials."
Francesco Gabriele, Alice Vetrano, Laura Bruno, Cinzia Casieri, Raimondo Germani, Nicoletta Spreti

Prizes

- 2nd prize at the National Contest "Catalysis at Play" (CIG 2021)
- Zentek-sponsored "BEST ORAL PRESENTATION" Award at the conference "I giovani e la Chimica in Abruzzo", SCI Sezione Abruzzo, July 5-6, 2021."